UNIVERSITÀ DEGLI STUDI
DI GENOVA

ISTITUTO
ITALIANO DI
TECNOLOGIA

DOCTORATE SCHOOL IN SCIENCES ANS TECHNOLOGIES OF CHEMISTRY AND MATERIALS

CYCLE: XXX

CURRICULUM: Nanochemistry

Investigation of Inorganic Nanocrystals as Electrode Material for Lithium and Sodium Ion Batteries

---

NAME: Lin **SURNAME:** Chen

SUPERVISORS: Liberato Manna, Simone Monaco; Bruno Scrosati;

TUTOR: Marco Panizza

Acknowledgements

The first acknowledgement goes to Prof. Liberato Manna for having welcomed me in his research group in Nanochemistry Department at Istituto Italiano di Tecnologia. Probably I wouldn't find a more organized scientific environment to manage my research work. Thanks to Prof. Marco Panizza for following my research work. To be honest, my improvement in scientific skills mostly thanks to Dr. Simone Monaco. I would claim him a friend more than my supervisor, he wisely guided me during my doctoral activities, supporting me to explore with new ideas and redirecting me to the right path when something went wrong. He is always open for any ideas and discussions and my doctoral research would not be so interesting without him. I appreciate his scientific knowledge and patience which is important to wide my knowledge and enrich my experiences.

I would like also to express my gratitude to Dr. Gianluca Longoni, for helping me to finishing my research work in the last year of my doctoral activities. His professional scientific attitude and sophisticated experiences influenced me a lot. The brilliant and professional skills that he expressed in the research activated the working process and made it productive. I appreciate his effective and professional guidance in my research and his kindness in helping me.

My appreciation also goes to my friends, Javad, Leyla, Anh, Zahid, Nickel, Taimoor, Andrea and Sergey. I still remember the time that we were spending together to prepare the courses and examinations as it happened yesterday. I couldn't remember how much stress we got from the course and how many times we were encouraging each other. A profound grateful to Anatolii, thanks for your supports, your humorous, your patients and your understanding. You are like an energy storage device, always charged with positive energy and always ready to share it with me. My life is more colorful and meaningful because of all of you.

Contents

List of Publications

This thesis is based on the following works:

I. **Lin Chen**, Enrico Dilena, Andrea Paolella, Giovanni Bertoni, Alberto Ansaldo, Massimo Colombo, Sergio Marras, Bruno Scrosati, Liberato Manna*, and Simone Monaco*, *Relevance of $LiPF_6$ as Etching Agent of $LiMnPO_4$ Colloidal Nanocrystals for High Rate Performing Li-ion Battery Cathodes*, ***ACS Appl. Mater. Interfaces***, **2016**, 8,4069-4075.

II. **Lin Chen**, Michele Fiore, Ji Eun Wang, Riccardo Ruffo, Do-Kyung Kim and Gianluca Longoni*, *Readiness level of Sodium-ion battery technology: a materials review*. ***Adv. Sustaina Adv. Sustainable Syst***. **2018**, 1700153.

III. **Lin Chen**, Sergio Marras, Giovanni Bertoni, Francisco Palazon, Mauro Gemmi Liberato Manna*, Simone Monaco*, *Colloidally Assisted Synthesis to Phase Pure $Na_{1.7}Ni_{1.0}Mn_{2.9}O_{7.6}$ with Suppressed P2/O2 Phase Transition as High Stable Cathode for Na-ion Batteries*, submitted **2018**.

Abstract

The worldwide demand for a clean, safe, high specific capacity and high energy rechargeable batteries systems keeps increasing. Li-ion batteries (LIBs) and Na-ion batteries (NIBs) have been proved to be reliable technologies, for a large variety of applications, ranging from portable high-end electronics, stationary. Recently they have been attracting a mounting interest of automotive industry, focused on hybrid (HEV) and electric vehicles (EV) design. The conductivity, working potential and specific capacity of the materials are the main issues which need to be taken into consideration for the high specific capacity and high energy batteries. Two main strategies are today pursued to improve energy of rechargeable batteries. The first solution, that combine crystal size reduction and carbon conductive coating, has been widely used to improve the ionic and electronic conductivity of the material. The second one is to increase the working voltage by choosing cathode materials with high-voltage Li^+/Na^+ intercalaction/deintercalation reactions. The PhD research activity has been devoted to the design, synthesis and electrochemical characterization of reliable phosphate and oxide materials for the LIBs and NIBs, fully exploiting the above mentioned optimization strategies. For what concern LIBs material optimization, high-voltage olivine phosphate $LiMnPO_4$ (LMP) nanoparticles have been synthesized by colloidal strategy.

To get an effective carbon coating layer on the surface of the nanoparticles, a special etching process has been applied in order to modify the nanoparticles surface. As a result, the electronic conductivity of the nano-metric particles, is sensibly improved. This work is introduced in **Chapter III**.

Chapter IV, **V** and **VI** contain the design, synthesis and investigation of binary transition metal oxide layered materials as electrode for NIBs. In particular, Ni-containing layered oxide are interesting systems because the overall electrochemical performance is based on the $Ni^{2+/3+/4+}$ Red-Ox couple which has a high operating voltage. P2-$Na_{2/3}Ni_xMn_{1-x}O_2$ and $Na_xNi_{x/2}Ti_{1-x/2}O_2$ material were designed and introduced in Chapter IV and V. The P2/O2 irreversible phase transition that happens above 4.2 V in the P2-type layered material leads to a capacity decay. A colloidal-assisted two-step synthetic route and the Na:Ni:Mn=1.7:1:3 ratio selection revealed to be of foremost importance in stabilizing P2-$Na_{2/3}Ni_xMn_{1-x}O_2$, bearing long charge/discharge cycles at working voltages of 4.4 V vs. Na^+/Na. Another Ni-containing binary metal oxide layered material $Na_xNi_{x/2}Ti_{1-x/2}O_2$ ($0.60 \leq x \leq 1.0$), has been studied as a bi-functional electrode material for NIBs by

selectively activating the redox couple of Ni^{4+}/Ni^{3+} and Ti^{4+}/Ti^{3+}. A series of $Na_xNi_{x/2}Ti_{1-x/2}O_2$ samples were designed and studied by modulating synthetic methods. Bi-polar P2-$Na_x(Ni^{2+})_{1/3(}Ti^{4+})_{2/3}O_2$ layered material was considered to be the most promising candidate for the symmetric Na-ion full cell in terms of phase purity and electrochemical characteristics. 1M $NaClO_4$ in PC/EC (1:1 V/V) as electrolyte was chosen by selecting and comparing the different electrolyte solutions for the $Na_x(Ni^{2+})_{1/3(}Ti^{4+})_{2/3}O_2$ as both cathode and anode. The optimized parameters are the foundation for the symmetric Na-ion full cell study. Symmetric Na-ion full battery with the same material as both cathode and anode became very attractive as a promising alternative to standard non-symmetric architectures from a commercial standpoint recently. Different types of symmetric Na-ion full batteries in the literatures have been reviewed in order to develop an in-depth knowledge of the state-of-the-art in the field. Na-ion battery based on P2- $Na_x(Ni^{2+})_{1/3(}Ti^{4+})_{2/3}O_2$ have been eventually introduced and investigated.

List of Figures

List of Tables

CHAPTER I

Introduction

The term “battery” was adopted by the scientists in 1700s to represent multiple electrochemical cells connected together. A typical battery consists of two electrodes that are electrically isolated by a separator soaked in an electrolyte to promote the movement of ions and allow the charge balance of the system.

There are two main challenges in the field of energy storage that our world faces: the first is to shift electricity production from burning fuel to sustainable energy sources and second one is to move on-ground transportation towards electrical propulsion by using electric vehicles (EVs) instead of cars driven by internal combustion engines (ICEs)[1]. One of the positive achievements for last few centuries since first batteries were developed is so called “rechargeable battery” which is a type of battery that can be charged/discharged more than once.

Successful implementation of theoretical advantages from using electric cars instead of ones based on organic fuels combustion is the scenario of upgraded and better future life . The combination of portable rechargeable battery and the electrochemical capacitor can clearly displace the internal combustion engine as the way to powering electric vehicles and other devices.

For many years, nickel-cadmium (Ni-Cd) battery had been the only suitable battery for portable equipment from wireless communications to mobile computing. Nickel-metal-hydride (Ni-MH) and lithium-ion batteries emerged in the early 1990s, lithium ion batteries have been considered able to satisfy the increasing energy demand because its high energy density.

1.1 Li-ion batteries

Lithium-ion battery (LIB), conceived and developed in Japan by Asahi Kaser Co and first commercialized by Sony Co in 1991, became the better candidate in order to fit the fast technological develop requirements. For a given cell, larger values of Wh/L and Wh/kg translate into smaller and lighter battery. The low atomic number of Li-based materials and their wide redox range, results in significantly high-energy density of the LIBs compared to the conventional lead

acid and Ni-MH batteries[2], as reported in **Table 1.1**[3]. Additionally, LIBs has other attractive features such as high efficiency, low self-discharge and long practical use. These characteristics make LIBs the enabling technology for the proliferation of portable battery-powered electronic devices, especially notebook computers and mobile phones. Li-ion batteries have an unmatchable combination of high energy and power density, making them as the technology of the choice for portable electronics[4].

Table 1.1. Performance comparison among various energy storage devices

	Working temperature (°C)	Energy		Power (W kg^{-1})	Voltage (V)	Self-discharge (%/Month)	Cycle life @80% DOD	Cost estimation	
		Wh L^{-1}	Wh kg^{-1}					$/kWh	$/kW
Lead Acid	~30-60	50-70	20-40	300	2.1	4-8	200	150	10
NiMH	~20-50	200	40-60	1300-500	1.2	20	>2500	500	20
Li-ion	~20-55	150-200	100-200	3000-800	~3.6	1-5	<2500	200	20-75
Double Layer Capactor	~30-65	5	5-20	1500	~2.5	30	-	2000	50

The schematic illustration of a lithium ion battery, $LixC_6$ as the anode and lithium cobalt oxide ($LiCoO_2$) as a cathode, as an example is shown in **Figure 1.1**. Lithium hexafluorophate ($LiPF_6$) in a mixture of Ethylene Carbonate (EC) and Dimethyl Carbonate (DMC) as electrolyte. The cathode and anode are separated by a separator as shown in Figure 1.1. When the Li-ion battery discharges, the Li^+ moves from anode to the cathode, facilitated by a Li^+-containing salt in the electrolyte, meanwhile, the electrons are passing from external circuit to power the devices and reverse occurs during the charging process. The electrochemical reaction takes place in the battery can be presented by the reaction:

$$XLi \leftrightarrow X + Li^+ + e^-$$

Where X is the electrode material host, e.g. iron phosphate, carbon, oxide.

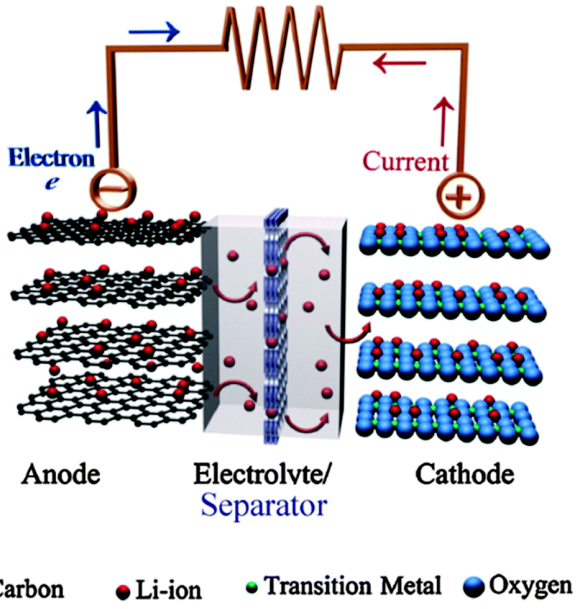

Figure 1.1 Schematic illustration of a typical lithium-ion battery where graphite and $LiCoO_2$ are used as anode and cathode, respectively[5]

The electrode materials must be a good ionic and electronic conductor because it must allow the flow of both lithium ions and electrons that generated during the reaction[6]. Therefore, the performances of the batteries are strongly depended on the structure and properties (electronic and ionic conductivity) of the active electrode materials.

Moreover, the power and energy density of a battery are largely depended on the electrode materials as well[7]. The electrical energy can be expressed either by per unit weight (Wh kg^{-1}) or per unit of volume (Wh L^{-1}) as listed in **Table 1.1**. The energy that a battery is able to deliver can be presented as a function of cell potential (V) and capacity (Ah kg^{-1}) according to the equation:

$$E = Q \cdot V$$

where E is the energy, Q is the capacity and V is the open circuit voltage of the battery. Therefore, to develop a high specific energy battery, it is essential to have high reduction potential cathode material, low reduction potential anode materials and high specific capacities[8-10,11].

The current choice for anode materials for Li-ion batteries is graphite due to its long life, abundant material supply and relatively low cost. Compared to lithium metal, it reduces the lithium activity and the reactivity with electrolyte and improves safety, but also leads to a lower cell voltage. There

are efforts in the development of improved anode materials. However, more effort might have been made to develop the cathode material, which gives more possibilities of a practical research[12].

The pioneering work of Goodenough and co-workers[13-15] represented the possibility of using layered $LiCoO_2$ as cathode materials for lithium rechargeable battery in the 1980's with an extended cell voltage of above 4.0 V *vs*. Li^+/Li. Thereafter, many materials such as $LiNiO_2$, $LiMnO_2$, V_2O_5 etc. were proposed as possible alternatives to the existing layered $LiCoO_2$ as cathodes due to its own drawbacks[6, 16, 17]. As successful result of another important work of Goodenough *et al.*[18], the phosphor-olivine $LiMPO_4$ compound (M = Mn, Fe, Ni) have been explored as a potential positive electrode material for lithium rechargeable batteries.

In order to have a battery with high energy, the conductivity (electronic and ionic conductivity), potential and specific capacity of the materials are the main issues need to be taken into consideration. Carbon coating have been proved to be effective to improve the electronic conductivity. Moreover, drop down of crystal size of active material from macro to nanoscale helps to reduce the Li^+ diffusion length and consequently improves the ionic conductivity. The strategy that combine carbon coating and crystal size reduction have been wildly used to improve the conductivity of the electrode. Another solution is to increase the working voltage by choosing cathode materials with high-voltage Li^+ intercalation/deintercalation reactions.

1.1.1 Scaling down the crystal size of electrode material to nano

Common LIBs are based on intercalation electrodes with an electrochemical process involving the intercalation/deintercalation of Li-ions between anode and cathode. It is expected that adopting nano-structurization of active electrode materials may result in the reduction of the diffusion length of the lithium ions in and out of the electrode since the characteristic time constant for diffusion is given by

$$t= L^2/D$$

where L is the diffusion length and *D* is the diffusion constant. The time *t* for intercalation decreases with the square of the particle size on replacing micrometer with nanometer particles. Therefore, to improve kinetics, nanostructured electrode morphologies, such as nanoparticles, nanofibers and others having at least one nano-metric dimension, have been considered[19-21].

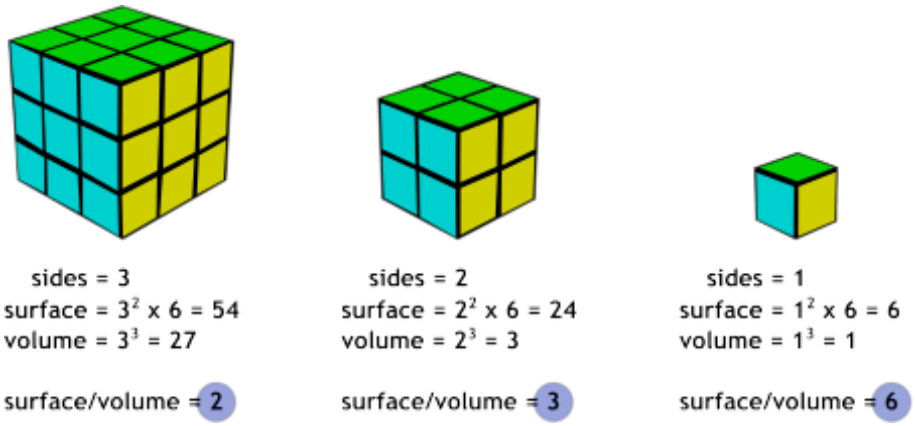

Figure 1.2. The surface area to volume area for particles with different sizes.

On the other hand, because of the large surface-to-volume ratio (as shown in **Figure 1.2**), which gives more surface for the material to contact with the electrolyte, the use of nanostructures is expected to result in an increase of the electrochemical activity by many orders of magnitude. In addition, the low tap density of these large surface area structures depresses the volumetric energy density and increases the reactivity of the battery[19].

A number of advances have been made in the LIBs field by controlling particles size in addition to composition, structure, and morphology in order to design better electrodes and electrolyte components[22-25]. Decreasing the electrochemically active materials to sub-micrometer and even smaller sizes combined with carbon-coating has led to new directions in designing electrode materials[4, 21].

Nanoscale design of the structure and chemistry of electrode materials may enable the development of a new generation of devices that approach the material theoretical capacity limit for electrochemical storage and deliver electrical energy rapidly and efficiently[26, 27].

1.1.2 High-voltage cathode materials for LIBs

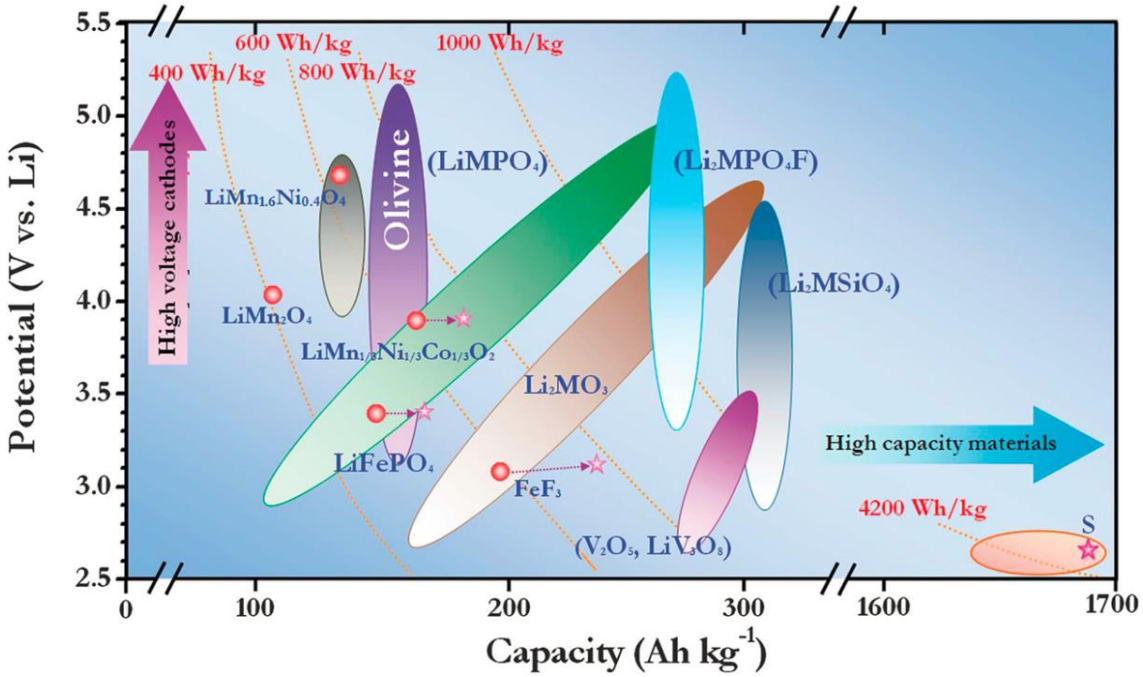

Figure 1.3. Schematic representation of the plot of LIB cathode material: potential vs. capacity. $LiMPO_4$, $LiMSiO_4$ and Li_2MPO_4F, where M=Fe, Mn, Co, Ni, ect; Li_2MO_2, where M= Mn, Mo, Ru, etc.[28]

The high-voltage cathode[8] materials that have been reported are mostly previously based on three types of materials: poly-anion compounds, spinel-type oxides and α-$NaFeO_2$-type layered oxides. As the example are $LiFePO_4$, $LiMn_2O_4$ and $LiNi_xCo_yMn_{1-x-y}O_2$, respectively. **Figure 1.3** presents the plots of potential vs. capacity these cathode materials. Polyanionic cathode materials have been extensively investigated since Goodenough's group, which includes phosphate (such as olivine $LiMPO_4$, and monoclinic $Li_3M_2(PO_4)_3$), silicates, fluorophosphates and fluorosilicates. Large $(XO_4)^{3-}$ (X = S, P, Si, As, Mo, W) polyanions occupy lattice positions and increase cathode redox potential while also stabilizing its structure[23].

The olivine phosphate ($LiMPO_4$) exhibit moderate theoretical discharge capacity, high thermodynamic stability, and stable discharge platform. The redox potentials are 3.5, 4.1, 4.8 and 5.1 V (vs. Li^+/Li) when M = Fe[29], Mn[28], Co[30] and Ni[31], respectively. However, the electrolyte oxidation process[9] that happens at potential higher than 4.5 V in conventional electrolytes limits the use of $LiCoPO_4$ and $LiNiPO_4$. $LiFePO_4$, with a theoretical capacity of 170 mAh g^{-1}, is the first phosphate proposed to work as cathode material in LIBs. It is particularly remarkable due to its good cyclic performance, abundant raw materials, non-toxicity, etc. $LiMnPO_4$[32, 33, 34, 35] has a more

positive Li^+ intercalation/deintercalation potential which is at 4.1 V vs. Li^+/Li compared to $LiFePO_4$ and it is another proper candidate that is comparable with the common used electrolytes.

1.2 The challenges of Li-ion batteries

"Safety of the system" is the motto for Li-ion batteries. Manufacturers are careful to claim and ensure that the cells are safe in normal operation conditions. In addition, cell design includes electrical preventers that shut off current flow when an abuse condition arises (Battery Management System or BMS). The name "lithium-ion" now is accepted by the battery community worldwide, although there is no lithium metal in the cell. However, very often lithium-metal deposition dendritically occurs during charging with the graphite anode and it may cause safety issues because it may cause an internal short circuit of the cell.

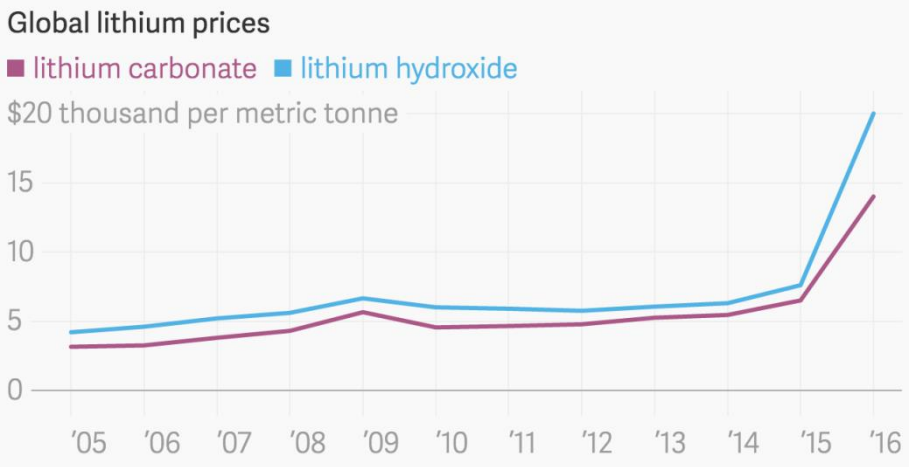

Figure 1.4 The price of lithium carbonate and lithium hydroxide within 10 years.

Another concern is about the amount of the Li resources that are still available for gaining and processing from the earth, they would not be sufficient to satisfy the increased demands on LIBs. In a conservative report published in 2012 (Japan), 7.9 million tons of metallic Li were esteemed to be required in order to replace half of the ICE cars world population, with hybrid electric vehicles and fully electric verficles[36]. It indicates that in the long term the cost of Li increase as demand increases. It has been proven by the global lithium price data collection figure offered by Benchmark company, as shown in **Figure 1.4**. The data is based on lithium carbonate and lithium

hydroxide, which are the two most commonly mined and sold raw materials for LIBs. Therefore, making provision beyond the LIB is important and alternatives with different chemistries have to be suggested[36].

1.3 Na-ion batteries

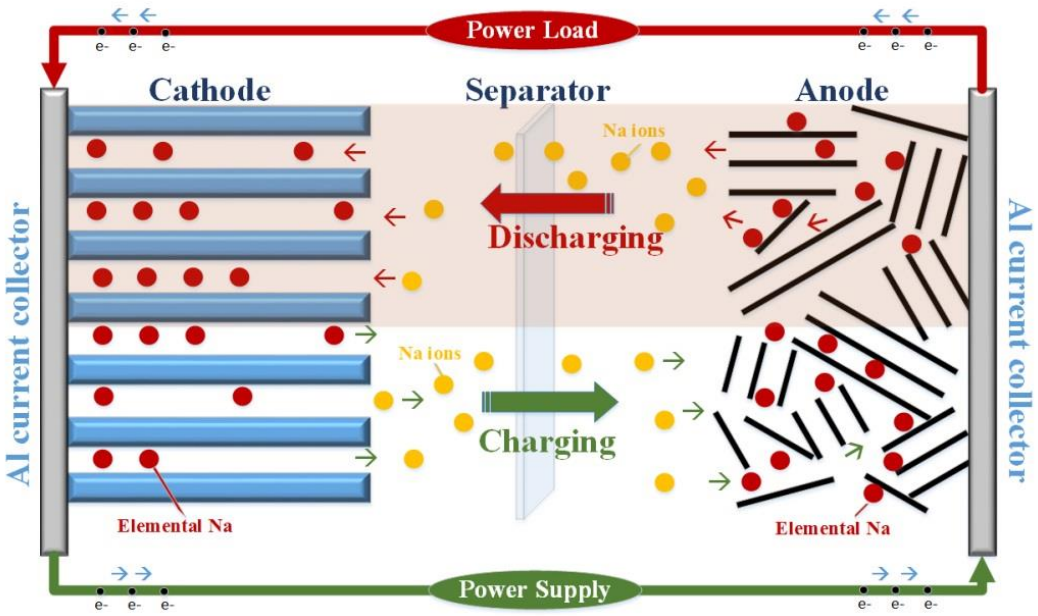

Figure 1.5. Working scheme of Na-ion batteries (NIBs)[37]

Sodium (Na) is located below Li in the periodic table and they share similar chemical properties in many aspects, both of them have one electron in their outer shell and both of them are easy to lose the electron. Sodium ion batteries (NIBs) were under investigation at the same time as LIBs in the 70s and 80s. Similar to Li-ion batteries, room-temperature rechargeable Na-ion batteries follow a working principle of the "rocking chair" storage mechanism[38], as shown in **Figure 1.5**. Sodium ions are shuttled between cathode and anode through a non-aqueous (or aqueous) Na-ion electrolyte.

Theoretically speaking, the Na-ion battery may not reach the energy density of the Li-ion battery because Na is more than 3 times heavier and larger than Li and the standard electrochemical potential of Na (2.71V) is lower than Li (3.04 V) with respect to SHE (Standard Hydrogen Electrode)[24]. As battery applications extend to large-scale storage such as electric heavy

transportation or stationary storage connected to renewable energy production, high energy density becomes less critical. With respect to the components of the battery, an estimation of the relative costs of LIBs and NIBs have been given[39] in the literatures, as compared in Figure 1.6. As the consequences, NIBs has the potential to be 10% less expensive the commercial LIBs consider the total cost.

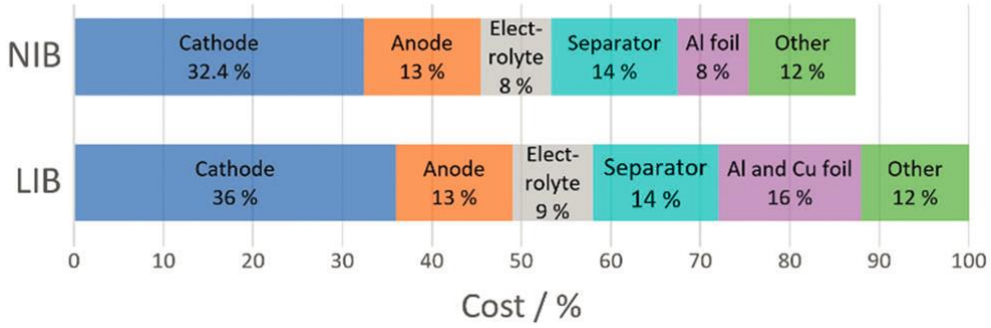

Figure 1.6 Comparison[40] of the manufacturing costs for Li-ion batteries (LIB) and Na-ion batteries (NIB).

Moreover, the abundance and low cost of Na in the earth crust makes the NIBs more preferable than LIBs for the large-scale applications, which involves a large amount of raw materials. For these reasons, the sodium alternative has been reintroduced into the battery research community. Several chemical structures that do not work for Li intercalation may do so far for NIBs which offers research of novel electrode materials[36, 41]. Therefore, there are more opportunities to explore novel electrode materials for NIBs.

1.3.1 Electrode materials

Similar to the LIBs, the most widely studied anode for the NIBs[41] are carbonaceous materials, which are attributed to their abundance, low cost and environmental friendly. Transition metal[42, 43] have also been explored to deliver high capacity during sodium storage through the conversion reaction: $M_xO_y + 2yNa^+ + 2ye^- \leftrightarrow xM + yNa_2O$, (M = transition metal). Among the oxides, Ti-based oxides[44-46] have also been widely recognized as potential anode apart from the carbonaceous materials. Apart from that, the increasing activities of alloy-based[47, 48] anode materials has flourished following the theoretical investigation of sodium ion alloys with group 14 elements by Ceder in 2011[49].

As the important component in NIBs, the cathode materials should be given for more attention because their significant effect on the electrochemical performances. The cathodes for NIBs includes the layered transition metal oxide, phosphate and fluorides etc. They share the similar rules as that of LIBs in terms of the working principles. **Figure 1.7** shows the distributions of different materials that have been studied and their publication numbers focusing on the cathode of NIBs with time. Among these cathode candidates, oxides and phosphate hold the bigger shares and the number of literature studies based on this two kind of materials dramatically increases in recent years.

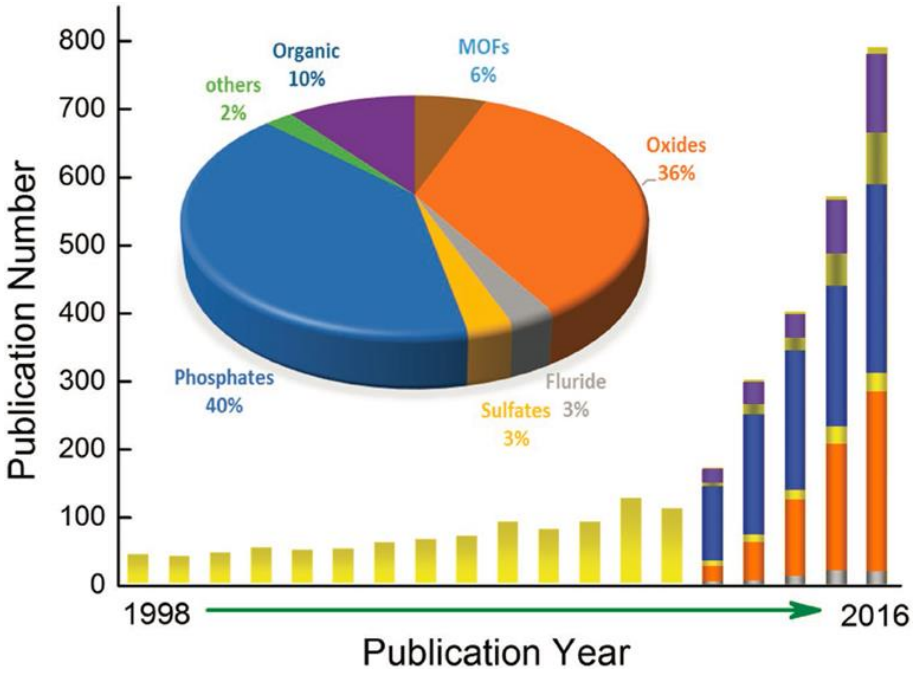

Figure 1.7 Histogram and bar chart showing the number of publications regarding cathodes for NIBs annually and in different materials system. The different color are (from bottom to top: fluride, oxide, sulfates, phosphates, MOFs, organic, others) on the vertical bars illustrating the research population of each type in the recent years[50].

Phosphates: Phosphates includes NASICON (Na Super Ionic Conductor) structure, fluorophosphates, carbonphosphates and pyrophosphates. The NASICON structure ($Na_2M_2(XO_4)_3$ where X= Si^{4+}, P^{5+}, S^{6+}, Mo^{6+}, As^{5+}), especially $Na_3V_2(PO_4)_3$ is well known for its facile sodium ion conductivity has been studied extensively. Similar to LIBs, in the NASICON structure, corner

shared MoO_6 and XO_4 polyhedra form a framework with large diffusion channels for Na^+. A new structural host, fluorophosphates[51-54] (Na_2FePO_4F, Na_2VPO_4F, $Na_{1.5}VPO_{4.8}F_{0.7}$ and $Na_3(VO)_2(PO_4)_2F$ etc.), has also been performed as cathode for NIBs. Carbonophosphates[55-57], which have been identified with sidorenkite structure, in the formula of $A_3M(CO_3)(PO_4)$ (A =Li or Na, M = Co, Mn, Fe, Ni), is a new class of potential cathode material for NIBs. The complicated structure with corner sharing of tetrahedral PO_4 groups and MO_6 octahedra forming double layers which accommodate Na atoms at two different interstitial sites. Na(1) sites coordinate with 7 oxygen atoms and Na(2) sites coordinate with 6 oxygen atoms. Pyrophosphate[57,58], which has four different Na^+ sites located in a 3D ion channel, is another unique structure cathode for NIBs. Na_4Co_3-$(PO_4)_2P_2O_7$[58] and $Na_7V_4(P_2O_7)_4PO_4$[59] were used in NIBs and offered good cyclic stability and capacity retention.

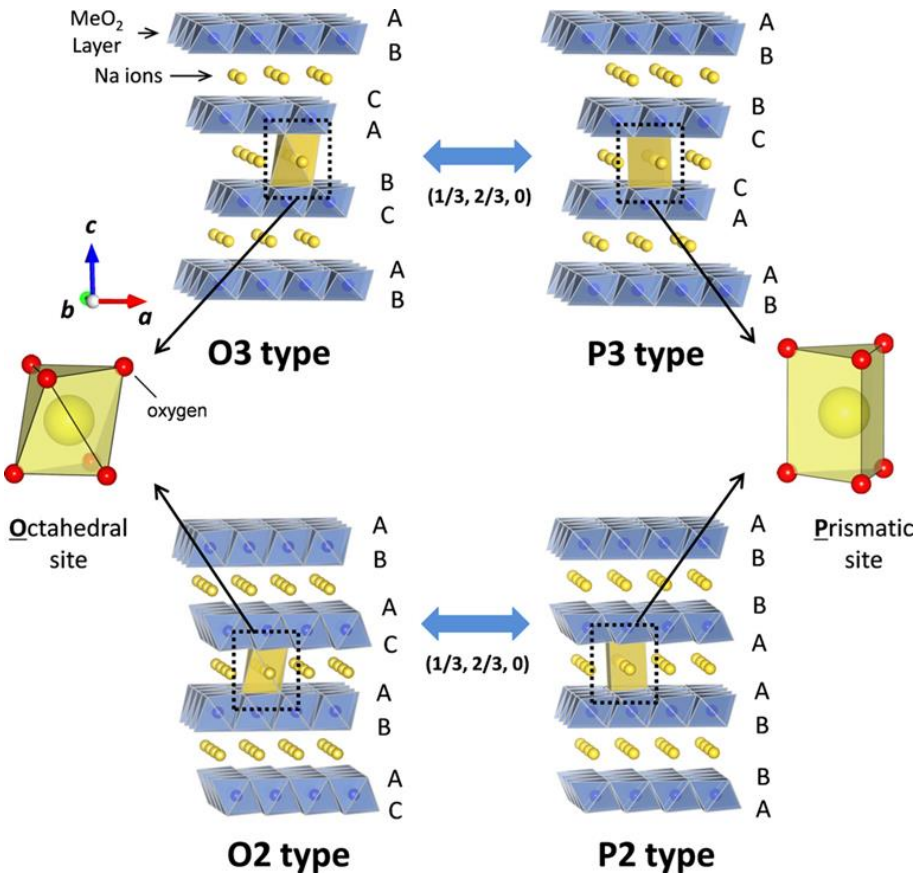

Figure 1.8. The classification of Na-M-O layered material with the sheets of edge-sharing MO_6 and phase transition process induces by sodium extraction[62].

Layered metal oxide: Among the cathode materials, layered oxide Na_xMO2[24] (M= Ti, V, Cr, Fe, Co, Mn, Ni and their combinations) are most popular cathode materials for NIBs because of their simple structure, high intercalation potentials and energy densities. Na^+ is reversibly de/intercalated between the two-dimensional layers of transition metal MO_6 octahedra during the electrochemical cycling. The electrochemical intercalation of sodium in Na_xCoO_2[60] has been first studied by Delmas during 1980s'. Typical Na layered oxides can be categorized into two main groups, O3- and P2-type, depending on the surrounding of Na environment (Octahedral and Prismatic sites) and the number of unique oxide layer packings[24, 61, 62] as shown in **Figure 1.8**. O3-type Na_xMO_2 (mainly known to occur when $0.7< x < 1$,) consists of a cubic close-packed (ccp) oxygen array, in which sodium and 3d-transition metal ions are accommodated at distinct octahedral sites because the ionic radius of Na^+ (1.02Å) is much larger than those of 3d-trasnsiton-metal ions in the trivlent state (< 0.7Å)[63]. The oxide layer stacking follows the ABCABC pattern and all Na share one edge and one face. P2-type phase is known to be structurally stabilized when the Na content in Na_xMO_2 is $0.67 < x < 0.7$, the oxide layer stacking follows the ABBA pattern and all the Na share either entirely edge or entirely face (Figure 1.8). When the Na^+ extracted from the O3- and P2-type phases, an energetically stable phase P3- and O2-type phase are achieved by gliding of MO_2 slabs without breaking M-O bonds, respectively, as shown in Figure 1.8. Suppressing or reducing the irreversible phase transitions is essential to improve the electrochemical performance of layered oxides in NIBs.

1.3.2 Symmetric full sodium-ion battery

As we discussed above for the LIBs, the energy, cycle life and the cost of NIBs are basically depend on the developments of the electrode materials as well. Different cathode and anode material (**Figure 1.9**) have been studied in sodium half-cell, in which the metallic sodium acts as the anode. To build a sodium-ion full cell, the anodes need to be paired with suitable cathode materials. The corresponding specific capacity, working potential range, states of charge or discharge and so on are all need to be taken into consideration when assembling a full cell[65-68]. At present, the report of the sodium ion full batteries haven't match the results achieved in lithium ion full batteries.

Compared to the half-cell testing, the limited supply of sodium ions provided by the cathode material in a full cell, results in a greater sensitivity of the cell performance to i) the coulombic

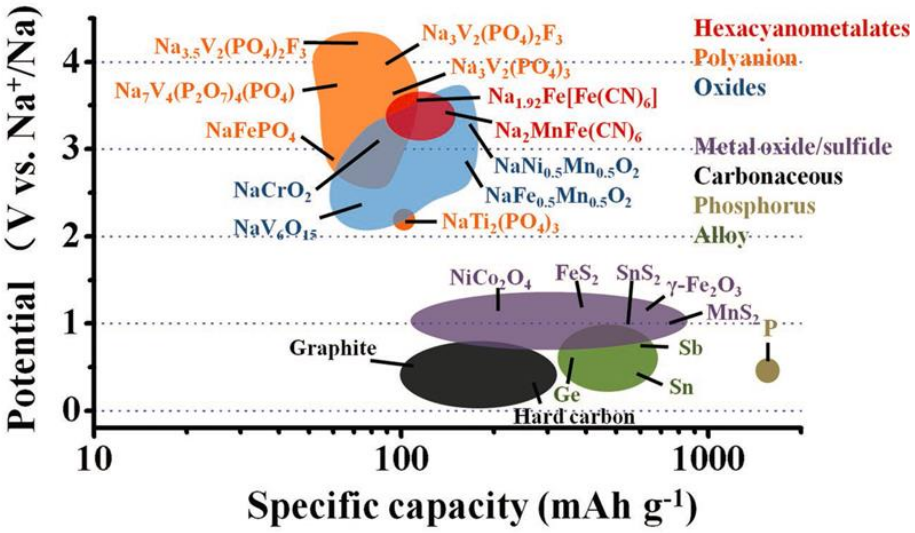

Figure 1.9. Capacity-voltage diagrams of representative cathode and anode materials for NIBs[64].

efficiencies of the electrodes; ii) the quantity of the sodium ions lost in the SEI (Solid Electrolyte Interphase, a protect layer on the surface of anode material) layer formation (both initially and ongoing during cycling); iii) any side reactions occurring within the cell [69]. The reported full cells can be divided into two main families: non-symmetric and symmetric full cell according to the electrode materials. For the non-symmetric full cell, the adopted cathode and anodes belong to two distinct families. For the symmetric full cell, the same material will be addressed both as cathode and anode by exploiting different Red-Ox sites.

In the Non-symmetric sodium ion full batteries, potential safety concerns on carbon materials (especially hard carbon) with possible thermal runaway are noticed because their plateau related with most capacities is too close to the sodium plating voltage. This kind of NIBs system cannot support the requirement of long life and safety of large-scale energy storage devices, therefore the symmetric sodium ion full cell became very attractive and promising alternative from a commercial standpoint recently. The same active materials, exploiting different redox sites and acting as both cathode and anode, can enable cells overcharging to some extent, buffer the large volume expansion (cathode expanding accompanied by anode shrinking, and vice versa) and greatly reduce the manufacturing costs and simplify the fabrication process[70-72].

1.4 Thesis structure

The main goals of current thesis are concerned around design, synthesis and characterization of phosphate and oxides electrode materials in order to improve the energy of the rechargeable batteries by i). decreasing the particle size of electrode materials; ii). choosing high-voltage cathode material. To pursue a thorough description of the work of research, four aspects are investigated and presented in this thesis:

In Chapter II, the chemicals and techniques used for the subsequent chapters will be listed.

In Chapter III, the colloidal (nano-technological) strategy is applied to synthesize the olivine phosphate $LiMnPO_4$ cathode material for Li-ion battery: For the first work, $LiMnPO_4$ nanoparticles were prepared through colloidal synthesis, then the surface of $LiMnPO_4$ nanocrystals (NCs) was etched by using $LiPF_6$. This makes the NCs dispersible in the aqueous glucose solution used as carbon source for the carbon coating step, to improve the electronic conductivity of the $LiMnPO_4$ NCs.

Chapter IV, **V**, and **VI**, contain the design and synthesis of layered oxides as electrodes for NIBs. In Chapter IV, P2-$Na_{2/3}[Ni_xMn_y]O_2$-based cathode materials for Na-ion batteries will be taken into account. P2-$Na_{2/3}[Ni_xMn_y]O_2$-based cathode materials were usually reported to drop at working voltages over 4.2 V vs. Na^+/Na, due to the P2/O2 irreversible phase transition. A colloidally-assisted two-step synthesis will be introduced to get phase pure P2-$Na_{1.7}Ni_{1.0}Mn_{2.9}O_{7.6}$. The adopted synthetic route and the chosen Na:Ni:Mn ratio (1.7:1:3) leads to a cathode material that can withstand long charge/discharge cycles at working voltages up to 4.4 V vs. Na^+/Na. Another Ni-containing binary metal oxide layered material $Na_xNi_{x/2}Ti_{1-x/2}O_2$ ($0.60 \leq x \leq 1.0$), has been studied as a bi-functional electrode material for NIBs by selectively activating the redox couple of Ni^{4+}/Ni^{3+} and Ti^{4+}/Ti^{3+}. A series of $Na_xNi_{x/2}Ti_{1-x/2}O_2$ samples are designed and studied by modulating synthetic methods in Chapter V. The optimized parameters, synthetic techniques and electrolytes, are the foundation for the symmetric Na-ion full cell study. Different types of symmetric Na-ion full batteries in the literatures is reviewed in Chapter VI in order to develop an in-depth knowledge of the state-of-the-art in the field. Symmetric Na-ion battery based on P2-$Na_x(Ni^{2+})_{1/3}(Ti^{4+})_{2/3}O_2$ is eventually introduced and investigated in the same chapter.

Chapter VII eventually summarizes the doctoral work and provides the outlook for the future research work.

1.5 References:

1. Goodenough, J. B.; Park, K.-S., The Li-ion rechargeable battery: a perspective. *Journal of the American Chemical Society* **2013,** 135, (4), 1167-1176.

2. Hannan, M.; Lipu, M.; Hussain, A.; Mohamed, A., A review of lithium-ion battery state of charge estimation and management system in electric vehicle applications: Challenges and recommendations. *Renewable and Sustainable Energy Reviews* **2017,** 78, 834-854.

3. Conte, F., Battery and battery management for hybrid electric vehicles: a review. *e & i Elektrotechnik und Informationstechnik* **2006,** 123, (10), 424-431.

4. Dunn, B.; Kamath, H.; Tarascon, J.-M., Electrical energy storage for the grid: a battery of choices. *Science* **2011,** 334, (6058), 928-935.

5. Song, M.-K.; Park, S.; Alamgir, F. M.; Cho, J.; Liu, M., Nanostructured electrodes for lithium-ion and lithium-air batteries: the latest developments, challenges, and perspectives. *Materials Science and Engineering: R: Reports* **2011,** 72, (11), 203-252.

6. Whittingham, M. S., Lithium batteries and cathode materials. *Chemical reviews* **2004,** 104, (10), 4271-4302.

7. Yoshio, M.; Brodd, R. J.; Kozawa, A., *Lithium-ion batteries*. Springer: 2009; Vol. 1.

8. Hu, M.; Pang, X.; Zhou, Z., Recent progress in high-voltage lithium ion batteries. *Journal of Power Sources* **2013,** 237, 229-242.

9. Tarascon, J.-M.; Armand, M., Issues and challenges facing rechargeable lithium batteries. *Nature* **2001,** 414, (6861), 359-367.

10. Bhatt, M. D.; O'Dwyer, C., Recent progress in theoretical and computational investigations of Li-ion battery materials and electrolytes. *Physical Chemistry Chemical Physics* **2015,** 17, (7), 4799-4844.

11. Yoshio, M.; Brodd, R.; Kozawa, A., Lithium-ion batteries: science and technologies. 2009. In Springer.

12. Etacheri, V.; Marom, R.; Elazari, R.; Salitra, G.; Aurbach, D., Challenges in the development of advanced Li-ion batteries: a review. *Energy & Environmental Science* **2011,** 4, (9), 3243-3262.

13. Mizushima, K.; Jones, P.; Wiseman, P.; Goodenough, J. B., $LixCoO_2$ (0< x<-1): A new cathode material for batteries of high energy density. *Materials Research Bulletin* **1980,** 15, (6), 783-789.

14. Thackeray, M.; David, W.; Bruce, P.; Goodenough, J., Lithium insertion into manganese spinels. *Materials Research Bulletin* **1983,** 18, (4), 461-472.

15. Goodenough, J. B., Rechargeable batteries: challenges old and new. *Journal of Solid State Electrochemistry* **2012,** 16, (6), 2019-2029.

16. Kalyani, P.; Kalaiselvi, N., Various aspects of $LiNiO_2$ chemistry: a review. *Science and Technology of Advanced Materials* **2005,** 6, (6), 689-703.

17. Thackeray, M. M.; Kang, S.-H.; Johnson, C. S.; Vaughey, J. T.; Benedek, R.; Hackney, S., Li_2MnO_3-stabilized LiMO 2 (M= Mn, Ni, Co) electrodes for lithium-ion batteries. *Journal of Materials chemistry* **2007,** 17, (30), 3112-3125.

18. Padhi, A. K.; Nanjundaswamy, K.; Goodenough, J. B., Phospho-olivines as positive-electrode materials for rechargeable lithium batteries. *Journal of the electrochemical society* **1997,** 144, (4), 1188-1194.

19. Scrosati, B.; Garche, J., Lithium batteries: Status, prospects and future. *Journal of Power Sources* **2010,** 195, (9), 2419-2430.

20. Aricò, A. S.; Bruce, P.; Scrosati, B.; Tarascon, J.-M.; Van Schalkwijk, W., Nanostructured materials for advanced energy conversion and storage devices. *Nature materials* **2005,** 4, (5), 366-377.

21. Bruce, P. G.; Scrosati, B.; Tarascon, J. M., Nanomaterials for rechargeable lithium batteries. *Angewandte Chemie International Edition* **2008,** 47, (16), 2930-2946.

22. Kucinskis, G.; Bajars, G.; Kleperis, J., Graphene in lithium ion battery cathode materials: A review. *Journal of Power Sources* **2013,** 240, 66-79.

23. Nitta, N.; Wu, F.; Lee, J. T.; Yushin, G., Li-ion battery materials: present and future. *Materials today* **2015,** 18, (5), 252-264.

24. Han, M. H.; Gonzalo, E.; Singh, G.; Rojo, T., A comprehensive review of sodium layered oxides: powerful cathodes for Na-ion batteries. *Energy & Environmental Science* **2015,** 8, (1), 81-102.

25. Slater, M. D.; Kim, D.; Lee, E.; Johnson, C. S., Sodium-ion batteries. *Advanced Functional Materials* **2013,** 23, (8), 947-958.

26. Wang, L. Y.; Zhang, H.; Cao, G. P.; Zhang, W. F.; Zhao, H. L.; Yang, Y. S., Effect of activated carbon surface functional groups on nano-lead electrodeposition and hydrogen evolution and its applications in lead-carbon batteries. *Electrochimica Acta* **2015,** 186, 654-663.

27. Gogotsi, Y., What Nano Can Do for Energy Storage.pdf>. *ACS nano* **2014,** 8, 5369-5371.

28. Aravindan, V.; Gnanaraj, J.; Lee, Y.-S.; Madhavi, S., $LiMnPO_4$–A next generation cathode material for lithium-ion batteries. *Journal of Materials Chemistry A* **2013,** 1, (11), 3518-3539.

29. Yamada, A.; Chung, S.-C.; Hinokuma, K., Optimized $LiFePO_4$ for lithium battery cathodes. *Journal of the electrochemical society* **2001,** 148, (3), A224-A229.

30. Amine, K.; Yasuda, H.; Yamachi, M., Olivine $LiCoPO_4$ as 4.8 V electrode material for lithium batteries. *Electrochemical and Solid-State Letters* **2000,** 3, (4), 178-179.

31. Xu, Y.-N.; Ching, W.; Chiang, Y.-M., Comparative studies of the electronic structure of $LiFePO_4$, $FePO_4$, Li_3PO_4, $LiMnPO_4$, $LiCoPO_4$, and $LiNiPO_4$. *Journal of applied physics* **2004,** 95, (11), 6583-6585.

32. Rudisch, C.; Grafe, H.-J.; Geck, J.; Partzsch, S.; Zimmermann, M. v.; Wizent, N.; Klingeler, R.; Büchner, B., Coupling of Li motion and structural distortions in olivine $LiMnPO_4$ from 7 Li and 31 P NMR. *Physical Review B* **2013,** 88, (5), 054303.

33. Delacourt, C.; Laffont, L.; Bouchet, R.; Wurm, C.; Leriche, J.-B.; Morcrette, M.; Tarascon, J.-M.; Masquelier, C., Toward understanding of electrical limitations (electronic, ionic) in $LiMPO_4$ (M= Fe, Mn) electrode materials. *Journal of the Electrochemical Society* **2005,** 152, (5), A913-A921.

34. Yonemura, M.; Yamada, A.; Takei, Y.; Sonoyama, N.; Kanno, R., Comparative kinetic study of olivine Li_xMPO_4 (M= Fe, Mn). *Journal of the Electrochemical Society* **2004,** 151, (9), A1352-A1356.

35. Yamada, A.; Kudo, Y.; Liu, K.-Y., Reaction Mechanism of the Olivine-Type $Lix(Mn_{0.6}Fe_{0.4})PO_4$ ($0 \leqslant x \leqslant 1$). *Journal of the Electrochemical Society* **2001,** 148, (7), A747-A754.

36. Kim, S. W.; Seo, D. H.; Ma, X.; Ceder, G.; Kang, K., Electrode materials for rechargeable sodium-ion batteries: potential alternatives to current lithium-ion batteries. *Advanced Energy Materials* **2012,** 2, (7), 710-721.

37. Tang, J.; Dysart, A. D.; Pol, V. G., Advancement in sodium-ion rechargeable batteries. *Current Opinion in Chemical Engineering* **2015,** 9, 34-41.

38. You, Y.; Yu, X.; Yin, Y.; Nam, K.-W.; Guo, Y.-G., Sodium iron hexacyanoferrate with high Na content as a Na-rich cathode material for Na-ion batteries. *Nano Research* **2015,** 8, (1), 117-128.

39. Kim, Y.; Ha, K. H.; Oh, S. M.; Lee, K. T., High-Capacity Anode Materials for Sodium-Ion Batteries. *Chemistry-A European Journal* **2014,** 20, (38), 11980-11992.

40. Ortiz-Vitoriano, N.; Drewett, N. E.; Gonzalo, E.; Rojo, T., High performance manganese-based layered oxide cathodes: overcoming the challenges of sodium ion batteries. *Energy & Environmental Science* **2017,** 10, (5), 1051-1074.

41. Ellis, B. L.; Nazar, L. F., Sodium and sodium-ion energy storage batteries. *Current Opinion in Solid State and Materials Science* **2012,** 16, (4), 168-177.

42. Alcántara, R.; Jaraba, M.; Lavela, P.; Tirado, J., $NiCo_2O_4$ spinel: First report on a transition metal oxide for the negative electrode of sodium-ion batteries. *Chemistry of Materials* **2002,** 14, (7), 2847-2848.

43. Jiang, Y.; Hu, M.; Zhang, D.; Yuan, T.; Sun, W.; Xu, B.; Yan, M., Transition metal oxides for high performance sodium ion battery anodes. *Nano Energy* **2014,** 5, 60-66.

44. Xiong, H.; Slater, M. D.; Balasubramanian, M.; Johnson, C. S.; Rajh, T., Amorphous TiO_2 nanotube anode for rechargeable sodium ion batteries. *The journal of physical chemistry letters* **2011,** 2, (20), 2560-2565.

45. Oh, S.-M.; Hwang, J.-Y.; Yoon, C.; Lu, J.; Amine, K.; Belharouak, I.; Sun, Y.-K., High electrochemical performances of microsphere C-TiO_2 anode for sodium-ion battery. *ACS applied materials & interfaces* **2014,** 6, (14), 11295-11301.

46. Usui, H.; Yoshioka, S.; Wasada, K.; Shimizu, M.; Sakaguchi, H., Nb-doped rutile TiO_2: a potential anode material for Na-ion battery. *ACS applied materials & interfaces* **2015,** 7, (12), 6567-6573.

47. Zhu, Y.; Han, X.; Xu, Y.; Liu, Y.; Zheng, S.; Xu, K.; Hu, L.; Wang, C., Electrospun Sb/C fibers for a stable and fast sodium-ion battery anode. *ACS nano* **2013,** 7, (7), 6378-6386.

48. Zhao, Y.; Manthiram, A., High-capacity, high-rate Bi–Sb alloy anodes for lithium-ion and sodium-ion batteries. *Chemistry of Materials* **2015,** 27, (8), 3096-3101.

49. Chevrier, V.; Ceder, G., Challenges for Na-ion negative electrodes. *Journal of The Electrochemical Society* **2011,** 158, (9), A1011-A1014.

50. Dai, Z.; Mani, U.; Tan, H. T.; Yan, Q., Advanced Cathode Materials for Sodium-Ion Batteries: What Determines Our Choices? *Small Methods* **2017**.

51. Ko, J. S.; Doan-Nguyen, V. V.; Kim, H.-S.; Petrissans, X.; DeBlock, R. H.; Choi, C. S.; Long, J. W.; Dunn, B. S., High-rate capability of Na_2FePO_4F nanoparticles by enhancing surface carbon functionality for Na-ion batteries. *Journal of Materials Chemistry A* **2017,** 5, (35), 18707-18715.

52. Cui, D.; Chen, S.; Han, C.; Ai, C.; Yuan, L., Carbothermal reduction synthesis of carbon coated Na_2FePO_4F for lithium ion batteries. *Journal of Power Sources* **2016,** 301, 87-92.

53. Park, Y.-U.; Seo, D.-H.; Kwon, H.-S.; Kim, B.; Kim, J.; Kim, H.; Kim, I.; Yoo, H.-I.; Kang, K., A new high-energy cathode for a Na-ion battery with ultrahigh stability. *Journal of the American Chemical Society* **2013,** 135, (37), 13870-13878.

54. Xu, M.; Xiao, P.; Stauffer, S.; Song, J.; Henkelman, G.; Goodenough, J. B., Theoretical and experimental study of vanadium-based fluorophosphate cathodes for rechargeable batteries. *Chemistry of Materials* **2014,** 26, (10), 3089-3097.

55. Hautier, G.; Jain, A.; Chen, H.; Moore, C.; Ong, S. P.; Ceder, G., Novel mixed polyanions lithium-ion battery cathode materials predicted by high-throughput ab initio computations. *Journal of Materials Chemistry* **2011,** 21, (43), 17147-17153.

56. Chen, H.; Hautier, G.; Jain, A.; Moore, C.; Kang, B.; Doe, R.; Wu, L.; Zhu, Y.; Tang, Y.; Ceder, G., Carbonophosphates: a new family of cathode materials for Li-ion batteries identified computationally. *Chemistry of Materials* **2012,** 24, (11), 2009-2016.

57. Chen, H.; Hao, Q.; Zivkovic, O.; Hautier, G.; Du, L.-S.; Tang, Y.; Hu, Y.-Y.; Ma, X.; Grey, C. P.; Ceder, G., Sidorenkite ($Na_3MnPO_4CO_3$): a new intercalation cathode material for Na-ion batteries. *Chemistry of Materials* **2013,** 25, (14), 2777-2786.

58. Nose, M.; Nakayama, H.; Nobuhara, K.; Yamaguchi, H.; Nakanishi, S.; Iba, H., $Na_4Co_3(PO_4)_2P_2O_7$: A novel storage material for sodium-ion batteries. *Journal of Power Sources* **2013,** 234, 175-179.

59. Lim, S. Y.; Kim, H.; Chung, J.; Lee, J. H.; Kim, B. G.; Choi, J.-J.; Chung, K. Y.; Cho, W.; Kim, S.-J.; Goddard, W. A., Role of intermediate phase for stable cycling of $Na_7V_4(P_2O_7)_4PO_4$ in sodium ion battery. *Proceedings of the National Academy of Sciences* **2014,** 111, (2), 599-604.

60. Delmas, C.; Braconnier, J.-J.; Fouassier, C.; Hagenmuller, P., Electrochemical intercalation of sodium in NaxCoO2 bronzes. *Solid State Ionics* **1981,** 3, 165-169.

61. Delmas, C.; Fouassier, C.; Hagenmuller, P., Structural classification and properties of the layered oxides. *Physica B+ C* **1980,** 99, (1-4), 81-85.

62. Yabuuchi, N.; Komaba, S., Recent research progress on iron-and manganese-based positive electrode materials for rechargeable sodium batteries. *Science and technology of advanced materials* **2014,** 15, (4), 043501.

63. Shannon, R. D., Revised effective ionic radii and systematic studies of interatomic distances in halides and chalcogenides. *Acta crystallographica section A: crystal physics, diffraction, theoretical and general crystallography* **1976,** 32, (5), 751-767.

64. Ren, W.; Zhu, Z.; An, Q.; Mai, L., Emerging Prototype Sodium-Ion Full Cells with Nanostructured Electrode Materials. *small* **2017**.

65. Ming, J.; Ming, H.; Yang, W.; Kwak, W.-J.; Park, J.-B.; Zheng, J.; Sun, Y.-K., A sustainable iron-based sodium ion battery of porous carbon–Fe_3O_4/$Na_2FeP_2O_7$ with high performance. *RSC Advances* **2015,** 5, (12), 8793-8800.

66. Oh, S.-M.; Myung, S.-T.; Yoon, C. S.; Lu, J.; Hassoun, J.; Scrosati, B.; Amine, K.; Sun, Y.-K., Advanced $Na[Ni_{0.25}Fe_{0.5}Mn_{0.25}]O_2$/C–$Fe_3O_4$ sodium-ion batteries using EMS electrolyte for energy storage. *Nano letters* **2014,** 14, (3), 1620-1626.

67. Hasa, I.; Hassoun, J.; Sun, Y. K.; Scrosati, B., Sodium-Ion Battery based on an Electrochemically Converted $NaFePO_4$ Cathode and Nanostructured Tin–Carbon Anode. *ChemPhysChem* **2014,** 15, (10), 2152-2155.

68. Ye, H.; Wang, Y.; Zhao, F.; Huang, W.; Han, N.; Zhou, J.; Zeng, M.; Li, Y., Iron-based sodium-ion full batteries. *Journal of Materials Chemistry A* **2016,** 4, (5), 1754-1761.

69. Smith, K.; Treacher, J.; Ledwoch, D.; Adamson, P.; Kendrick, E., Novel High Energy Density Sodium Layered Oxide Cathode Materials: from Material to Cells. *ECS Transactions* **2017,** 75, (22), 13-24.

70. Noguchi, Y.; Kobayashi, E.; Plashnitsa, L. S.; Okada, S.; Yamaki, J.-i., Fabrication and performances of all solid-state symmetric sodium battery based on NASICON-related compounds. *Electrochimica Acta* **2013,** 101, 59-65.

71. Kobayashi, E.; Plashnitsa, L. S.; Doi, T.; Okada, S.; Yamaki, J.-i., Electrochemical properties of Li symmetric solid-state cell with NASICON-type solid electrolyte and electrodes. *Electrochemistry Communications* **2010,** 12, (7), 894-896.

72. Guo, S.; Yu, H.; Liu, P.; Ren, Y.; Zhang, T.; Chen, M.; Ishida, M.; Zhou, H., High-performance symmetric sodium-ion batteries using a new, bipolar O3-type material, $Na_{0.8}Ni_{0.4}Ti_{0.6}O_2$. *Energy & Environmental Science* **2015,** 8, (4), 1237-1244.

CHAPTER II

Experimental Section

This Chapter gives the methods, chemicals and measurement techniques used for the LIB and NIBs study.

2.1 Chemicals

2.1.1 $LiMnPO_4$

$LiMnPO_4$ nanoparticles are prepared by colloidal synthesis, carbon coating process is achieved by pyrolysis in Ar_2 at 450°C for 1h. The chemicals involved in the preparation route are shown in **Table 2.1**, and they have been used as received from the supplier.

Table 2.1 Precursors used for carbon-coated $LiMnPO_4$ nanoparticles.

Chemicals and Solvents	Supplier	Synthesis
Manganese chloride anhydrous (99.99% purum)-$MnCl_2$	Sigma Aldrich	Colloidal
Ammonium phosphate dibasic ((≥99.0% purum, LOT#BCBD7253V)-$(NH_4)_2HPO_4$	Sigma Aldrich	
Lithium iodide (99.99% purum, LOT#MKBN9943V)-LiI	Sigma Aldrich	
Oleylamine (OAm, 70% purum, LOT#STBF0846V)	Sigma Aldrich	
1–octadecene (technical grade, 90%, LOT#MKBS8289V)	Sigma Aldrich	
α–D–glucose (99.5 % purum, LOT#089K00603)	Sigma Aldrich	Solid state

2.1.2 Layered P2-$Na_{0.45}Ni_{0.26}Mn_{0.76}O_2$ (NaNMO)

Layered NaNMO sample is prepared through colloidal assisted-solid state reaction. $Ni_{0.25}Mn_{0.75}O$ nanoparticles are achieved by colloidal synthesis then followed by a sodiation process via solid state reaction. The chemicals employed for the synthesis are shown in **Table 2.2**.

Table 2.2 Precursors used for NaNMO sample

Chemicals and Solvents	Supplier	Synthesis
Manganese (II) Acetylacetonate (LOT#MKBS6814 V)	Sigma Aldrich	Colloidal
Nickel (II) Acetylacetonate (95%, LOT#MKBT0868V)	Sigma Aldrich	
Sodium Carbonate (LOT#BCBH1569 V)	Sigma Aldrich	Solid State
Oleylamine (OLAM, 70% purum, LOT#STBF4991 V)	Sigma Aldrich	Colloidal
1-Octadecene (ODE, technical grade, 90%, LOT# MKBT0768 V)	Sigma Aldrich	Colloidal
Sodium Percholorate ($NaClO_4$, 98.0%-102%, anhydrous, LOT#Y21A005)	Sigma Aldrich	Colloidal

2.1.3 Layered P2- $Na_xNi_{x/2}Ti_{1-x/2}O_2$ ($0.60 \leq x \leq 1.0$) (NaNTO)

Two different techniques (colloidal-assisted solid state reaction and full solid state reaction) are explored and compared to prepare NaNTO sample. The colloidal-assisted solid state reaction is following the similar procedure of NaNMO sample. The full solid-state reaction is achieved by mix Na_2CO_3, TiO_2 and NiO. The chemicals are shown in **Table 2.3** and Table 2.4, respectively.

Table 2.3 Precursors used for colloida-assisted solid-state synthesis for NaNTO sample

Chemicals and Solvents	Supplier	Synthesis
Octadecanol (ODAL, 95%,)	Sigma Aldrich	Colloidal
Oleic acid (OLAC)	Sigma Aldrich	
Octadecene (technical grade, 90%, LOT# MKBT0768 V)	Sigma Aldrich	

Oleylamine (OLAM, OLAM, 70% purum, LOT#STBF4991 V)	Sigma Aldrich	
Titanium ethoxide(TEO, LOT# 3087363)	Sigma Aldrich	
Titanium Choloride ($TiCl_4$)	Sigma Aldrich	
Nickel choloride ($NiCl_2$)	Sigma Aldrich	
Sodium Carbonate (LOT#BCBH1569 V)	Sigma Aldrich	Solid State

Table 2.4 Chemicals used for full solid-state synthesis of NaNTO sample

Chemicals and Solvents	Supplier	Synthesis
TiO_2	Sigma Aldrich	Solid State
Nickel (II) Oxide (NiO)	Sigma Aldrich	
Sodium Carbonate (LOT#BCBH1569 V)	Sigma Aldrich	
Sodium Percholorate ($NaClO_4$, 98.0%-102%, anhydrous, LOT#Y21A005)	Sigma Aldrich	Colloidal

The preparation details of the three samples will be reported in Chapter III, IV and V respectively.

2.2 Sample characterization

X-ray Diffraction (XRD): XRD patterns were recorded on a Rigaku SmartLab X-ray powder diffractometer equipped with a 9 kW CuKα rotating anode, operating at 40 kV and 150 mA. A Göbel mirror was used to convert the divergent X-ray beam into a parallel beam and to suppress the Cu Kβ radiation. The ex-situ diffraction patterns were collected under inert atmosphere of nitrogen using an Anton Paar domed sample holder (DSH). The *in-operando* XRD diffraction experiments were collected in Bragg-Brentano para-focusing geometry, using a homemade cell attachment a D/teX Ultra ID silicon strip detector set in X-ray fluorescence reduction mode. The cell were cycled at a constant current of 50 µA.

Electron Diffraction Tomography(EDT): EDT experiments were performed on a Zeiss Libra 120 operating at 120 kV and equipped with LaB_6 electron source, in-column omega filter for energy filtered imaging and a Nanomegas Digistar P1000 device for precession electron diffraction. In the

EDT experiment, the TEM sample was obtained by crushing in an agatha mortar a small piece of Eu-doped silica sample. The obtained powder was dispersed in isopropanol and sonicated. After sonication a drop of the dispertion was deposited on a carbon-coated copper grid. Data analysis, including 3D diffraction volume reconstruction, cell parameter determination and reflection integration, was performed by *PETS* software[1]. Structure solution was performed by direct methods implemented in the program *SIR2014*[2].

High Resolution Scanning Electron Microscopy (HRSEM) and Energy Dispersive X-ray spectroscopy (EDS)*:* HRSEM analysis was carried out using a JEOL JSM 7500FA scanning electron microscope, equipped with a cold field emission gun (single crystal tungsten <310> emitter, ultimate resolution of 1nm). Images were acquired at 10kV, using an in-lens secondary electron (SE) detector and a 2-segment solid state annular backscattered electron (BSE) detector. EDS analysis was performed using an Oxford X-max LN2-free Silicon Drift Detector (SDD), with 80mm2 of sensor active area and 129eV of energy resolution at 5.9keV (MnKα). The Extended Pouchou and Pichoir (XPP) matrix correction algorithm included in the Oxford AZtec software was used to analyze the data. Samples were prepared by drop casting the solution on ultra-flat 5x5 mm (type P) silicon substrates.

X-ray photoelectron spectroscopy (XPS): XPS was carried out with an Axis Ultra DLD spectrometer equipped with a monochromatic Al Kα X-ray source (1486.6 eV photon energy). Charge compensation was applied and energy scale calibration was performed setting the C-C/C-H carbon C 1s peak at 248.8 eV. High-resolution spectra were acquired with a step of 0.1 eV and pass energy of 10 eV.

High resolution TEM (HRTEM): HRTEM was acquired on a JEOL 2200FS microscope working at 200 kV. The aberration corrector (CEOS) of the objective lens was set at negative spherical aberration and small overfocus to give bright contrast on the Mn/Ni columns in the case of very thin flakes (few nm in thickness) for the NaNMO sample.

Thermogravimetric Analysis (TGA): TGA measurement helps to quantify the fraction of carbon content in LMP and NaNMO. The thermal analysis was performed using a TGA Q500 instrument, from room temperature (RT) to 700 °C (equilibration time 5 min at 30 °C, heating rate 5 °C/min) in air flux.

2.3 Electrodes preparation, cells configuration and electrochemical characterization

2.3.1 Electrodes preparation

The electrochemical characterization of samples was carried out on composite electrodes with the following formulation: 85 or 80 wt.% of active material, 10 wt.% of conductive carbon (Super P) and 5 or 10 wt.% of PVdF (Polyvinylidene Fluoride). The electrodes were prepared by blade-casting a N-methyl pyrrolidone (NMP) based slurry of the three components, on aluminum foil used as current collector for cathode and cupper foil for anode. Before casting of the slurry, the aluminum foil underwent etching procedure in 1 M KOH solution for 60 seconds. Circular electrodes (geometric area of 1.77 cm^2) were cut from the dried depositions, pressed and further dried at 120 °C under vacuum for at least 2 hours before use, the preparation process are shown in **Figure 2.1**.

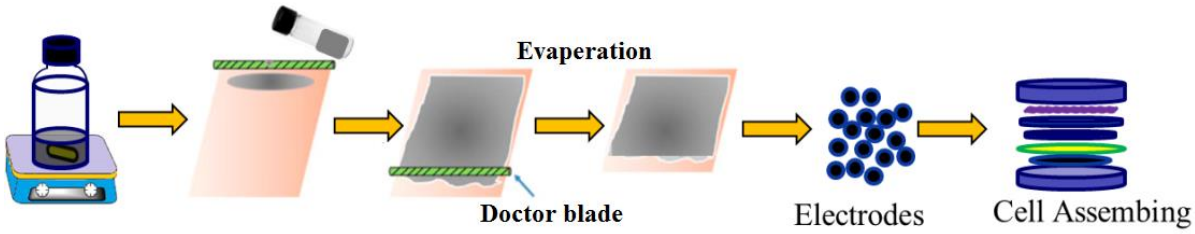

Figure 2.1. The scheme of electrodes preparation process

2.3.2 Cells configuration: It involves two types of cell configuration in this thesis. The two-electrode coin-type cell and the three-electrodes Swagelok cell.

Coin-type (2032) electrochemical cells (**Figure 2.2**a and c): The coin-type cell is a two-electrodes electrochemical testing system (Figure 2.2a). The diameter of the circular electrode for the coin-type cell is 15 mm, the active material mass loading for the tested electrodes was around 2 mg/cm^2. Metallic Li/Na disk was employed as both counter and reference electrode. All the 2032 cells have been assembled and sealed in an argon filled glove box (MBraun, with H_2O and O_2 <0.1 ppm). A dried glass fiber membrane (Whatman GF/D) was used as separator wetted with electrolyte solution (200µL).

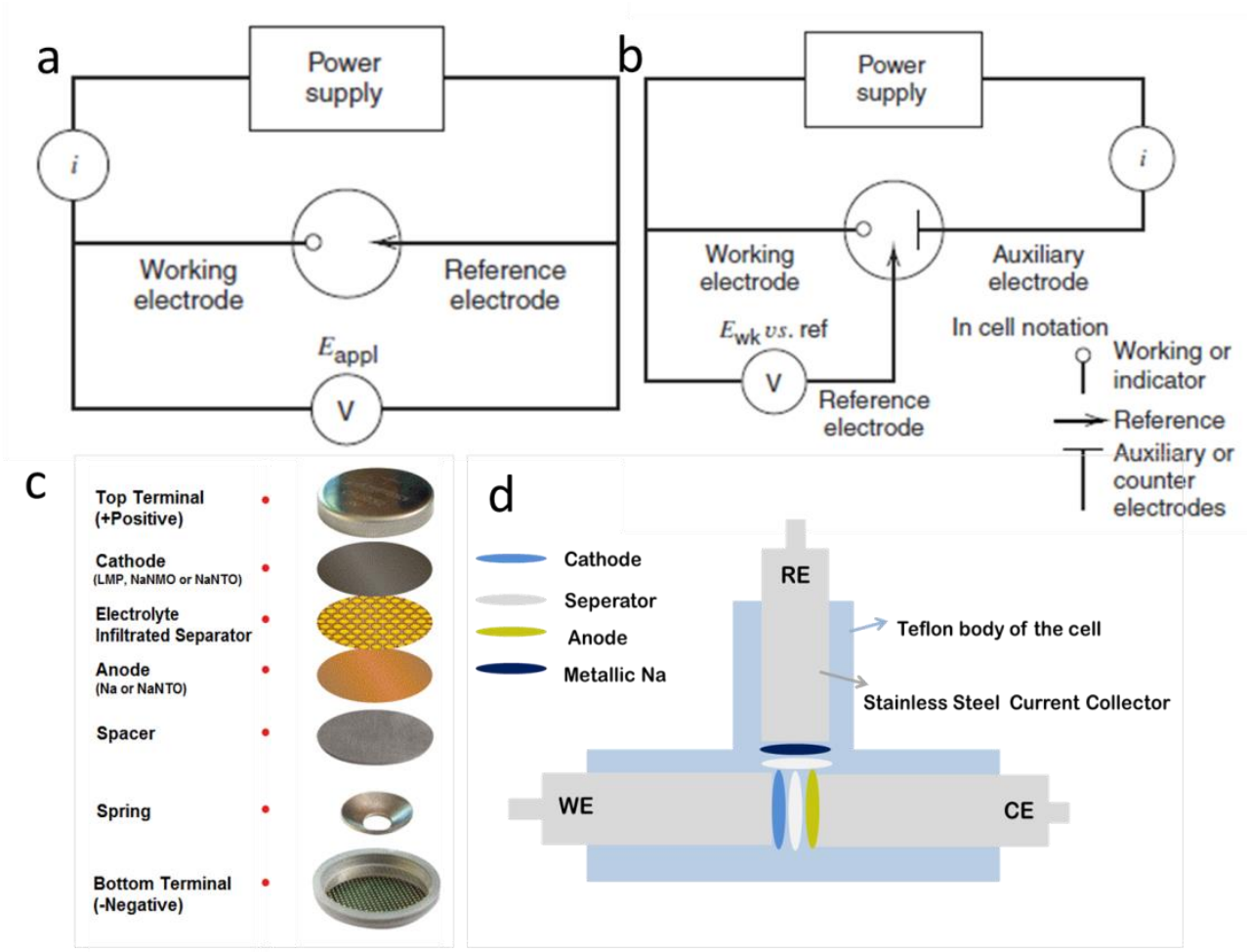

Figure 2.2: Schematic representation of a. two-electrodes system[3] (c. "coin-type") and b. three-electrodes system[3] (d. "Swagelok-type" electrochemical cell).

Swagelok-type electrochemical cell (Figure 2.2b and d): Swagelok-type cell is a typical three-electrodes testing system (Figure 2.2b), in which working, counter and reference electrode are arranged in a "T" geometrical configuration. In this system, the device is used to measure the potential difference between the working electrode (WE) and reference electrode (RE), which has a high input impedance, so that a negligible current is drawn trough the RE. The diameter of the circular electrode for the Swagelok-type cell is 12 mm, the active material mass loading for the tested electrodes was around 1.3 mg cm^{-2}. The three-electrodes cell, in which the metallic Li/Na disk as only the reference electrode, was assembled and sealed in an argon filled glove box (MBraun, with H_2O and O_2 <0.1 ppm). A dried glass fiber membrane (Whatman GF/D) was used as separator wetted with electrolyte solution (250µL).

2.3.3 Electrochemical Characterization

Cyclic Voltammetry (CV) measurements: Cyclic voltammetry has become an important and widely used electrochemical analysis technique in the battery field. By varying the applied potential at a working electrode in both forward and reverse direction (at a constant scan rate), as shown in **Figure 2.3**a, the CV technique records the current versus time as a function of potential, as shown in Figure 2.3b. Cyclic Voltammetry is a useful technique for initial electrochemical studies of new systems. When an electrochemically active compound A is present in the solution, an anodic current peak at the potential Ep,a is detected with the current $i_{p,a}$, because of the reaction: $A + e \rightarrow A^-$. When the potential is swept back during the reverse scan, a cathodic current peak may be observed at Ep,c with a current $i_{p,c}$ with the reaction: $A^- - e \rightarrow A$. The important parameters in CV are the peak potentials ($E_{p,c}$, $E_{p,a}$) and peak current (i_{pc} and i_{pa}) of the cathodic and anodic peaks, respectively. If the electron transfer process is fast compared with other processes (such as diffusion), the reaction is said to be electrochemically reversible[4].

The value of the peak separation[4-6]

$$\Delta E_p = \left| E_{pa} - E_{pc} \right| = 2.03RT/nF$$

(n is the number of electrons transferred per molecule, R is the gas constant, T is the absolute temperature and F is Faraday constant) is a measure of the reversibility. For the reversible diffusion-controlled redox reaction at 25°C with n electrons ΔE_p in principle should be 0.0592/nF and the magnitude of the peak current for a reversible electron transfer is given by Randles-Sevcik equation[4, 7]

$$i_p = 2.686*10^5\ n^{2/3}\ AC^*D^{1/2}v^{1/2}$$

where A is the electrode area (cm^2), D is the diffusion coefficient (cm^2s^{-1}), C* is the concentration in mol cm^{-3}, and v is the scan rate in V s^{-1}. CV gives information on the possible redox reactions of the system, including the Faradic insertion and extraction reaction and has proven very useful in obtaining information about fairly complicated electrode reactions[3].

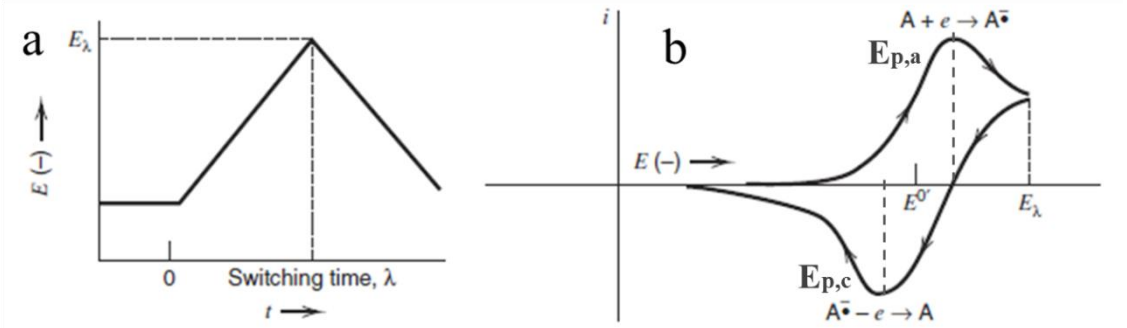

Figure 2.3 (a) cyclic potential sweep. (b) Resulting cycling voltammogram.

***Galvanostatic technique*[8]:** In this technique, a controlled continuous current is applied to the working electrode, by means of a current generator (called a galvanostat). At the same time, electrochemical potential fluctuations are monitored between the working and reference electrodes, whose potential is assumed to be constant, as shown in **Figure 2.4**a. The IR loss (Ohmic drop) is the main reason for the abruptly potential change at the moment when the current is first applied.

Galvanostatic techniques (e.g. Galvanostatic Cycle with Potential Limitation, GCPL and Galvanostatic Intermittent Titration Technique, GITT), have become widely accepted standard procedures for battery material electrochemical characterization. They provide qualitative information concerning the mechanisms accountable for material energy storage, as well as quantitative detail about stoichiometric modification of the alkali ion hosting species.

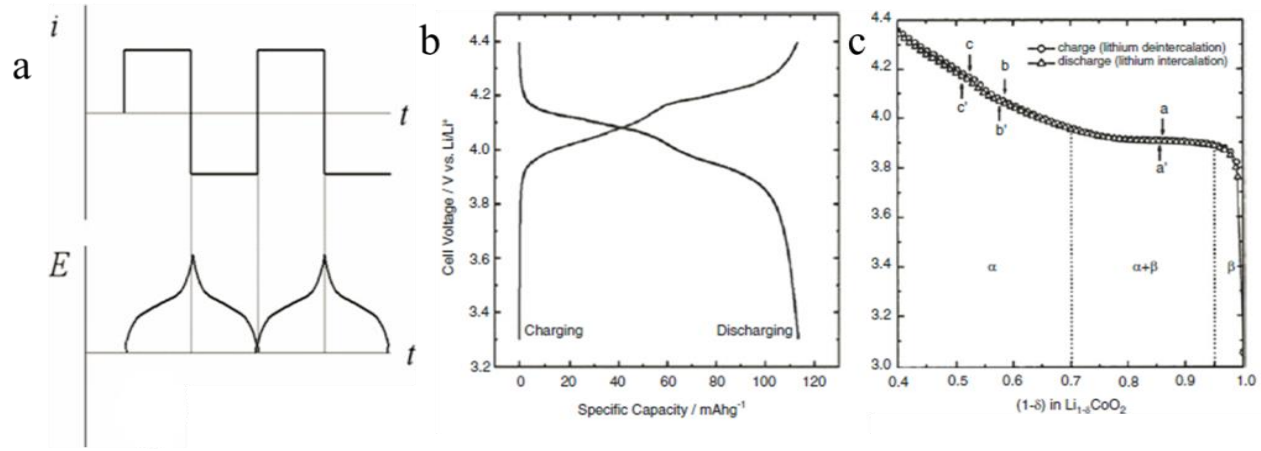

Figure 2.4 a). Cyclic chronopotentiometry; b) Galvanostatic charge/discharge curve of $LiMn_2O_4$ [9]and c) open-circuit potential versus lithium stoichiometry plot of $LiCoO_2$[10].

In a GCPL measurement, the electroactive species will be oxidized/reduced when the constant anodic/cathodic current is applied to the electrode. The electrode potential changes with time according to the change of the concentration ratio of reactant to product at the electrode surface. After the concentration of the reactant drops to zero at the electrode surface, there's not enough reactant to be supplied to the surface to accept all of the electron that being forced by the application of a constant current. The electrode potential will then sharply change to more anodic/cathodic values. If the current changes from an anodic to cathodic one, the product that formed by the anodic reaction starts to be reduced. Then the potential moves in the cathodic directions as the concentration of the cathodic product increases. The current in repeatedly reversed in the cyclic chronopotentiometry and potential changes correspondingly as shown in Figure 2.4a. The shape of the curves is governed by the reversibility of the electrode reaction.

GCPL technique is used to estimate the specific capacity and to evaluate the cycling stability of the battery, respectively. A typical galvanostatic charge/discharge profile of $LiMn_2O_4$[9] at a rate of 0.2C (*n*C rate[3] means the discharging/charging rate at which the battery is virtually fully discharged/discharged for 1/*n* h) is shown in Figure 2.4b. The total quantity charge available from a fully charged cell (or storable in a fully discharged cell) can be calculated at a specific C rate from the charge transferred during the discharging or charging process in terms of mAh g^{-1}. Alternatively, the quantity of the electricity can be converted to the number of moles of inserted atoms as long as the electrode potential is obtained in a (quasi-) equilibrium state as shown in Figure 2.4c[10].

A different capacity curve is a plot of dQ/dV vs. voltage as shown in **Figure 2.5**, which presents the differential capacity curves (dQ/dV) from GCPL tests on an electrochemical cell consisting of graphite and lithium metal. The data are derived from the galvanostatic charge/discharge profile in Figure 2.4b. dQ/dV vs. voltage curves are useful to measure the specific voltage of electrochemical reactions accurately.

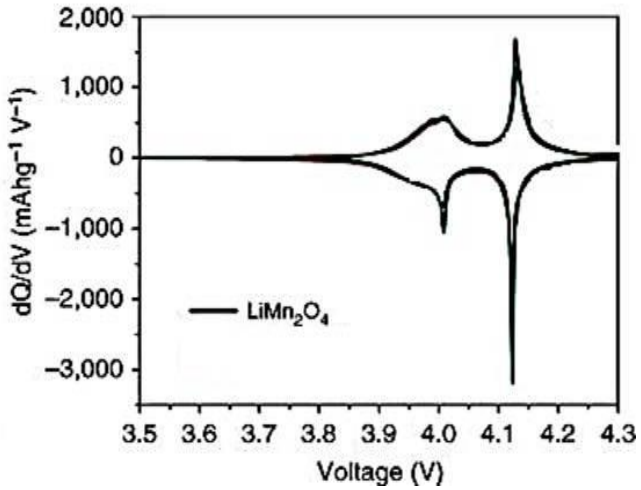

Figure 2.5. Different capacity curves derive from the galvanostatic charge/discharge profile of $LiMn_2O_4$ in Figure 2.4b.

***Electrochemical impedance Spectroscopy (EIS) measurements*:** EIS[11] is usually measured by applying an AC (Alternating Current) potential to an electrochemical cell and then measure the current through the cell. The measurement normally is done by using a small excitation signal of a very low amplitude, so the cell's response is linear. Then the current response to a potential ($E = E_0 \exp(j\omega t)$, E_0 is the amplitude of signal, ω is the radial frequency) in this system will be a sinusoidal following $I = I_0 \exp(j\omega t - \phi)$ (ϕ: phase shift) as shown in **Figure 2.6**.

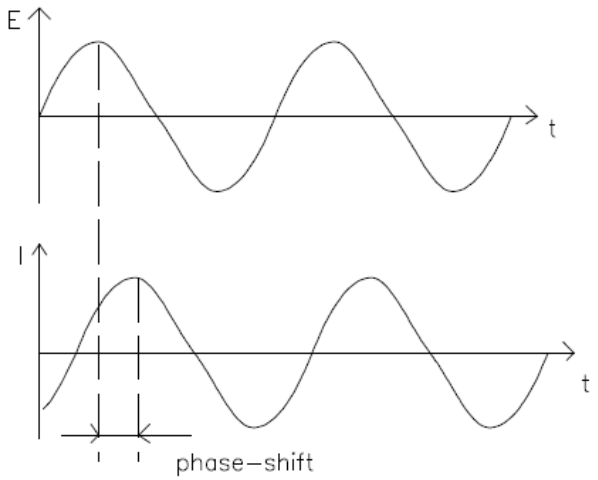

Figure 2.6. Sinusoidal current response in a linear system[11].

The impedance is then represented as $Z = E/I = Z_0 \exp(j\phi)$ according to Ohm's Law. With the Eulars relationship,

$$\exp(j\phi) = \cos\phi + j \sin\phi$$

The impedance can be represented as $Z(\omega) = E/I = Z_0 \exp(j\phi) = Z_0 (\cos\phi + j \sin\phi)$, means the impedance $Z(\omega)$ is composed of a real and an imaginary part. If the real part is plotted on the X-axis and the imaginary part is plotted on the Y-axis, then we can obtain the 'Nyquist Plot'.

EIS has been extensively used to analyze lithium battery systems, especially to predict the behavior of the batteries, and to determine the factors of limiting the performance of an electrode including its conductivity, charge-transfer properties, properties of the passivating layer, etc[12].

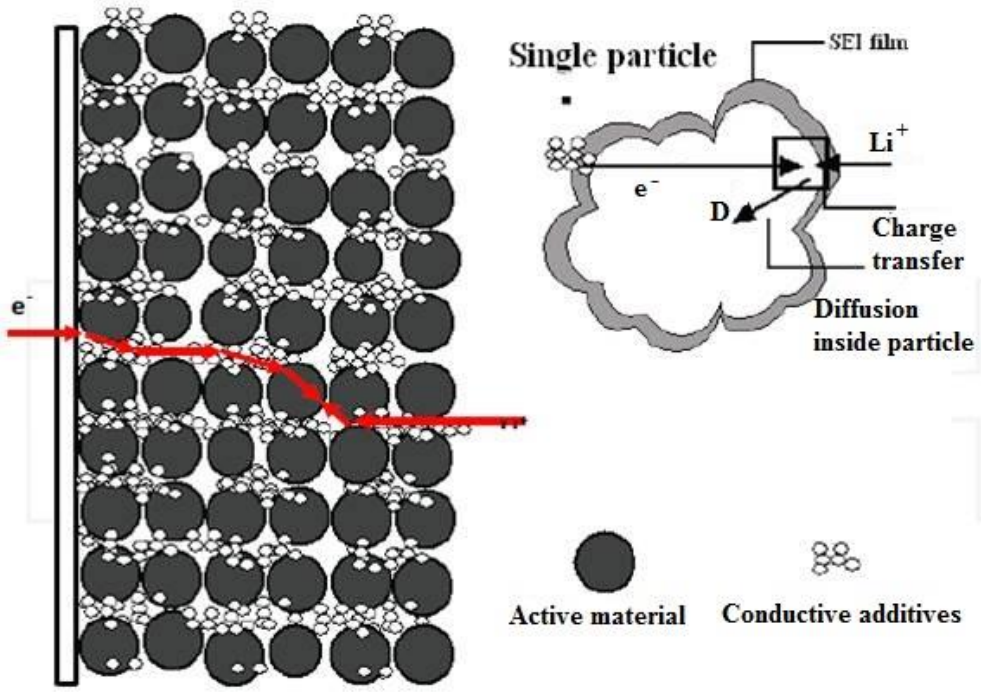

Figure 2.7. Kinetically relevant steps of electrochemical intercalation into the porous layer of intercalation materials.

Barsoukov et al[13, 14] proposed a model based on single particles for commercial composite electrode, as shown in **Figure. 2.7**. They supposed that the electrochemical kinetics characteristic of battery materials were presented by several common steps: (i) ionic charge conduction through electrolyte in the pores of the active layer and electronic charge conduction through the conductive part of the active layer; (ii) lithium-ion diffusion through the surface insulating layer of the active

material and the lithium-ion diffusion in the solid phase; (iii) electrochemical reaction on the interface of active material particles (charge transfer); (iv) phase-transfer in case where several phases are present and (v) a capacitive behavior that is related to the occupation of lithium ions[15].

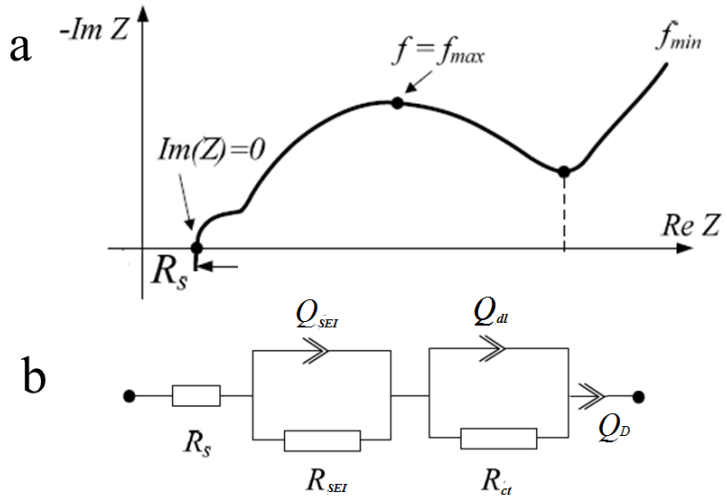

Figure 2.8. a) Typical Nyquist plot of Li-ion battery and b) The corresponding equivalent circuit used for curve fitting the Nyquist plot of Li-ion battery[16].

The EIS spectra (Nyquist plot) of a battery in the frequency range 10^{5}-10^{-2} Hz is presented in **Figure 2.8**a. It can be interpreted in terms of the following physical phenomena[13,16, 17] in an order of decreasing frequency: (i) a value of the ohmic resistance R*s* of the battery; (ii) the semicircles within the mid-high frequency window display of double layers on the materials within the electrode and the contribution of different resistance which can be caused by the electrode materials and the presence of the resistive film as shown in Figure 2.7. The middle frequency semicircle usually associated with charge transfer, and finally, an (iii) a very low frequency inclined line attributed to the Warburg impedance relates to the diffusion within the electrolyte and active material[12]. It is controlled bu the diffusion coefficients and the particle size for the electrode material. The electrical equivalent circuits[15, 16] is illustrated in Figure 2.8b, R*s* represents the ohmic resistance, R_{SEI} and R*ct* are resistances of the SEI film and the charge transfer reaction. The capacitance of the SEI film and the capacitance of the double layer are represented by the constant phase elements (CPE, it is physically interpreted as an effect of the surface roughness of the sample, leading to an heterogeneity of the capacitance[18]) Q_{SEI} and Q_{dl}, respectively. The very low frequency

region, however, cannot be modelled properly with a finite Warburg element; therefore, it is chosen to replace the finite diffusion by a CPE, i.e., Q_D. Since the Warburg impedance corresponds to the lithium diffusion, it can be used to calculate the coefficient of Li^+ (D_{Li+}) as the following equation[19, 20]:

$$D_{Li+} = \frac{1}{2}\left[\left(\frac{V_M}{AF\sigma}\right)\frac{\delta E}{\delta x}\right]^2$$

Where A is the surface area of the active material, V_M is the molar volume of the material, F is the Faraday constant, $\frac{\delta E}{\delta x}$ is the differentiation of the differentiation of the open circuit voltage (E) vs. mobile Li^+ concentration (*x*). In the single-phase E is linearly related to x and the $\frac{\delta E}{\delta x}$ value is the slope of the corresponding line. σ is the Warburg factor and can be obtained from the slop of $|Z'|$ vs. $\omega^{-1/2}$ in the Warburg region. The equation[21] $D_{Li+} = R^2T^2/2A^2n^4F^4C^2\sigma^2$ is wildly to calculate the lithium ion diffusion coefficient , where R is the gas constant, T is the absolute temperature, n is the number of electrons per molecule during the oxidation/reduction and C is the lithium concentration.EIS analyses were performed in the range 100 kHz-100 mHz, with a perturbation amplitude of 5 mV and 10 points per decade.

The electrochemical tests were carried out with MPG-2 or VMP3 (BioLogic) potentiostats/galvanostats. All the measurements were done at room temperature (23 °C).

2.4 References

1. Palatinus, L., PETS–program for analysis of electron diffraction data. *Prague: Institute of Physics of the AS CR* **2011**.

2. Burla, M. C.; Caliandro, R.; Carrozzini, B.; Cascarano, G. L.; Cuocci, C.; Giacovazzo, C.; Mallamo, M.; Mazzone, A.; Polidori, G., Crystal structure determination and refinement via SIR2014. *Journal of Applied Crystallography* **2015,** 48, (1), 306-309.

3. Bard, A. J.; Faulkner, L. R.; Leddy, J.; Zoski, C. G., *Electrochemical methods: fundamentals and applications*. wiley New York: 1980; Vol. 2.

4. Settle, F. A., *Handbook of instrumental techniques for analytical chemistry*. Prentice Hall PTR: 1997.

5. Bard, A. J.; Inzelt, G.; Scholz, F., *Electrochemical dictionary*. Springer Science & Business Media: 2008.

6. Park, J.-K., *Principles and applications of lithium secondary batteries*. John Wiley & Sons: 2012.

7. Randles, J., TRANS FARADAY SOC. *Trans. Faraday Soc.* **1948,** 44, 327.

8. Pyun, S.-I.; Shin, H.-C.; Lee, J.-W.; Go, J.-Y., *Electrochemistry of insertion materials for hydrogen and lithium*. Springer Science & Business Media: 2012.

9. Zhang, Y.; Shin, H.-C.; Dong, J.; Liu, M., Nanostructured $LiMn_2O_4$ prepared by a glycine-nitrate process for lithium-ion batteries. *Solid State Ionics* **2004,** 171, (1), 25-31.

10. Shin, H.-C.; Pyun, S.-I., Investigation of lithium transport through lithium cobalt dioxide thin film sputter-deposited by analysis of cyclic voltammogram. *Electrochimica acta* **2001,** 46, (16), 2477-2485.

11. Instruments, G., Basics of electrochemical impedance spectroscopy. *G. Instruments, Complex impedance in Corrosion* **2007**, 1-30.

12. Zhuang, Q.-C.; Qiu, X.-Y.; Xu, S.-D.; Qiang, Y.-H.; Sun, S.-G., Diagnosis of electrochemical impedance spectroscopy in lithium-ion batteries. In *Lithium Ion Batteries-New Developments*, InTech: 2012.

13. Barsoukov, E.; Macdonald, J. R., *Impedance spectroscopy: theory, experiment, and applications*. John Wiley & Sons: 2005.

14. Barsoukov, E.; Kim, J. H.; Kim, J. H.; Yoon, C. O.; Lee, H., Kinetics of lithium intercalation into carbon anodes: in situ impedance investigation of thickness and potential dependence. *Solid State Ionics* **1999,** 116, (3), 249-261.

15. Zhuang, Q.-C.; Wei, T.; Du, L.-L.; Cui, Y.-L.; Fang, L.; Sun, S.-G., An electrochemical impedance spectroscopic study of the electronic and ionic transport properties of spinel LiMn2O4. *The Journal of Physical Chemistry C* **2010,** 114, (18), 8614-8621.

16. Stroe, D. I.; Swierczynski, M.; Stan, A. I.; Knap, V.; Teodorescu, R. In *Diagnosis of lithium-ion batteries state-of-health based on electrochemical impedance spectroscopy technique*, Energy Conversion Congress and Exposition (ECCE), 2014 IEEE, 2014; IEEE: 2014; pp 4576-4582.

17. EROL, S. ELECTROCHEMICAL IMPEDANCE SPECTROSCOPY ANALYSIS AND MODELING OF LITHIUM COBALT OXIDE/CARBON BATTERIES. Citeseer, 2015.

18. La, T. m. i. e. http://www.bio-logic.net/wp-content/uploads/20120817-Application-note-42.pdf

19. Xia, H.; Lu, L.; Ceder, G., Li diffusion in LiCoO 2 thin films prepared by pulsed laser deposition. *Journal of Power Sources* **2006,** 159, (2), 1422-1427.

20. Xia, H.; Meng, S. Y.; Lu, L.; Ceder, G., Electrochemical Behavior and Li Diffusion Study of $LiCoO_2$ Thin Film Electrodes Prepared by PLD. **2007**.

21. Zhang, Z.; Zhou, Z.; Nie, S.; Wang, H.; Peng, H.; Li, G.; Chen, K., Flower-like hydrogenated TiO 2 (B) nanostructures as anode materials for high-performance lithium ion batteries. *Journal of Power Sources.* **2014,** 267, 388-393.

CHAPTER III

Relevance of $LiPF_6$ as Etching Agent of $LiMnPO_4$ Colloidal Nanocrystals for High Rate Performing Li-ion Battery Cathodes

3.1 Introduction

As previously discussion in Chapter I, lithium transition metal phosphates with olivine structure have being studied as high-voltage cathode candidates for rechargeable lithium ion batteries, since almost 20 years[1]. Among their merits, there is the high chemical and thermal stability and the low cost of their precursors. Phosphates with an olivines crystal structure (belonging to orthorhombic space group *Pnma*) are characterized by the presence of longitudinal channels running parallel to crystallographic *b*-axis. These channels are suitable for lithium-ion intercalation and de-intercalation reactions that take place during the cathode discharge and charge processes, respectively.[2] For $LiFePO_4$ (LFP), the intercalation/de-intercalation process is biphasic (from $LiFePO_4$ to $FePO_4$ and *vice versa*) and is reversible. $LiMnPO_4$ (LMP) is more attractive than LFP among the other olivines, since it is has the same theoretical specific capacity as LFP (170 mAh g^{-1}), but is characterized by a higher working potential (4.1 V vs. Li^+/Li). The pervasive use of LMP would enable the development of batteries with energy densities that are approximately 20% higher than those based on LFP.[3, 4] However, low delivered capacity and cycling stability, and poor rate capability are the issues that LMP suffer from. These are mostly related to the low electronic conductivity (about two orders of magnitude lower than that of LFP)[5] and the poor Li^+ intercalation/de-intercalation kinetics. The latter arises from the pseudo Jahn-Teller distortion of the crystal lattice occurring at the interface between $LiMnPO_4$ and $MnPO_4$ during electrode cycling[4, 6, 7].

Many attempts have been made to overcome these limiting factors in olivine type materials for batteries. The poor electronic conductivity is usually improved by carbon coating,[6, 8-10] while working with nano-sized crystals helps to reduce the Li^+ diffusion length[11-15] and consequently

improves the ionic conductivity as introduced in Chapter I. Beneficial effects on the electrochemical performances are also seen by the incorporation of dopants, such as V,[16] Fe,[17] Ce,[18] Ni,[19] and Mg[20], that can buffer the pseudo Jahn-Teller distortion. To circumvent the effects of high electronic and ionic resistances, it is customary in the laboratory to adopt charge protocols for the cathode cycling tests (*i.e.* low currents and long charge times),[21-24] since a slower charging process maximizes the final achievable capacity. These conditions are however far from the realistic case in which an actual battery works and that requires fast charge processes. Only few reports on LMP-based cathodes have adopted fast charge protocols, and all of them based on a composite electrode formulations invariably containing a considerable fraction of carbon and polymeric binder (more than 25% in weight).[14, 15, 25] Also, carbon was present not only as coating layer but also in the form of additives (e.g. carbon black powders) that were deemed necessary to enhance the electric conductivity. At the cathodic working potentials, both binder and carbon are inactive for Li^+ intercalation/de-intercalation. Therefore, a mass of the active material that is, at best, only 75% of the total electrode mass, translates into an overall low energy density of the electrode.[26] These figures are far from the 4% wt. in total mass of conductive carbon and PVdF binder used in commercial electrodes based on active materials different from LFP and LMP.[27]

Our group developed a colloidal synthesis approach to $LiMPO_4$ (M=Fe, Mn) nanocrystals (NCs) and a subsequent surface treatment and a carbon coating procedure that delivered high performance LFP NCs-based cathodes.[28, 29] The treatment consisted in an etching of the NC surface with $LiPF_6$, which removed the organic ligands bound to the surface of the NCs and enabled then the formation of a compact carbon film in the following carbon coating step. Here, we have extended that procedure to LMP NCs, which, similarly to the LFP NCs of our previous work,[29] were prepared by a colloidal approach.

3.2 Experimental methods

3.2.1 Synthesis of $LiMnPO_4$ NCs

Colloidal LMP NCs were prepared with a procedure that was adapted from our previous reports on LFP NCs:[28, 29] 0.90 g of lithium iodide (LiI), 0.63 g of manganese(II) chloride ($MnCl_2$ anhydrous), 0.60 g of ammonium phosphate dibasic ($(NH_4)_2HPO_4$), 50 mL of oleylamine and 50 mL of 1-octadecene were mixed in a 250mL three-neck round bottom flask connected to a standard Schlenk line. The solution was degassed under vacuum for 4 hours at 120°C, after which it was heated

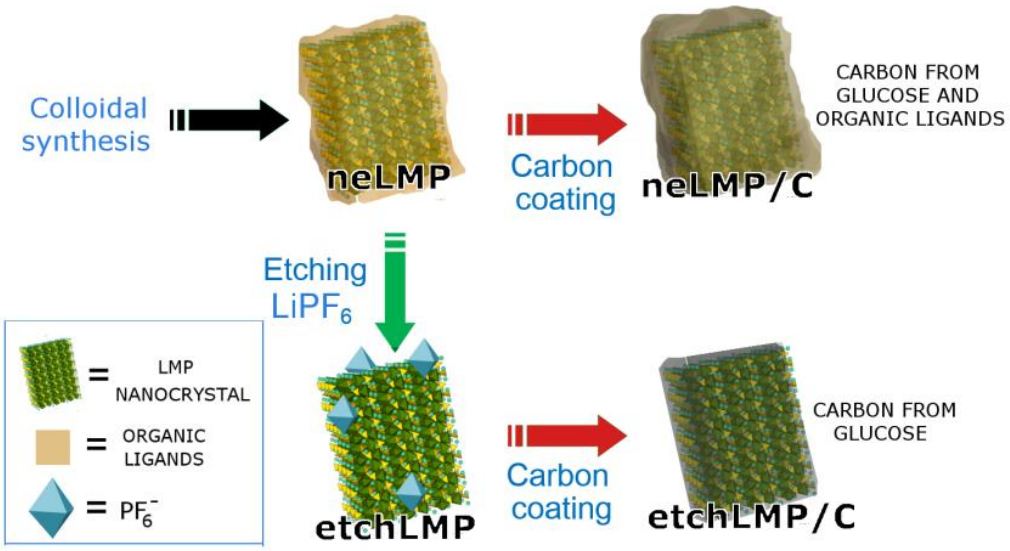

Scheme 3.1. Synthetic route to neLMP/C and etchLMP/C NCs. The scheme depicts the procedure used to prepare the neLMP/C particles (top right) by carbon coating of not etched NCs (neLMP, top left) and the etchLMP/C particles (bottom right) by carbon coating of etched NCs (etchLMP, bottom left).

overnight at 250 °C (heating rate 5°C/min) under N_2. It was then precipitated and cleaned by repeated additions of chloroform and ethanol followed by centrifugation at 9000 rpm.

3.2.2 $LiPF_6$ treatment

The as-synthesized LMP NCs (500 mg) were suspended in 10 mL of chloroform and mixed with 10 mL of 0.33 M lithium hexafluorophosphate ($LiPF_6$) aqueous solution. The final 20 mL mixture was vigorously shaken and sonicated for 0.5 h. After 15 minutes, the $LiMnPO_4$ NCs were transferred into the aqueous phase. The aqueous phase was then collected and centrifuged at 9000 rpm. The precipitate was vigorously shaken in a mixture of ultrapure water (30 mL) and chloroform (20 mL), to remove the excess of $LiPF_6$ and organics from the NCs. After centrifugation at 9000 rpm, the liquid phase was discarded and the precipitate was then redispersed in 20 mL of ultrapure water and 10 mL of ethanol and it was finally centrifuged at 8000 rpm. This last step was repeated twice.

3.2.3 Carbon coating of the LMP NCs

A coating layer of carbon was produced on both etched and not etched LMP NCs, following the procedure described below. For the etchLMP sample, about 500 mg of NCs were dispersed in aqueous glucose solution (150 mg of glucose in 5 mL of water) while for neLMP the NCs were solubilized in 5 mL of glucose dispersion in chloroform. The solutions were sonicated for 0.5h and then dried overnight under vacuum at 40 °C. The pyrolytic procedure that produced the carbonaceous coating was the same for both samples. A quartz combustion boat containing the dried mixture (NCs + glucose) was placed in the middle of a tubular furnace under a slightly reducing atmosphere (95% Ar, 5% H_2, 50 sccm) and was heated up to 450 °C (5 °C/min), kept at 450°C for 1h and then slowly heated to 650 °C (3 °C/min) and kept at 650°C for 1h. The furnace was then cooled down to room temperature, while still under Ar/H_2 (95/5%) atmosphere.

The synthetic procedure of etched (etchLMP/C), not etched (neLMP/C) and carbon coated $LiMnPO_4$ NCs-based cathodes are shown in **Scheme 3.1**.

3.2.4 Electrochemical Measurements

The electrochemical characterization of the etched and not etched NCs, in both cases after carbon coating, was carried out on composite electrodes with the preparation procedure as introduced in Chapter 2. Cyclic Voltammetries (CVs) at 30 μV s^{-1} and Electrochemical impedance Spectroscopy (EIS). The cells were charged using a constant current–constant voltage (CC–CV) protocol, at different currents (i.e. different C-rates: C/10, 1C, 2C, 5C and 10C considering 1C = 170 mA g^{-1}_{LMP}) up to 4.5V followed by constant voltage step at 4.5V for 1h. The cells were then discharged down to 2.5V at the same C-rate used for the corresponding charge step. EIS runs were performed on fully charged (4.5V) and fully discharged (2.5V) cells, in the range 100 kHz-10 mHz with a perturbation amplitude of 5 mV and 10 points/decade. Our composite electrodes had a higher fraction of active material (80%) with respect to previous reports (75% at best), which contributes to reducing the need of carbon additive and polymeric binder, with a consequent benefit for the future development of high energy density LMP-based cathodes.

3.3 Results and Discussions

Material characterization

The $LiMnPO_4$ NCs were prepared *via* a colloidal method, by modification of the synthesis that we had previously developed for iron-based phospho-olivine.[28] The synthesis required the use of organic ligands such as oleylamine and octadecene to stabilize the NCs growth and to control their size. At the same time, the presence of these long chain ligands makes the NCs hydrophobic and soluble only in nonpolar or moderately polar solvents (for example chloroform). The hydrophobicity of the NCs represents a serious drawback during the carbon coating procedure, which involves the use of an aqueous glucose solution as carbon source:[10] As the NC solution and the glucose solution would not mix, we were forced to use a glucose dispersion in chloroform. The insolubility of glucose in a nonpolar solvent reduces the possibility of formation of a uniform carbon coating around each individual NC as a consequence of the sugar decomposition during the annealing step. In order to make the NCs hydrophilic and therefore allow an adequate mixing with the aqueous glucose solution, the aliphatic surfactants were removed by treating the NCs with an aqueous $LiPF_6$ solution, following the same etching procedure developed in our previous paper.[29] The activity of $LiPF_6$ as etching agent is due to its reaction with water, which produces *in situ* hydrofluoric acid, according to the following mechanism:[29, 30]

$$LiPF_6 + H_2O \rightarrow LiF + POF_3 + 2HF$$

The generated HF can act as an etchant on the surface of the LMP nanoparticles, by removing the hydrophobic surfactant molecules and replacing them with hydrophilic PF_6^- anions. The choice of $LiPF_6$ was additionally driven by the fact that anhydrous organic solutions of this salt are commonly used as electrolytes for lithium-ion batteries. If, from one side, the hydrophilicity of NCs can be crucial to allow a good contact between particles and carbon, on the other it is also important to maintain the nanometer size dimensions of the particles during the heating treatment that is followed to generate the conductive carbon layer (and that is carried out at a temperature of 650 °C). Such harsh conditions can potentially cause partial coalescence of the NC into bigger particles. In our case, this was prevented by adopting a double step pyrolytic process (see the experimental section for details) and by maintaining the samples at the final temperature of 650 °C for only 1h.

We performed carbon coating on both etched (etchLMP) and not etched (neLMP) $LiMnPO_4$ NCs, to study the effect of the surface treatment step on the electrochemical performances of the LMP-based cathodes. In the case of etchLMP, the only carbon source came from the added glucose, while for neLMP the carbon sources were represented by both glucose and the organic ligands coming from the synthesis. The X-ray diffraction (XRD) spectra of the neLMP, etchLMP, neLMP/C and etchLMP/C dry powders are reported in **Figure 3.1**a. All samples were characterized by similar

diffraction patterns, corresponding to pure $LiMnPO_4$ with orthorhombic olivine-type structure (*Pnma* space group; ICSD collection code: 167253). From the XRD spectra we can conclude that

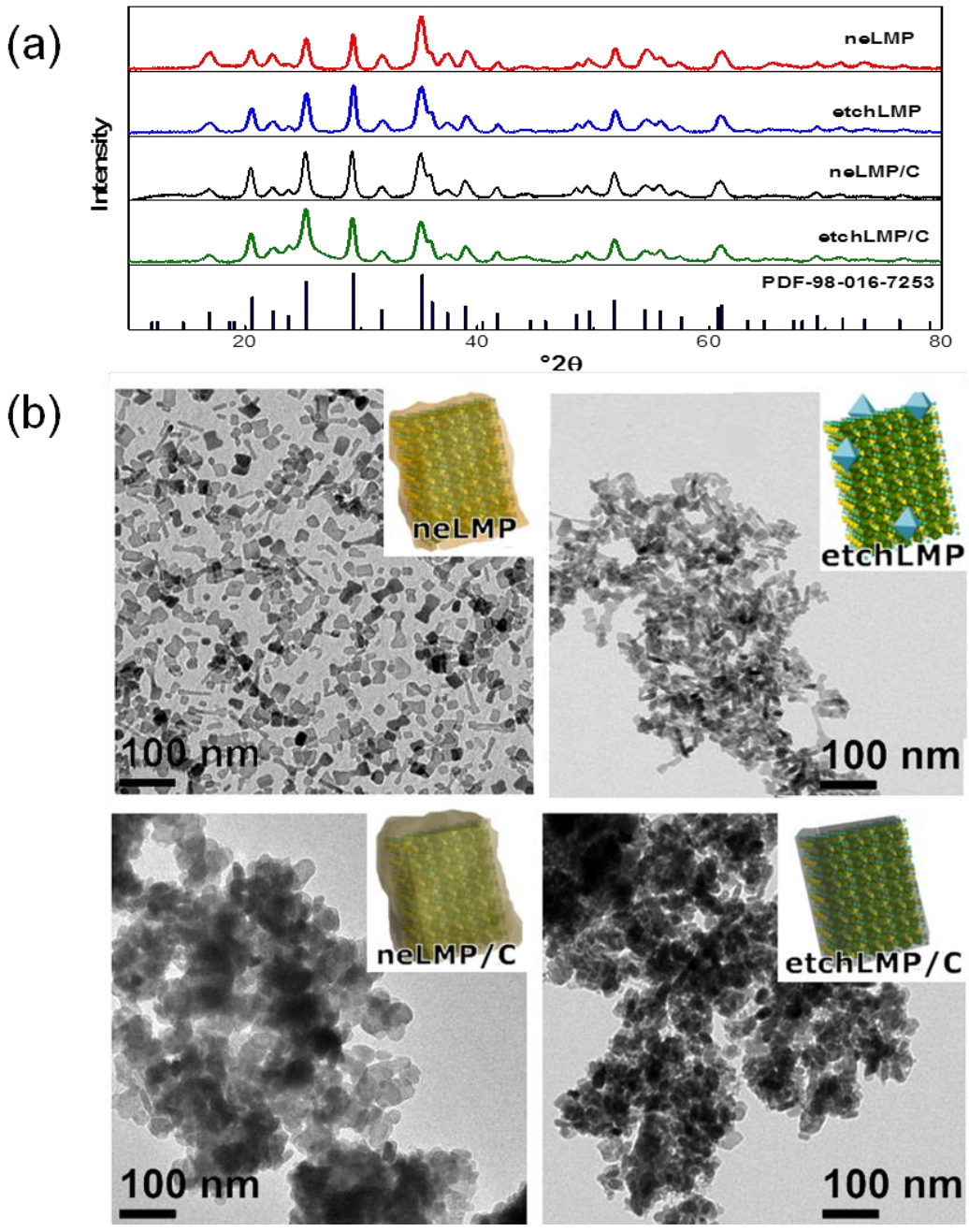

Figure 3.1. Structural and morphological characterization of the not etched and etched $LiMnPO_4$ NCs before (neLMP, etchLMP) and after (neLMP/C, etchLMP/C) carbon coating. (a) XRD patterns corresponding to pure $LiMnPO_4$ with orthorhombic olivine-type structure (ICSD collection code: 167253); (b) low-magnification TEM images, in which several $LiMnPO_4$ nanoparticles can be seen.

neither structural changes in the crystals nor impurities were generated during both etching and carbon coating. TEM images of the initial neLMP, as well as the etchLMP, neLMP/C and etchLMP/C samples are reported in Figure 1b. The initial neLMP NCs exhibited dumbbell and platelet-like shapes, with sizes ranging from few nm to 50 nm. On average, the lateral size of the NC decreased of about 5-10% after the $LiPF_6$ treatment, which is beneficial as it helps to reduce the Li^+ diffusion length. This difference in size between the not etched and the etched NCs were retained after the respective samples were carbon coated, even though the carbon coating caused some reshaping and agglomeration of the NCs. The extent of agglomeration was actually minimized by the pyrolytic protocol adopted here. For comparison, the TEM image of **Figure 3.2**a, which is referred to etchLMP/C prepared by a simplest single step pyrolytic process at 650 °C (onestep-etchLMP/C), indicates that these particles are clearly bigger than the initial particles, with size exceeding 100 nm.

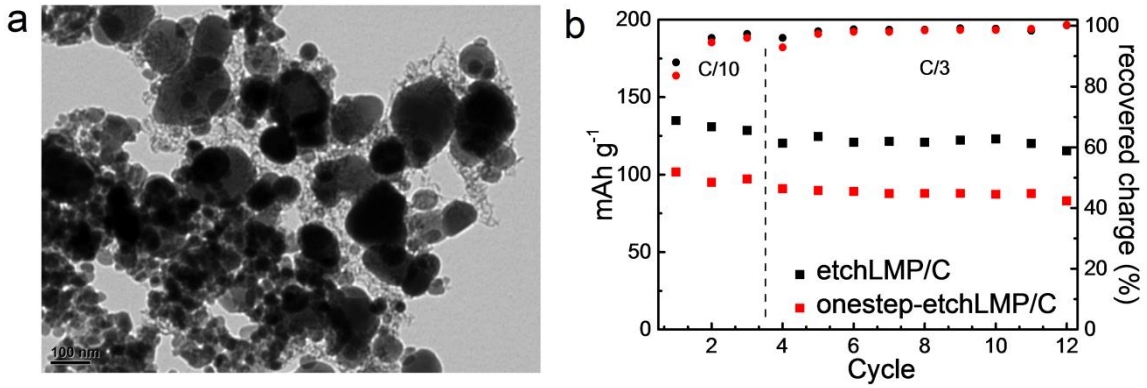

Figure 3.2. Morphological and electrochemical characterization of one-step-etchLMP/C- based electrode. a) TEM image, which evidences the presence of crystals with sizes bigger than 100 nm; b) comparison of specific capacity (mAh g^{-1}) and recovered charge (%) vs. cycle number for one-step-etchLMP/C and etchLMP/C–based electrodes at C-rates of C/10 and C/3.

The carbon coated neLMP/C and etchLMP/C NCs were analyzed by HRTEM (**Figure 3.3**a). Both samples were characterized by an amorphous carbon layer surrounding the crystals, with the preservation of the platelet morphology. The etched NCs appeared to have a thinner carbon layer than the not etched ones, for which the coating was almost 2.0 nm thick, as evidenced from the fringes at the edges of the particles. To assess the weight fraction in the NCs due to the carbon

coating, the neLMP/C and etchLMP/C samples were subjected to TGA analysis under air.[24, 31] The data are reported in Figure 3.3b as percentage of weight loss *vs.* temperature. The two samples exhibited a weight loss in the 300-600 °C range: here, the loss of weight coincides with the carbon coating that was converted in CO_2, while the residual weight corresponds to $LiMnPO_4$, which is stable even at temperatures above 700 °C. The carbon content was found to be 12.4 % wt. for neLMP/C and 9.7 % wt. for etchLMP/C. Also, while the TGA curve of the etchLMP/C sample exhibited one step, with a decomposition temperature of 420 °C, the curve of the neLMP/C sample exhibited two steps, with decomposition temperatures of 420 °C and 570°C. Since in the etched sample the only carbon source comes from glucose, we assign the lower temperature step in the two samples to the decomposition of the carbon originating from glucose, while the higher temperature step that was seen only in the neLMP/C sample should have arisen from the pyrolysis of carbon originating from the surfactant shell (made of oleylamine and octadecene).

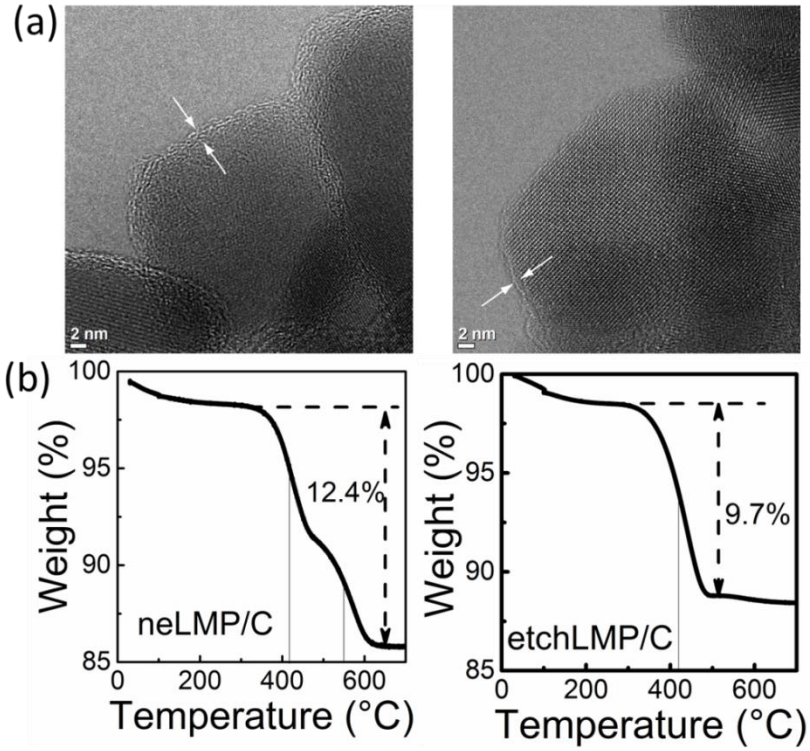

Figure 3.3. Characterization of carbon coating on neLMP/C and etchLMP/C NCs. (a) HRTEM images: the arrows and the different colors evidenced the amorfous carbon layer on neLMP/C NCs and etchLMP/C NCs; (b) TGA analysies of dried powders: the vertical solid lines identify the decomposition temperatures of the carbonaceous layers.

Electrochemical performance

As preliminary electrochemical test, we investigated the behavior of the etchLMP/C and neLMP/C NCs by CVs. **Figure 3.4**a compares the CVs (normalized to the mass of active material) of the two systems. Both samples were characterized by an anodic peak A at 4.23 V which is related to Mn^{2+}/Mn^{3+} oxidation, and a cathodic peak C at 3.93 V attributed to the reverse redox process. The main difference between the two systems is that the value of the normalized current of the peaks for the etched sample (blue line) was almost 8 times higher than that of the neLMP/C (red line). This behavior can indicate a superior conductivity of the former electrode.

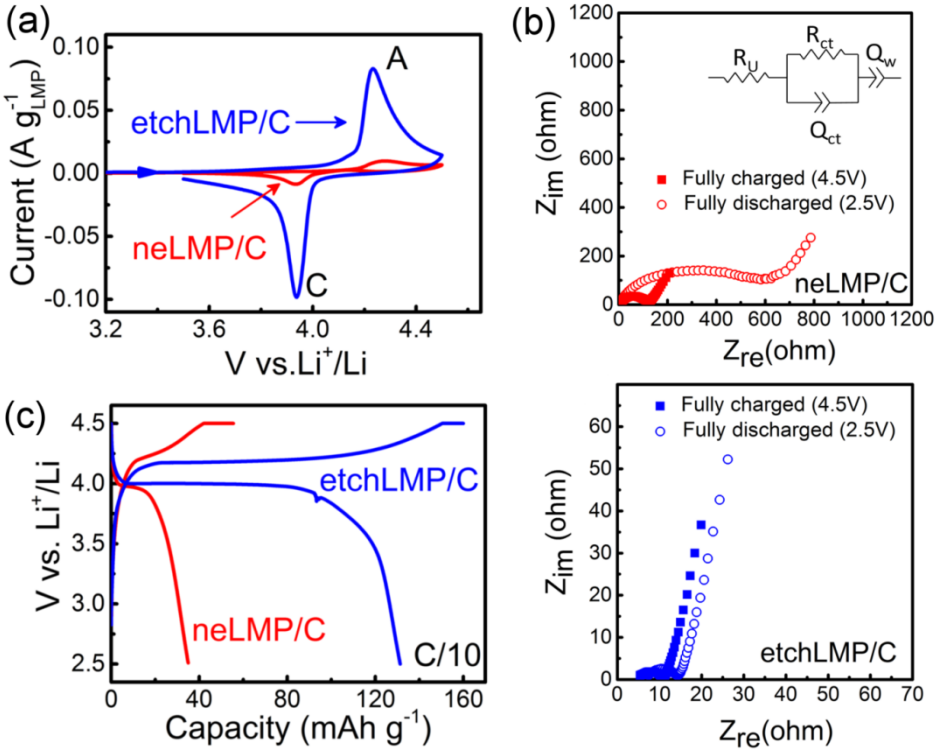

Figure 3.4. Electrochemical characterization of neLMP/C and etchLMP/C-based cells. (a) Cyclic voltammetry performed at scan rate of 30 μV s^{-1} in the 3.5 - 4.5 voltage range with current normalized to the active material mass; (b) electrochemical impedance spectra (Nyquist plot) of the fully charged (4.5 V, full squares) and discharged (2.5 V, empty dots) cells, inset: scheme of the equivalent circuit that better fits the impedance data of the fully charged cells; (c) voltage profiles upon the first galvanostatic charge/discharge cycle at C-rate of C/10.

To support our assumption we performed EIS of fully charged (4.5V) and fully discharged (2.5V) cells. Figure 3.4b reports the recorded impedance. As expected for a lithium ion battery, the impedance was found to be sensitive to the state of charge of the battery; in particular, it increases in the discharged state because at 2.5 V no redox process takes place, with the consequent enhancement of charge transfer resistance.[32] The equivalent circuit that better fits the EIS data of the fully charged cells (see Figure 3.4b inset) is composed by an uncompensated resistance (R_U) in series with one parallel R_{ct}/Q_{ct} and Q_W elements, with R_{ct} and Q_{ct} corresponding to charge transfer resistance and constant phase element respectively, Q_W corresponding to a constant phase element related to Li^+ diffusion. From the fitting of the experimental data, the extrapolated R_{ct} for the neLMP/C is ~ 212 ohm cm^2 while R_{ct} for the etchLMP/C is almost 18 times lower (i.e. 12 ohm cm^2). The lower R_{ct} value for the etched sample is in good agreement with the CVs data and is a clear evidence of the higher conductivity achieved by etching the NCs prior to carbon coating. Therefore etching does improve the quality of the carbon coating that is grown on the particles. From the data in the lower frequency range (the so-called Warburg region) using Eq.1 and Eq.2, it is possible to estimate the ratio between the Li^+ diffusion coefficients (D_{Li+}) for the etched and not etched samples:[33, 34]

$$\frac{D_{Li_{etchLMP/C}}}{D_{Li_{neLMP/C}}} = \left(\frac{\sigma_{neLMP/C}}{\sigma_{etchLMP/C}}\right)^2 \quad (1)$$

$$D_{Li} = \frac{R^2T^2}{n^4F^4A^22C^2\sigma^2} \quad (2)$$

where *R* is the gas constant, *T* is the absolute temperature, *n* is the number of electrons transferred in the redox process, *F* is the Faraday constant, *A* is the surface area of the LMP-based electrode, *C* is the Li^+ concentration in the solid electrode and σ is the Warburg factor.

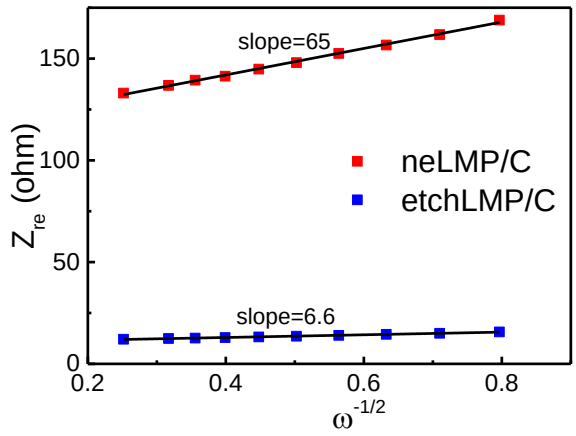

Figure 3.5. Real components of the impedance (Z_{re}) vs. the reciprocal of the square root of the angular frequency ($\omega^{-1/2}$) for neLMP/C (red) and etchLMP/C (blue) –based electrodes. The slope of the curve represents the Warburg factors, σ.

The Warburg factors σ were determined from the plot (**Figure 3.5**) of the real components of the impedance (Z_{Re}) versus the reciprocal of the square root of the angular frequency ($\omega^{-1/2}$), according to the following expression:[33, 34]

$$Z_{Re} = R_{ct} + R_s + \sigma\ \omega^{-1/2} \qquad (3)$$

The estimated D_{Li} ratio reveals that the Li^+ diffusion is almost two orders of magnitude faster in the case of etchLMP/C compared to the neLMP/C. This remarkable result further confirms the critical role of NC surface etching: this step not only improves the electron conductivity, but it positively affects the Li^+ diffusion rate.

The electrochemical behavior of the etched and not etched LMP/C-based cells was finally studied by galvanostatic charge/discharge cycles. Figure 3.4c compares the first voltage profiles upon galvanostatic charge/discharge at the low C-rate of C/10 of the two studied LMP samples. The etchLMP/C-based electrode delivered a specific capacity close to 130 mAh g^{-1} while the not etched sample exhibited a poor capacity of only 35 mAh g^{-1}. Already since these first charge/discharge cycles, the superior performance of the etchLMP/C sample was clearly visible. In view of actual exploitation in a real battery type of scenario, we studied the etchLMP/C-based cathodes at different charge and discharge C-rates, ranging from 1C to 10C, with particular attention to the charge process. The adopted charge protocol (see the experimental section for details) enabled a reasonable fast charge time of maximum 2h at 1C-rate, and even faster at higher C-rates. **Figure 3.6** reports the specific capacity and the recovered charge *vs.* cycle number (a) and the corresponding voltage

profiles for the first charge/discharge cycle (b) at each tested C-rates for etchLMP/C sample. For comparison, Figure 3.6a reports in addition the specific capacity of the neLMP/C-based cell, while the voltage profiles for the first charge/discharge cycle are reported in Figure 3.6c.

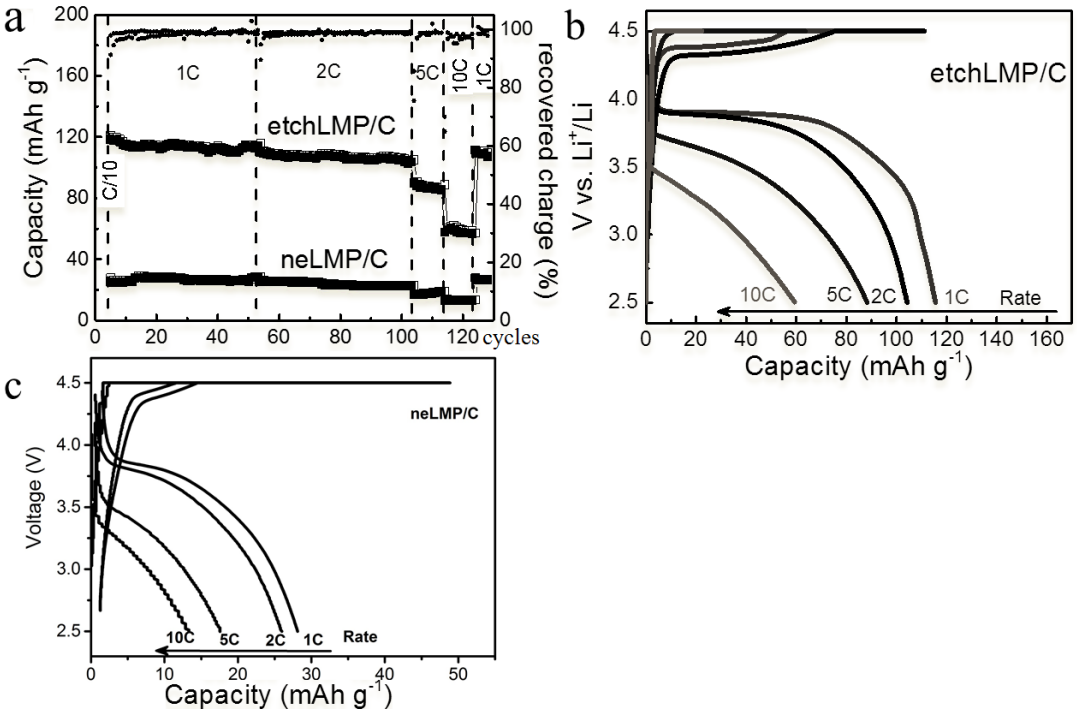

Figure 3.6. Galvanostatic charge/discharge performances at discharge rates of 1C, 2C, 5C and 10C. The electrodes were charged following a constant current - constant voltage protocol. a) Comparison of specific capacity (mAh g^{-1}) and recovered charge (%) vs. cycle number for etchLMP/C and neLMP/C–based electrodes; b) voltage profiles upon the first galvanostatic charge/discharge cycle for etchLMP/C-based electrode; c). Voltage profiles upon the first galvanostatic charge/discharge cycle for neLMP/C-based electrode at 1C, 2C, 5C and 10C.

The etchLMP/C electrode exhibited a specific capacity of 118 mAh g^{-1} at 1C with a stable cycling performance, with a capacity fade of 0.06% per cycle during the first 50 cycles as shown in Figure 3.6. At 2C, 5C and 10C the capacities were 110 mAh g^{-1}, 90 mAh g^{-1} and 60 mAh g^{-1} respectively. The etchLMP/C delivered capacity was higher than that of the neLMP/C NCs, which never exceeded 30 mA g^{-1} at all tested C-rates. At the end of the whole charge/discharge protocol (120 cycles at different C-rates), the etchLMP/C electrode delivered, at 1C, a capacity of 109 mAh g^{-1}. This value corresponds to 92% of the initial capacity.

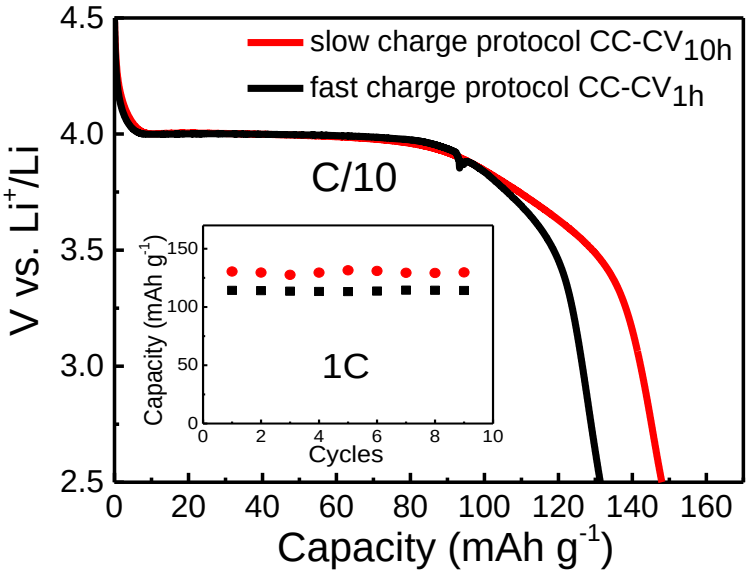

Figure 3.7. Voltage profiles upon the first galvanostatic discharge cycle at C/10 and specific capacity vs. cycle number at 1C for etchLMP/C. Comparison between slow (red) and fast (black) charge protocols.

When a slower constant current-constant voltage (CC-CV) charge protocol (charging constant voltage times of 10h) was adopted, the etchLMP/C-based cathode showed a specific capacity increase of about 14% at both C/10 an 1C (**Figure 3.7**) with respect to the data reported in Figure 3.6. However, even if slow charge protocols are a common practice in the literature[21-24] and allow higher discharge capacity values, the cell performances are far from what is required for a practical use of a battery that usually needs fast charge processes. The good rate capability of etchLMP/C NCs, compared to the not etched sample can be primarily related to a better and more effective carbon coating on the NCs surface. The rate capability here reported for the etchLMP/C NCs represents an important result, taking into account the electrode formulation (80 % wt. active material) and the adopted charge protocol.

3.4 Conclusions

In summary, we have prepared $LiMnPO_4$ nanocrystals through colloidal synthesis, followed by surface etching with $LiPF_6$ and carbon coating with glucose. We demonstrate the crucial and beneficial effect of the etching procedure on the electrochemical performances of so-prepared etchLMP/C-based cathodes for LIBs. The aforementioned electrodes showed good and stable

electrochemical performances, displaying discharge capacities at 1C of 118 mAh g^{-1}, 4 times higher than those of electrodes based on not etched LMP/C. The favorable influences of the adopted etching process are: i) the efficient removal of the hydrophobic passivated surfactants shell, present on NCs surface after the colloidal synthesis. This increases the nanoparticles solubility in the aqueous glucose solution used as carbon source for NCs coating, enabling the formation of a good conductive carbon layer; (ii) the possibility to prepare composite electrodes with a reduced amount of carbon additive and polymeric binder, with a consequent benefit on the energy density of LMP-based cathodes. The protocol reported here enabled the preparation of LMP/NCs-based cathodes with high rate capability and which can be charged with a reasonable fast CC-CV procedure (of maximum 2h at 1C-rate), which is of paramount importance for the future development of high rate and high power Li-ion batteries.

3.5 References

(1) Padhi, A. K.; Nanjundaswamy, K. S.Goodenough, J. B. Phospho-olivines as positive-electrode materials for rechargeable lithium batteries. *J. Electrochem Soc.* **1997,** *144,* 1188-1194.

(2) Alyoshin, V. A.; Pleshakov, E. A.; Ehrenberg, H.Mikhailova, D. Platelike $LiMPO_4$ (M = Fe, Mn, Co, Ni) for Possible Application in Rechargeable Li Ion Batteries: Beyond Nanosize. *J. Phys. Chem. C* **2014,** *118,* 17426-17435.

(3) Delacourt, C.; Laffont, L.; Bouchet, R.; Wurm, C.; Leriche, J. B.; Morcrette, M.; Tarascon, J. M.Masquelier, C. Toward understanding of electrical limitations (electronic, ionic) in $LiMPO_4$ (M = Fe, Mn) electrode materials. *J. Electrochem. Soc.* **2005,** *152,* A913-A921.

(4) Wang, D. Y.; Buqa, H.; Crouzet, M.; Deghenghi, G.; Drezen, T.; Exnar, I.; Kwon, N. H.; Miners, J. H.; Poletto, L.Graetzel, M. High-performance, nano-structured $LiMnPO_4$ synthesized via a polyol method. *J. Power Sources* **2009,** *189,* 624-628.

(5) Yonemura, M.; Yamada, A.; Takei, Y.; Sonoyama, N.Kanno, R. Comparative kinetic study of olivine Li_xMPO_4 (M = Fe, Mn). *J. Electrochem. Soc.* **2004,** *151,* A1352-A1356.

(6) Dong, Y. Z.; Wang, L.; Zhang, S. L.; Zhao, Y. M.; Zhou, J. P.; Xie, H.Goodenough, J. B. Two-phase interface in $LiMnPO_4$ nanoplates. *J. Power Sources* **2012,** *215,* 116-121.

(7) Piper, L. F. J.; Quackenbush, N. F.; Sallis, S.; Scanlon, D. O.; Watson, G. W.; Nam, K. W.; Yang, X. Q.; Smith, K. E.; Omenya, F.; Chernova, N. A.Whittingham, M. S. Elucidating the Nature of Pseudo Jahn-Teller Distortions in Li_xMnPO_4: Combining Density Functional Theory with Soft and Hard X-ray Spectroscopy. *J. Phys. Chem. C* **2013,** *117,* 10383-10396.

(8) Bakenov, Z.Taniguchi, I. Physical and electrochemical properties of $LiMnPO_4$/C composite cathode prepared with different conductive carbons. *J. Power Sources* **2010,** *195,* 7445-7451.

(9) Oh, S. M.; Oh, S. W.; Myung, S. T.; Lee, S. M.Sun, Y. K. The effects of calcination temperature on the electrochemical performance of $LiMnPO_4$ prepared by ultrasonic spray pyrolysis. *J. Alloy Compd.* **2010,** *506,* 372-376.

(10) Wang, J. J.Sun, X. L. Understanding and recent development of carbon coating on $LiFePO_4$ cathode materials for lithium-ion batteries. *Energ. Environ. Sci.* **2012,** *5,* 5163-5185.

(11) Bakenov, Z.Taniguchi, I. Electrochemical performance of nanocomposite LiMnPO4/C cathode materials for lithium batteries. *Electrochem. Commun.* **2010,** *12,* 75-78.

(12) Xiao, J.; Xu, W.; Choi, D. W.Zhang, J. G. Synthesis and Characterization of Lithium Manganese Phosphate by a Precipitation Method. *J. Electrochem. Soc.* **2010,** *157,* A142-A147.

(13) Rui, X. H.; Zhao, X. X.; Lu, Z. Y.; Tan, H. T.; Sim, D. H.; Hng, H. H.; Yazami, R.; Lim, T. M.Yan, Q. Y. Olivine-Type Nanosheets for Lithium Ion Battery Cathodes. *Acs Nano* **2013,** *7,* 5637-5646.

(14) Zhang, W. X.; Shan, Z. Q.; Zhu, K. L.; Liu, S. Z.; Liu, X. Y.Tian, J. H. LiMnPO4 nanoplates grown via a facile surfactant-mediated solvothermal reaction for high-performance Li-ion batteries. *Electrochim. Acta* **2015,** *153,* 385-392.

(15) Guo, H.; Wu, C. Y.; Xie, J.; Zhang, S. C.; Cao, G. S.Zhao, X. B. Controllable synthesis of high-performance LiMnPO4 nanocrystals by a facile one-spot solvothermal process. *J. Mater. Chem. A* **2014,** *2,* 10581-10588.

(16) Gutierrez, A.; Qiao, R. M.; Wang, L. P.; Yang, W. L.; Wang, F.Manthiram, A. High-Capacity, Aliovalently Doped Olivine $LiMn_{(1-3x/2)}V_x$ square $_{x/2}PO_4$ Cathodes without Carbon Coating. *Chem. Mater.* **2014,** *26,* 3018-3026.

(17) Zhang, K.; Han, X. P.; Hu, Z.; Zhang, X. L.; Tao, Z. L.Chen, J. Nanostructured Mn-based oxides for electrochemical energy storage and conversion. *Chem. Soc. Rev.* **2015,** *44,* 699-728.

(18) Kou, L. Q.; Chen, F. J.; Tao, F.; Dong, Y.Chen, L. High rate capability and cycle performance of Ce-doped $LiMnPO_4$/C via an efficient solvothermal synthesis in water/diethylene glycol system. *Electrochim. Acta* **2015,** *173,* 721-727.

(19) Iturrondobeitia, A.; Goni, A.; de Muro, I. G.; Lezama, L.; Kim, C.; Doeff, M.; Cabana, J.Rojo, T. High-Voltage Cathode Materials for Lithium-Ion Batteries: Freeze-Dried $LiMn_{0.8}Fe_{0.1}M_{0.1}PO_4$/C (M = Fe, Co, Ni, Cu) Nanocomposites. *Inorg. Chem.* **2015,** *54,* 2671-2678.

(20) Omenya, F.; Miller, J. K.; Fang, J.; Wen, B. H.; Zhang, R. B.; Wang, Q.; Chernova, N. A.Whittingham, M. S. Single-Phase Lithiation and Delithiation of Simferite Compounds $Li(Mg,Mn,Fe)PO_4$. *Chem. Mater.* **2014,** *26,* 6206-6212.

(21) Cheng, G. Y.; Zuo, P. J.; Wang, L. G.; Shi, W.; Ma, Y. L.; Du, C. Y.; Cheng, X. Q.; Gao, Y. Z.Yin, G. P. High-performance carbon-coated $LiMnPO_4$ nanocomposites by facile two-step solid-state synthesis for lithium-ion battery. *J. Solid State Electr.* **2015,** *19,* 281-288.

(22) Xia, Q. B.; Liu, T.; Xu, J. J.; Cheng, X. Y.; Lu, W.Wu, X. D. High performance porous $LiMnPO_4$ nanoflakes: synthesis from a novel nanosheet precursor. *J. Mater. Chem. A* **2015,** *3,* 6301-6305.

(23) Zhao, M.; Fu, Y.; Xu, N.; Li, G. R.; Wu, M. T.Gao, X. P. High performance $LiMnPO_4$/C prepared by a crystallite size control method. *J. Mater. Chem. A* **2014,** *2,* 15070-15077.

(24) Zhang, L. F.; Qu, Q. T.; Zhang, L.; Li, J.Zheng, H. H. Confined synthesis of hierarchical structured $LiMnPO_4$/C granules by a facile surfactant-assisted solid-state method for high-performance lithium-ion batteries. *J. Mater. Chem. A* **2014,** *2,* 711-719.

(25) Su, J.; Liu, Z. Z.; Long, Y. F.; Yao, H.; Lv, X. Y.Wen, Y. X. Enhanced electrochemical performance of $LiMnPO_4$/C prepared by microwave-assisted solvothermal method. *Electrochim. Acta* **2015,** *173,* 559-565.

(26) Varzi, A.; Taubert, C.; Wohlfahrt-Mehrens, M.; Kreis, M.Schutz, W. Study of multi-walled carbon nanotubes for lithium-ion battery electrodes. *J. Power Sources* **2011,** *196,* 3303-3309.

(27) Marks, T.; Trussler, S.; Smith, A. J.; Xiong, D. J.Dahn, J. R. A Guide to Li-Ion Coin-Cell Electrode Making for Academic Researchers. *J. Electrochem. Soc.* **2011,** *158,* A51-A57.

(28) Paolella, A.; Bertoni, G.; Dilena, E.; Marras, S.; Ansaldo, A.; Manna, L.George, C. Redox Centers Evolution in Phospho-Olivine Type ($LiFe_{0.5}Mn_{0.5}PO_4$) Nanoplatelets with Uniform Cation Distribution. *Nano Lett.* **2014,** *14,* 1477-1483.

(29) Paolella, A.; Bertoni, G.; Marras, S.; Dilena, E.; Colombo, M.; Prato, M.; Riedinger, A.; Povia, M.; Ansaldo, A.; Zaghib, K.; Manna, L.George, C. Etched Colloidal $LiFePO_4$ Nanoplatelets toward High-Rate Capable Li-Ion Battery Electrodes. *Nano Lett.* **2014,** *14,* 6828-6835.

(30) Barlow, C. G. Reaction of water with hexafluorophosphates and with Li bis(perfluoroethylsulfonyl)imide salt. *Electrochem. Solid St.* **1999,** *2,* 362-364.

(31) Damen, L.; De Giorgio, F.; Monaco, S.; Veronesi, F.Mastragostino, M. Synthesis and characterization of carbon-coated $LiMnPO_4$ and $LiMn_{1-x}Fe_xPO_4$ (x=0.2, 0.3) materials for lithium-ion batteries. *J. Power Sources* **2012,** *218,* 250-253.

(32) Rodrigues, S.; Munichandraiah, N.Shukla, A. K. A review of state-of-charge indication of batteries by means of a.c. impedance measurements. *J. Power Sources* **2000,** *87,* 12-20.

(33) Zhang, Z. H.; Zhou, Z. F.; Nie, S.; Wang, H. H.; Peng, H. R.; Li, G. C.Chen, K. Z. Flower-like hydrogenated TiO_2(B) nanostructures as anode materials for high-performance lithium ion batteries. *J. Power Sources* **2014,** *267,* 388-393.

(34) Bard, A. J.Faulkner, L. R., *Electrochemical methods : fundamentals and applications*. 2nd ed.; Wiley: New York, 2001.

CHAPTER IV

Colloidally Assisted Synthesis to Phase Pure $Na_{1.7}Ni_{1.0}Mn_{2.9}O_{7.6}$ with Suppressed P2/O2 Phase Transition as High Stable Cathode for Na-ion Batteries

4.1. Introduction

The two main reasons for switching from lithium to sodium are that sodium is highly abundant and its chemistry is closely related to that of lithium. As introduced in Chapter I, sodium-ion batteries (NIBs) use the same types of cathode materials developed for LIBs (i.e., polyanionic networks and layered oxide-based compounds). However, Na^+ ion is bigger than Li^+ (1.02 Å and 0.76 Å respectively) so that its intercalation in the electrode host structure is more difficult[1] and as result the specific energy of NIBs is commonly lower than that of LIBs. The search for electrode materials with superior performances in terms of high working voltage, cycling stability and good rate capability is therefore mandatory in order to make NIBs competitive to the much more mature LIBs.

Cathode materials characterized by high working potentials (hence high energies) are represented by layered oxides with the general structure Na_xTMO_2, where TM stands for one or more transition metals [2] such as Cr,[3] Mn,[4] Fe,[5] Co[6] or Ni.[7] These materials are characterized by a layered structure (see Chapter 1), with the Na ions sandwiched between the TMO_6 layers. According to current literature reports, if the oxide contains only one transition metal species, the cathode exhibits limited capacity, poor rate capability and low cycling performance,[3-8] whereas higher performances are found when more than one metal species is present in the oxide layers (albeit at the cost of losing some specific capacity) because of the cooperative effect of binary or ternary metals in metal oxide layers.[2] Most of the effort is devoted to removing multiple plateaus, to increasing the average voltage and to improving the reversible capacity. An example is represented by Ni-Mn binary layered oxides, which are regarded as promising cathode materials since their Ni^{2+}/Ni^{4+} redox

processes are highly reversible and take place at a high nominal operating voltage (up to 4.2 V vs. Na^+/Na). Depending on the Na^+ intercalation sites and on the number of unique TMO_6 layers in the repeating cell unit, Na layered oxides can be classified as of O2-, O3-, P2- and P3-type (see Chapter 1).[9] In the O-type oxides, Na ions are located in octahedral sites, while in the P-type oxides they are hosted in prismatic sites and the number indicates the number of unique interlayers that are surrounded by the different oxide layers. The Na interlayers that are sandwiched by the oxide layers can vary from 2 to 3 per cell unit.

A major problem with these materials is their poor structural stability upon Na^+ intercalation/deintercalation at the high operating voltages of such cathodes. O3-$NaNi_{0.5}Mn_{0.5}O_2$ for example is known to undergo several phase transitions (from O3 to a final P3 phase)[10] during the charge process, which implies multiple slab gliding and a strong Jahn–Teller distortion that negatively affect its cycling stability. Better electrochemical performances are achieved with the P2-type oxides, due to their lower Na^+ diffusion barrier (i.e. high ionic conductivity)[2, 11-13] and their higher structural stability. However, the cycling performance of P2-$Na_{2/3}[Ni_xMn_y]O_2$-based cathodes is generally greatly affected by the working voltage window.[14, 15] When they are deeply charged (this typically occurs at potentials of ~4.4 V vs Na^+/Na), the low amount of sodium in their structure usually induces a gliding of the TMO_6 layers, with the transition to the O2-phase [8, 16] (see **Figure 4.1**). As this phase transition is irreversible and results in a drastic capacity fading, the cathode cannot be cycled at potentials higher than 4 V vs. Na^+/Na,[17, 18] which narrows the voltage window and limits the energy delivered and the capacity of the electrode, hence the practical use of these materials.

Partial cation substitution has been extensively proposed as an effective strategy to improve the cycling performance of the P2-type systems. Several types of cations have been tested for such scope, such as the electrochemically inactive Li, Ti, Mg and Zn[15, 16, 19-21] ones, or Cu and Fe[8, 22] that are instead electroactive during the charge/discharge process. The new cations can alleviate the variation of lattice parameters occurring during the P2/O2 phase transition or make the transition occur at a higher voltage. Very recently, Manikandan et al. [23] have shown that P2-$Na_{0.5}Ni_{0.25}Mn_{0.75}O_2$ (Ni:Mn ratio 1:3) exhibits a relatively stable cycling performances when charged at C/10 up to 4.4 V vs. Na^+/Na. The reasons for such stability were however not provided, and the good electrochemical behavior was inferred to be related to a more reversible P2/O2 transition.

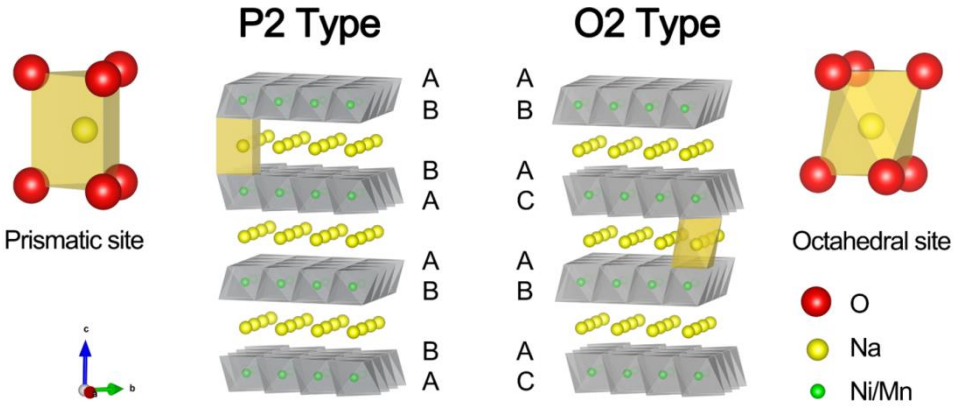

Figure 4.1. Structure of P2 and O2 phase $NaTMO_6$ layered oxides. Sodium ions are located at the prismatic and octahedral site in P2 and O2 type, respectively.

In this Chapter, the P2/O2 transition is actually eliminated by 'phase-transition mitigation' in a phase pure P2-$Na_z[Ni_xMn_y]O_2$-based cathode at a specific Na:Ni:Mn ratio of cations (1.7:1:3). We prepared our sample using a colloidally-assisted, two-step synthesis. In the initial colloidal step, size and stoichiometric controlled $Ni_{0.25}Mn_{0.75}O$ nanocrystals (NCs) were synthesized, which were then used as precursors to prepare P2-$Na_{1.7}Ni_{1.0}Mn_{2.9}O_{7.6}$ (NaNMO) in a second sodiation step carried out via a conventional solid state synthesis. The cathode material could withstand long charge/discharge cycles up to 4.4 V vs Na^+/Na. due to the suppression of the detrimental P2/O2 phase transition during Na^+ intercalation/deintercalation. To compare the different techniques, the sample is also prepared by all solid-state reaction.

4.2. Experimental Section

4.2.1 Colloidal synthesis of $Ni_{0.25}Mn_{0.75}O$

Colloidal $Ni_{0.25}Mn_{0.75}O$ nanocrystals (NCs) were prepared dissolving 4.32g of Manganese(II) Acetylacetonate (MnAcAc anhydrous) and 1.62 g of Nickel (II) Acytelacetonate (NiAcAc anhydrous) in a mixture containing 100mL of oleylamine and 100mL of 1-octadecene,in a 500 mL three-neck flask connected to a standard Schlenk line. The solution was heated at 230 °C (heating rate 5°C/min) under N_2 for 4 hours. It was then precipitated (separate the obtained nanoparticles

from the solution) and cleaned by repeated additions of chloroform and ethanol followed by centrifugation at 9000 rpm. The precipitate was dried at 40 °C in the vacuum oven. Around 1.6 g of powders were obtained and the sample was named as NMO for short.

4.2.2 Solid-state synthesis of $Na_{1.7}Ni_{1.0}Mn_{2.9}O_{7.6}$

The as-synthesized NMO NCs (1g) and 0.47g of sodium carbonate (Na_2CO_3) were mixed in 10 mL of ethanol and ball-milled at 500 rpm for 3 hours, by using a 12 mL stainless steel jar (Retsch, model 01.462.0239). The mixture was then collected and dried overnight under vacuum at 40 °C. The thermal treatment of the prepared mixture was carried out in air, using a zirconium combustion boat. The adopted heating protocol comprised four isothermals, as follow: (i) 120 °C for 1h (RT to 120 °C, 5 °C min^{-1}); (ii) 500 °C for 1h (120 °C to 500 °C, 3 °C min^{-1}); (iii) 900 °C for 3h (500 °C to 900 °C, 5°C min^{-1}); (iv) 700 °C for 6h (900 °C to 700 °C, 5 °C min^{-1}). The furnace was then cooled down to room temperature. The obtained sample (about 1.5 g) was named as NaNMO for short.

4.2.3 All-solid-state synthesis

Manganese(II) Acetylactonate (MnAcAc anhydrous), Nickel (II) Acytelactonate (NiAcAc anhydrous) and sodium carbonate (Na_2CO_3) were mixed via wet ball-milling for 3h with ethanol. The powder was dried at 80 °C overnight and, then, calcinated. The amount of chemicals and the pyrolysis protocol were the same adopted in the colloidal assisted synthesis.

4.2.4 Electrochemical Measurements

The electrochemical characterization of NaNMO was carried out on composite electrodes with the procedure as introduced in Chapter II. The electrochemical behavior was tested by galvanostatic charge/discharge, cyclic voltammetry (CV) at 50 μV s^{-1} and electrochemical impedance spectroscopy (EIS). The cells were charged using a constant current protocol, at different currents (i.e. different C-rates: C/10, 1C, 2C and 5C, considering 1C = 120 mA g^{-1}) up to 4.4V vs. Na^+/Na. The cells were then discharged down to 2.0 V at the same C-rate used for the corresponding charging step. EIS analyses were performed at fully charged (4.4 V) cells, in the range 100 kHz-100 mHz, with a perturbation amplitude of 5 mV and 10 points per decade.

4.3. Results and Discussion

According to the literature, P2-type Na_xTMO_2 as cathode materials for NIBs are made either via a two steps sol-gel or co-precipitation method followed by a heat treatment[8, 20, 23, 24] or by a one-step,

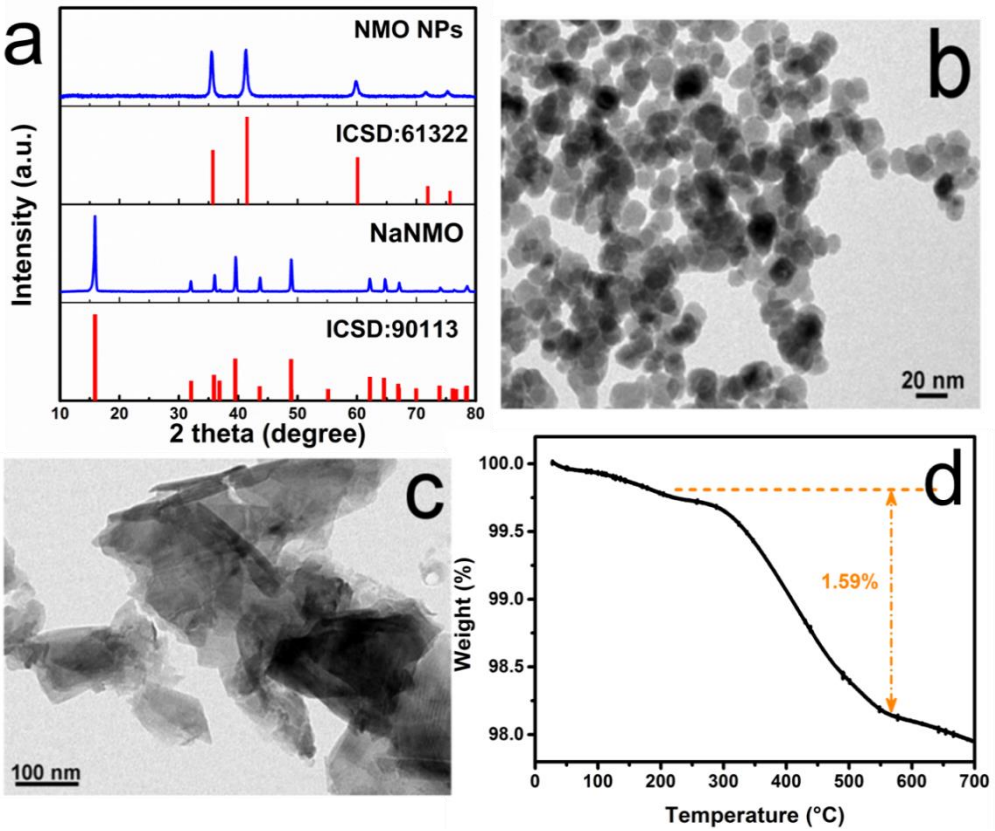

Figure 4.2 Structure and morphological characterization of the NMO NCs and NaNMO flakes. a). XRD patterns corresponding to pure $Ni_{0.25}Mn_{0.75}O$ with cubic structure (ICSD code: 61322) and the pure NaNMO with hexagonal layered structure (ICSD code: 90113). (b) and (c) low-magnification TEM images of NMO NCs and NaNMO flakes respectively d). The TGA analysis of NaNMO dryed powder: the vertical dotted arrow identifies the percentage of weight loss due to the decomposition of the carbonaceous layers.

all-solid-state reaction.[16, 21, 25, 26] In all cases, temperatures higher than 700 °C are required to achieve the final sodiated phase. Compared to the all-solid-state approach, co-precipitation and sol-gel (which are solution methods) methods may enable a more homogenous mixing of the precursors.[27] The approach that we have followed in this work to prepare $Na_{1.7}Ni_{1.0}Mn_{2.9}O_{7.6}$ comprises the following two steps: (i) a colloidal synthesis of $Ni_{0.25}Mn_{0.75}O$ (NMO) NCs (around 2 g of product), in which organic ligands such as oleylamine and octadecene are used to control the NCs growth and to tune their size, enabling a better control on the size of the NMO NCs compared

to the more conventional solution methods; (ii) a sodiation process through a solid-state reaction, by adding Na_2CO_3 to the purified NMO nanoparticles, which led to a NaNMO powder that preserved the Ni:Mn ratio of the NMO NCs.

The diffraction pattern from NMO dried powder could be indexed to the pure $Ni_{0.25}Mn_{0.75}O$ cubic structure (space group: Fm-3m, ICSD code:61322, see **Figure 4.2**a). The NCs had an average diameter around 10 nm (see TEM image of Figure 4.2b). After mechanical ball-mixing the NMO NCs with Na_2CO_3, the resulting powder was heated in air (see Experimental Section for details). The final product NaNMO sample was made of particles with flake-like shapes (see TEM image of Figure 4.2c).This thermal treatment in addition created a thin carbonaceous coating corresponding to almost 1.6 % wt. of the total NaNMO mass, as detected by TGA analysis (Figure 4.2d). As proven by the XRD pattern of Figure 4.2a (third one from top), the final NaNMO product had a pure P2-type hexagonal phase, characterized by a layered structure (space group: P63/mmc), similar to that reported for $Na_{0.58}Ni_{0.33}Mn_{0.67}O_{1.95}$ (ICSD code: 90113).[28]

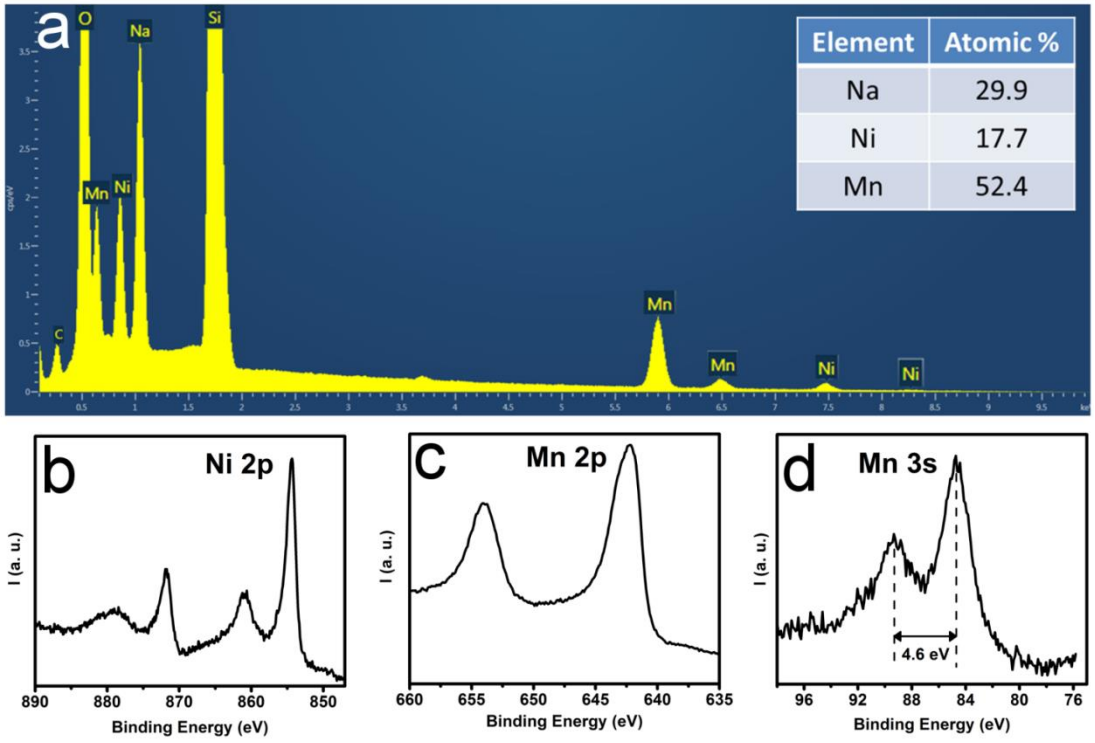

Figure 4.3. Compositional analysis of pristine NaNMO. (a) EDS spectra in which the atomic % of Na, Ni and Mn are expressed; XPS spectra of (b) Ni 2p, (c) Mn 2p and (d) Mn 3s.

The stoichiometry of the NaNMO sample was determined by EDS and XPS analysis of the sodiated powder. The EDS analysis (see **Figure 4.3**a) revealed a Na:Ni:Mn atomic ratio of 1.7:1.0:2.9, with a Mn:Ni ratio approaching 3, consistent with the stoichiometry of the starting NMO particles prepared by colloidal synthesis. The XPS data (Figure 4.3b-d) confirmed the presence of only Ni^{2+} and Mn^{4+} in the NaNMO structure. The oxygen stoichiometry in NaNMO was estimated by considering the atomic ratios of the metals (by EDS) and their oxidation states (by XPS), giving an overall composition for the NaNMO sample corresponding to $Na_{1.7}Ni_{1.0}Mn_{2.9}O_{7.6}$.

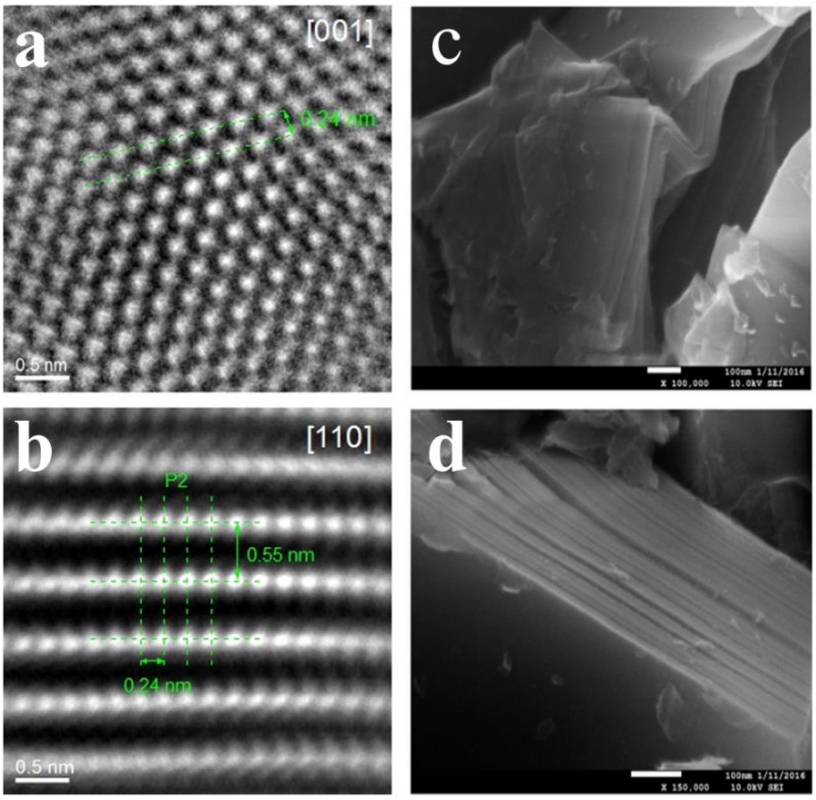

Figure 4.4. a,b) HRTEM images from top view and side view of a thin NaNMO flakes; c,d) High resolution SEM pictures of the pristine NaNMO powder with different magnifications.

HRTEM analysis was carried out on individual NaNMO flakes, working with a choice of aberration conditions [29] of the objective lens to give bright contrast on the heavier Ni/Mn ion columns in the structure (see **Figure 4.4**a-4.4b). The flakes had hexagonal structure, with the Ni/Mn ions in the [110] projection forming the rectangular sublattice, as expected from the P2 structure in this orientation. The measured interplanar distances (0.55 nm for (002) planes and 0.24 nm for (100)

planes) are in good agreement with the XRD data. SEM analysis (Figure 4.4c-4.4d) evidenced that each individual flake had a lamellar structure, made of stacks of several lamellae, each of them 10 nm thick (i.e. approximately composed of 20 Ni/Mi and Na layers).

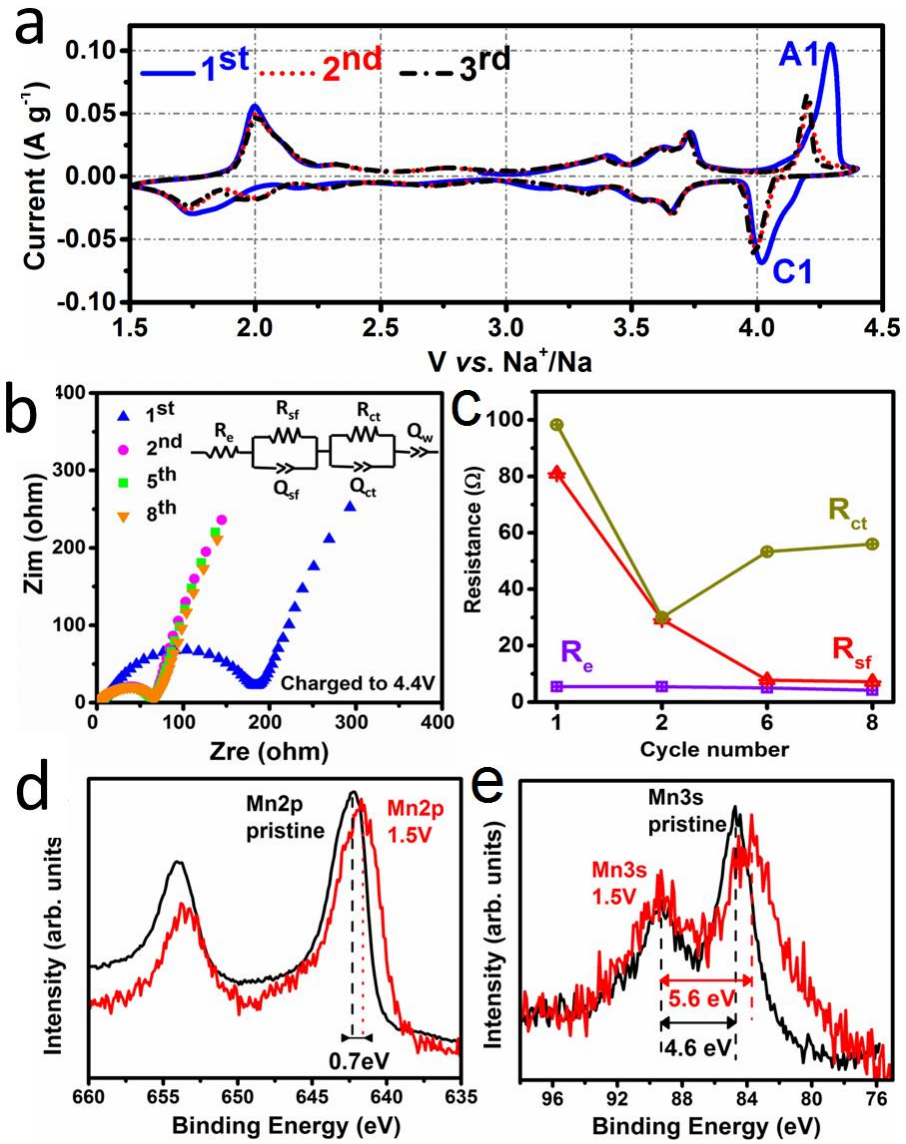

Figure 4.5. Electrochemical performances of NaNMO-based cathode. a) cyclic voltammetry performed at scan rate of 50 μV s^{-1} in the 1.5 - 4.4 voltage range with current normalized to the active material mass; (b,c) Electrochemical impedance study of NaNMO fully charged cathode at different galvanostatic charge/discharge cycles; b) Nyquist plot of the different cycles. Insert: scheme of the equivalent circuit that better fits the impedance data of the fully charged cells; c) Resistance values vs cycle number; d,e) XPS analysis of the deeply discharged (1.5 V) NaNMO cathode. Mn 2p (d) and Mn 3s (e) spectra of pristine NaNMO powder (black line) and deeply discharged NaNMO cathode (red), showing the reduction from Mn(IV) to Mn(III).

The electrochemical behavior of the NaNMO-based electrode was firstly investigated by cyclic voltammetry (CV). **Figure 4.5**a reports the first three consecutive voltammetric scans carried out between 1.5 and 4.4 V. Several pairs of peaks associated with the electrochemical Na-extraction and insertion are observed. The redox peaks located in the potential range of 3.0-3.8 V are related to the Red-Ox couple of $Ni^{2+}/Ni^{3+}/Ni^{3.5+}$.[18] It is known that Na-extraction/insertion in this voltage region does not modify the P2 structure of the oxide,[17] and therefore the electrode exhibits a generally good cyclability in such voltage range. The evidence that no changes in the abovementioned peaks potentials and currents were observed during the three CVs of Figure 3a supports the P2-phase stability of our NaNMO sample in this potential window. The well-defined anodic (A1) and cathodic (C1) peaks centered around 4.2 V correspond to the further oxidation of Ni^{3+} to Ni^{4+}.[8, 30] In a previously reported work on P2-type $Na_{2/3}Ni_xMn_yO_2$ (with Ni:Mn ratio of 1:2 [17, 19] and 1:3 [15, 23]) the redox processes occurring at potentials over 4 V were related to the P2/O2 phase transition. This transition, as described in the introduction, usually implies a structural instability of layered oxides and is responsible for the capacity fade upon cycling. Our data of Figure 3a indicate that the A1 and C1 peaks remained stable during cycling, with only a minor voltage shift after the 1st CV (from 4.29 to 4.20 V for A1 and from 4.02 to 3.99 V for C1). This A1 and C1 shift can be related to side reactions with the electrolyte that can occur at high voltage and that can form a first passivation layer on the cathode surface, as evidenced by impedance data of Figure 4.5b and 45c[31, 32].

EIS was used to investigate the sodium-ion transport during the electrochemical desodiation (charge) and sodiation (discharge) process. More specifically, we investigated the EIS of a fully charged electrode, to better understand the shift of the redox peaks A1 and C1 occurring between the first and the successive cycles of the cyclic voltammetries (CVs) of Figure 4.5a.

Nyquist plots of the fully charged cells at different cycles are shown in Figure 4.5b. The equivalent circuit that can better fits the EIS data is reported in Figure 4.5b inset and the fitting values are in **Table 4.1**. The R_e represent the uncompensated resistance (almost constant during the whole cycling test), in series with two parallel R/Q and Q_W (were Q is a constant phase element). In addition to the Ni^{2+}/Ni^{4+} redox processes, a series of peaks below 2.5 V were observed. By XPS analysis carried out on a NaNMO electrode discharged down to 1.5 V, we related these peaks to the Mn^{4+}/Mn^{3+} redox couple (Figure 4.5d-4.5e). The possibility to work at a potential as low as 1.5 V translates into a higher capacity (more Na^+ ions can be intercalated in the structure) at the expenses, however, of the final average working potential.

Table 4.1. Fitting parameters of the impedance spectra in of the charged NaNMO electrode in Figure 4.5b,c

Cycle	R_e (Ω)	$Q_{sf}(10^{-5})$	a_{sf}	R_{sf} (Ω)	$Q_{ct}(10^{-5})$	a_{ct}	R_{ct} (Ω)	$Q_w(10^{-3})$	a_w
1st	5.44	1.4	1.0	81.1	8.25	0.66	98.3	5.3	0.78
2nd	5.45	2.06	0.98	29.3	2.54	0.77	30.0	6.2	0.82
5th	5.02	3.27	0.81	7.9	3.94	0.75	53.3	6.5	0.81
8th	4.2	6.4	0.78	7.2	4.0	0.70	56.0	6.6	0.80

The 2nd and the 3rd voltammetric cycles of Figure 4.5a show similar behaviors, with a negligible variation in both peak potentials and currents. The good superimposition of consecutive CV scans, can be directly related to the chemical reversibility of the NaNMO cathode during the electrochemical desodiation (charge) and sodiation (discharge) processes. This behavior is most likely an indication that the removed Na-ion can be re-inserted in the layered crystal without significant structural changes, even if cycled in the high voltage region (> 4 V) where the above mentioned P2/O2 phase transition is expected to occur.

The NaNMO-based cathode was additionally tested by galvanostatic charge/discharge cycles at a C-rate of C/10 in the 2.0-4.4 voltage range. **Figure 4.6**a reports the voltage profile vs specific capacity (Q) for the 1st, 10th and 20th cycles, while the differential capacity analysis (dQ/dV vs V) of the same cycles is reported in Figure 4.6c. The good match of the 1st curve of Figure 3c (blue line) with the CVs of Figure 4.5a evidences that the multi-step voltage profile below 3.8 V is related to the Na^+ extraction within the P2-phase, while the long charge plateau at 4.2 V, with the typical shape of a two-phase transition, corresponds to the oxidation of Ni to Ni^{4+}. Both voltage profiles and dQ/dV curves indicate that the higher voltage discharge process was shifted from an initial value of 4.03 V to a stable value of 3.87 V upon cycling. The evolution of this plateau reflects an increase of the resistance during repeated Na-extractions/insertions, as corroborated by the increase of the Ohmic drops in Figure 4.6a. This behavior has been already reported in literature, and it has been usually associated to a pronounced capacity fade in the voltage region above 3.5 V [14, 15] resulting in a low delivered energy of the electrodes.

In order to quantify the capacity loss of our NaNMO-cathode related to the described voltage shift, we evaluated the discharge capacity delivered in the 2.0-3.5 and 3.5-4.4 voltage regions for the 1st,

10th and 20th cycle. Figure 4.6c reports the discharge capacity for both voltage ranges, normalized to the total discharge capacity delivered for each cycle. We found that the capacity delivered in the high voltage range represents more than the 40% of the total capacity, even after 20 cycles. This result confirms the good stability of the NaNMO-cathode in the high voltage (i.e. high energy) range. Our P2-NaNMO cathode presented an initial discharge capacity of 109 mAh g^{-1} corresponding to 92% of its theoretical value and a high capacity retention (of 93.6%) after 20 cycles, reaching a value of 102 mAh g^{-1}. Such stability is higher than that of previous works that reported, at best, a capacity retention of 80% in 20 cycles in a comparable voltage range.[23]

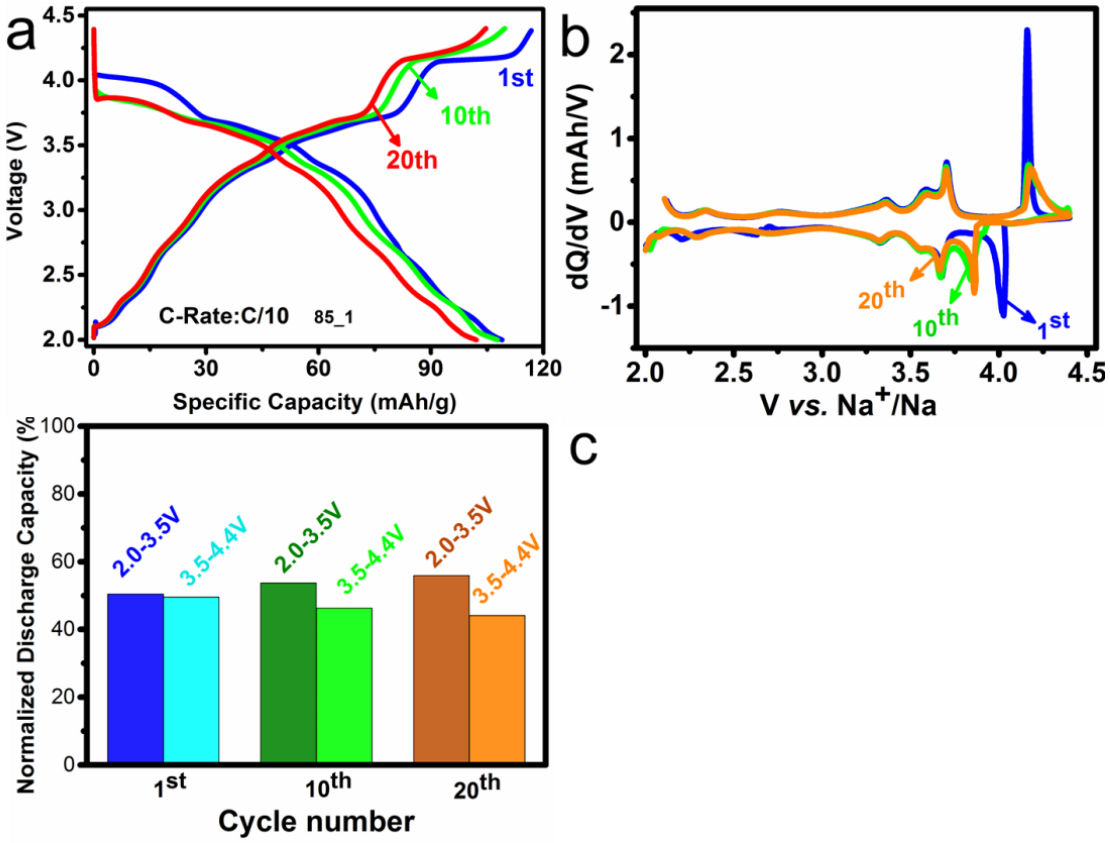

Figure 4.6. Electrochemical performances of NaNMO-based cathode. a) voltage profiles upon galvanostatic charge/discharge at 1st, 10th and 20th cycles of the NaNMO sample in 2.0 - 4.4 voltage range at C/10; b) the differential capacity (dQ/dV) vs. voltage for the 1st, 10th and 20th cycles of the NaNMO cells of **Figure 4.2c;** c) the discharge capacity of two different voltage ranges, normalized to the total discharge capacity delivered for each cycle.

To better understand the reasons of such high stability upon cycling in the 2.0-4.4V range, we investigated the effect of Na^+ intercalation/deintercalation process on the overall structure of the P2-NaNMO sample. **Figure 4.7**a reports a series of *in-operando* XRD patterns recorded on the electrode during the first electrochemical cycle (C-rate of C/20). The reflections related to the P2 phase were maintained during the whole charge/discharge process, with a progressive shift of the peaks during the desodiation process (blue curves of Figure 4.7a). The (002) and (004) peaks shifted to lower 2θ values while the (010) and (012) peaks moved to higher angles, consistent with an increase of the *c-axis* from 11.232Å to 11.379Å and a contraction of the *a-axis* from 2.873Å to 2.849Å. The gradual depletion of Na ions upon charging caused an increasing electrostatic repulsion between the oxygen atoms of consecutive TMO_6 layers.

To minimize this repulsion, the oxide layers move along the *c-axis* of the P2 structure, resulting in the observed cell expansion.[17, 33] The XRD pattern recorded on the deeply desodiated NaNMO-electrode charged above 4.0 V showed the predominant presence of the peaks of the original P2 phase and a new weak peak at 17.8 °2θ. This new peak is in accordance with the presence of a disordered "Z" phase, as recently reported for P2-$Na_x[Mn_{1/2}Fe_{1/2}]O_2$[34, 35]. It is worth to note that the literature results for Fe-based oxides showed a complete transition from P2 to "Z" phase during desodiation, while our fully charged NaNMO, preserves mainly the original P2 phase, with a minor presence of the "Z" phase. The (002) and (004) peaks of P2 shifted towards high angles and the (010) and (012) peaks moved to low angles during the discharge process, moreover, the peak related to "Z" phase disappeared as well at the beginning of the sodiation process, corresponding to the reversible sodium insertion process.

After the first cycle, the electrode was subjected to *in-operando* XRD measurements for the second cycle as shown in **Figure 4.8**a. The corresponding XRD pattern indicated a complete recovery of the 1st cycle phase. Figure 4.8b compares the XRD patterns of the pristine NaNMO with that of the electrode discharged at 2.0 V after 100 charge/discharge cycles at 2.0-4.4 V. Here, the top pattern contains broad and low intensity peaks that can be mainly attributed to the original P2 phase, suggesting a good reversibility of sodiation/desodiation process even after a long cycling test. It is worth to note that no peaks related to the O2 phase (typically at 21° in 2θ) were detected,[19, 33] even after 100 cycles. We can conclude that the usually observed detrimental P2/O2 phase transition is actually suppressed in the present $Na_{1.7}Ni_{1.0}Mn_{2.9}O_{7.6}$-based cathodes and that the partial P2/"Z" transition take place. The preservation of the P2 phase even at high voltage (i.e. at deep desodiation stage) is the main reason for the good stability (i.e. high capacity retention) observed during the galvanostatic charge/discharge cycles of the NaNMO cathode in the 2.0-4.4V range.

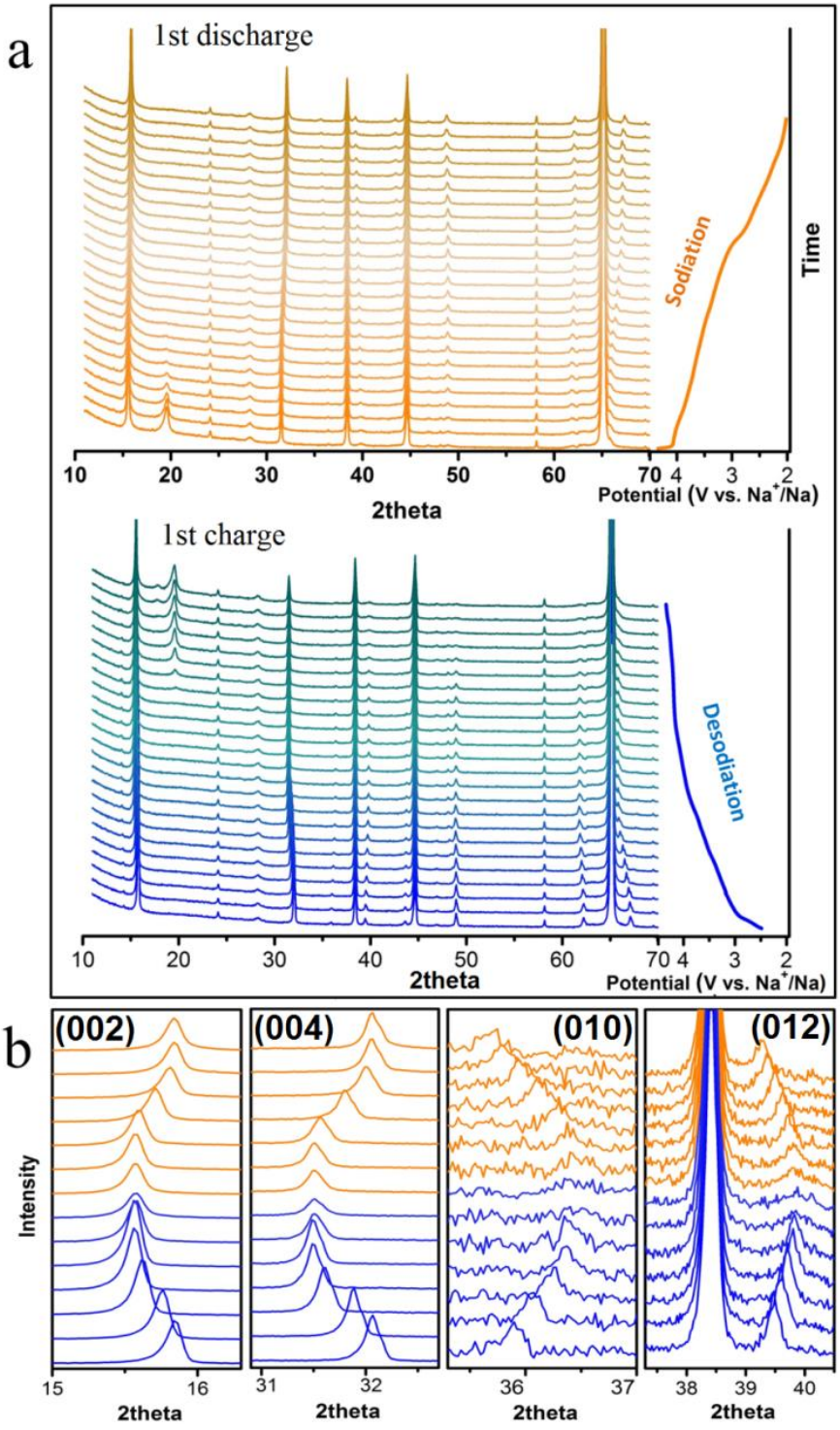

Figure 4.7. *In-operando* XRD characterization upon charge/discharge process of P2-NaNMO-based cathode. a) XRD patterns of the cathode at different charge/discharge voltages in the 2.0-4.4 V range (blue curves are the desodiation process and the orange curves are the sodiation process); b) the peaks shift indication of *in-operando* XRD patterns at different voltage during charge/discharge.

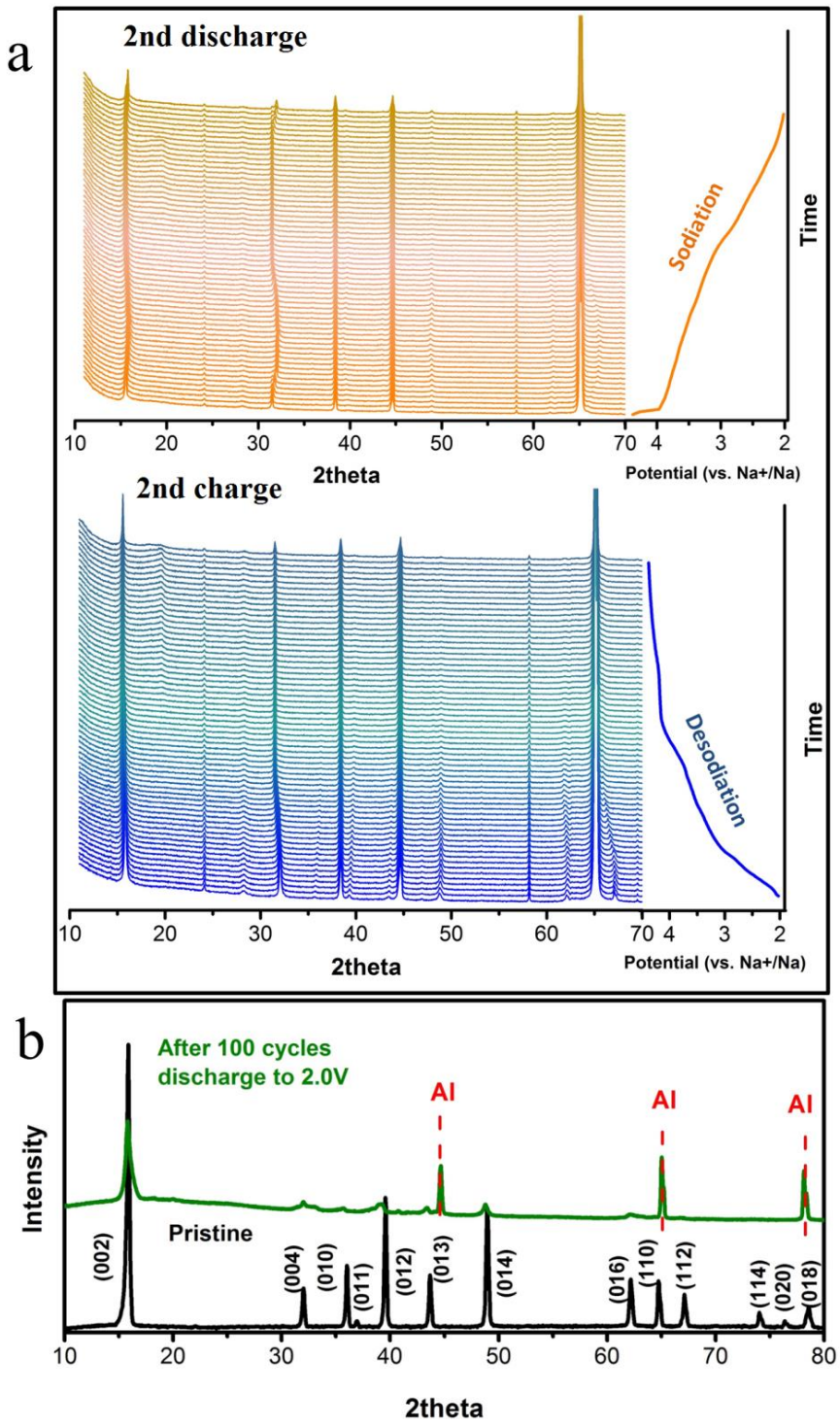

Figure 4.8. *In-operando* XRD characterization upon charge/discharge process of P2-NaNMO-based cathode for the second cycle. a) XRD patterns of the cathode at different charge/discharge voltages in the 2.0-4.4 V range (blue curves are the desodiation process and the orange curves are the sodiation process); b) XRD patters of a discharged (2.0 V) NaNMO-based cathode after 100 charge/discharge cycles and of the pristine electrode.

$Na_{1.7}Ni_{1.0}Mn_{2.9}O_{7.6}$ powder sample was even synthesized following a one-step, all-solid-state (ssNaNMO) route (details of the synthesis are reported in the Experimental Section). Structural and electrochemical characterizations of the samples prepared through both colloidally-assisted two step synthesis and all-solid state approach are compared in **Figure 4.9**. Differently from the colloidally-assisted solid state reaction, the all solid-state method produced a small amount of impurities (mainly sodium carbonate) detectable in the XRD pattern and in the EDS analysis (Figure 4.9a and 4.9b respectively). The inhomogeneities of the ssNaNMO sample were reflected in the poor electrochemical performance of the corresponding electrode, as visible from the cyclic voltammetries reported in Figure 4.9c. For this reasons, we focused our efforts on the study of the cycling performances of NaNMO composite cathodes obtained by colloidal-assisted solid state reaction. To investigate the effect of the voltage cut off on the electrochemical behavior of NaNMO-based cathodes, we performed galvanostatic charge/discharge cycles at C/10 in three different potential ranges: 2.2-3.8V, 2.0-4.4V and 1.5-4.4V. As shown in **Figure 4.10**a, the initial voltage profiles of the three samples exhibited good overlap in the common voltage ranges, indicating that the phase transitions associated with Na^+ insertion/deinsertion are weakly affected by the adopted charged/discharged voltage window. The cycling stabilities of the three samples are reported in Figure 4.10b. During the first 20 cycles at C/10, the NaNMO-based electrodes exhibited a specific discharge capacity of 72, 109 and 155 mAh g^{-1}, which increased by broadening the adopted voltage range. The cathode cycled in the restricted range of 2.2-3.8V evidenced, as expected, an excellent cycling stability, with almost no capacity fade and a coulombic efficiency approaching 100% after the first 4 cycles. However, even the electrodes cycled in the 2.0-4.4V and 1.5-4.4V voltage ranges had remarkable high cycling performances, with capacity fade of 0.33% per cycle when charge/discharge in 2.0-4.4 V range, and of 0.51% in the case of the deep discharged electrode (down to 1.5V).

From the aforementioned cycling performances we decided to further investigate the rate capability of NaNMO-cathode cycled in the 2.0-4.4 V range. We did not consider further the 1.5-4.4V range in which the lower stability was seen, as well as 2.2-3.8 V window, in which we recorded the smallest discharge capacity among the three ranges. Figure 4.10c reports the discharge capacity upon galvanostatic charge/discharge cycles at C-rates ranging from C/10 to 5C. After the first four equilibration cycles at C/10, the NaNMO-cathode exhibited a starting specific capacity of 94 mAh g^{-1} at 1C with a low capacity fade of 0.22% per cycle, reaching a value of 84 mAh g^{-1} in 50 cycles (i.e. capacity retention of almost 90%).

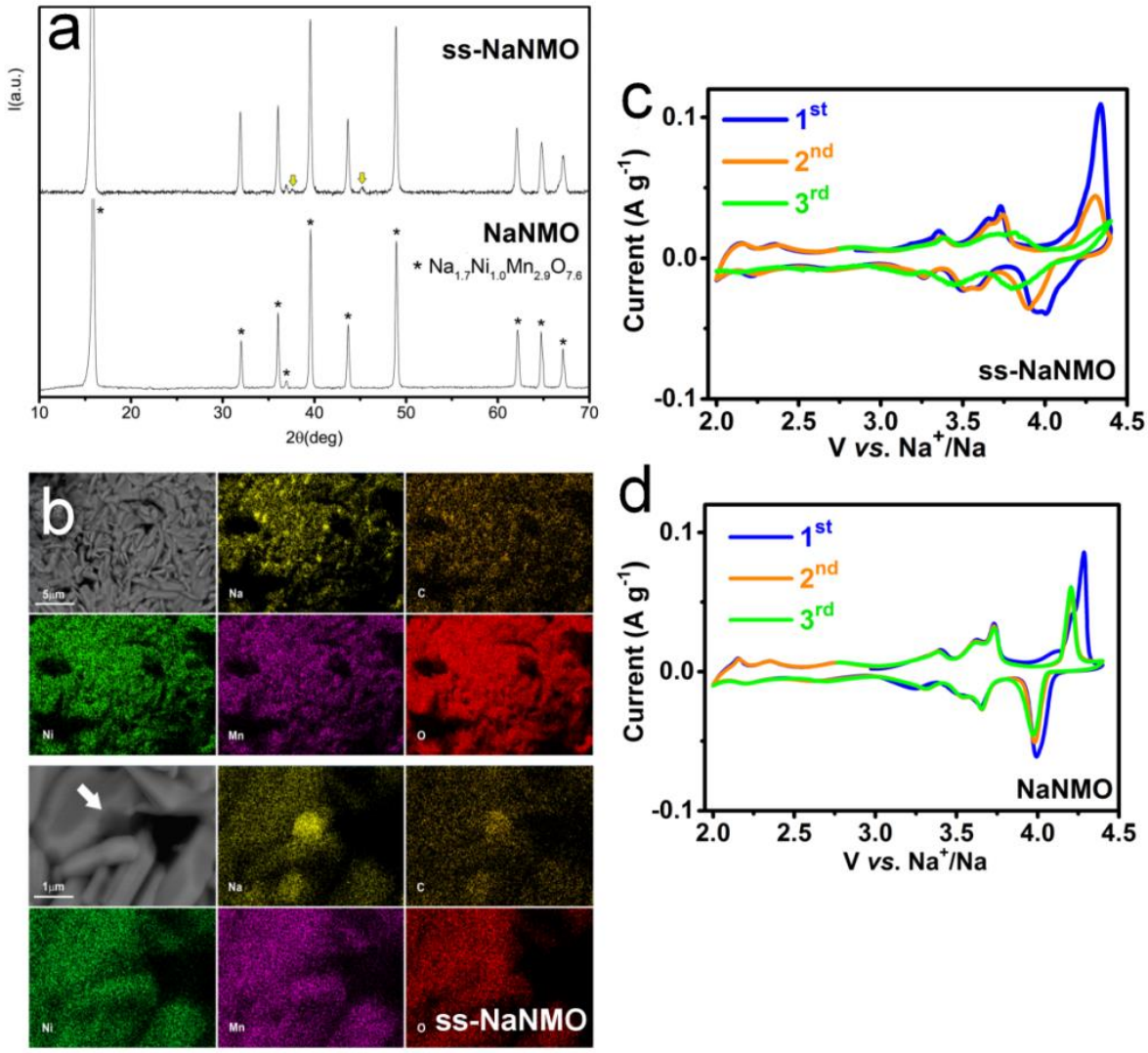

Figure 4.9. Structural and electrochemical characterization of ss-NaNMO and NaNMO-based electrodes. a) XRD patterns which evidence the presence of impurities in ss-NaNMO sample; b) HRSEM-EDS analysis that shows Na/C reach particles in the ss-NaNMO; the first three cyclic voltammetries at 50 μV s^{-1} of (c) ss-NaNMO and (d) NaNMO.

At 2C and 5C the capacity values were 67 mAh g^{-1} and 37 mAh g^{-1}, respectively. At the end of the whole charge/discharge protocol (more than 120 cycles at different C-rates), the NaNMO-cathode delivered, at 1C, a capacity of 77.4 mAh g^{-1}, corresponding to 82% of its initial capacity. The good cycling performance at both low (C/10) and high (1C) C-rates of our NaNMO-cathode when cycled at potential higher than 4 V, is primary attributed to the suppression of P2/O2 phase transition, as supported by XRD analysis.

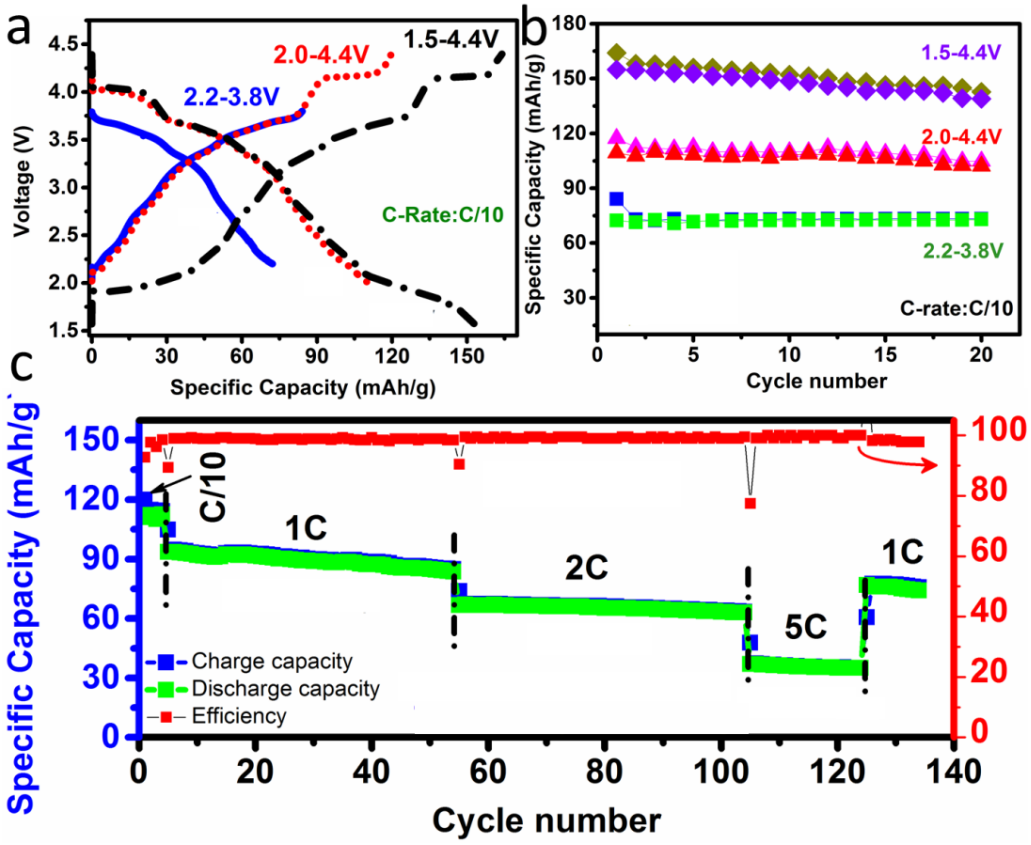

Figure 4.10. Galvanostatic charge/discharge performances of NaNMO-based cathodes. a) Initial voltage profiles and b) galvanostatic charge/dischargee performances of NaNMO-cathode cycled at C/10 in different voltage range: 2.2-3.8 V, 2.0-4.4 V and 1.5-4.4 V. c) cycle performances of the NaNMO sample at different C-rate: C/10, 1C, 2C and 5C in the range of 2.0-4.4 V.

To further understand the reasons for the good performance, the electron diffraction tomography (EDT) electron diffraction have been carried out to study the structure of NaNMO sample. The electron diffraction patterns are recorded while the sample is rotated around the goniometer axis in discrete step of 1°[36] . To avoid loss of reciprocal space in between the step the patterns are recorded in precession mode with the electron beam precessing on a cone surface with the vertex fixed on the sample plane[37]. The aperture semiangle of the cone in general is equal to the angular step in between the patterns. Thanks to the combine effect of the random orientation of the patterns, that in general is far from zone axes, and to the reciprocal space integration done by the precession, the electron diffraction intensities obtained in this way are close to a kinematical approximation and can

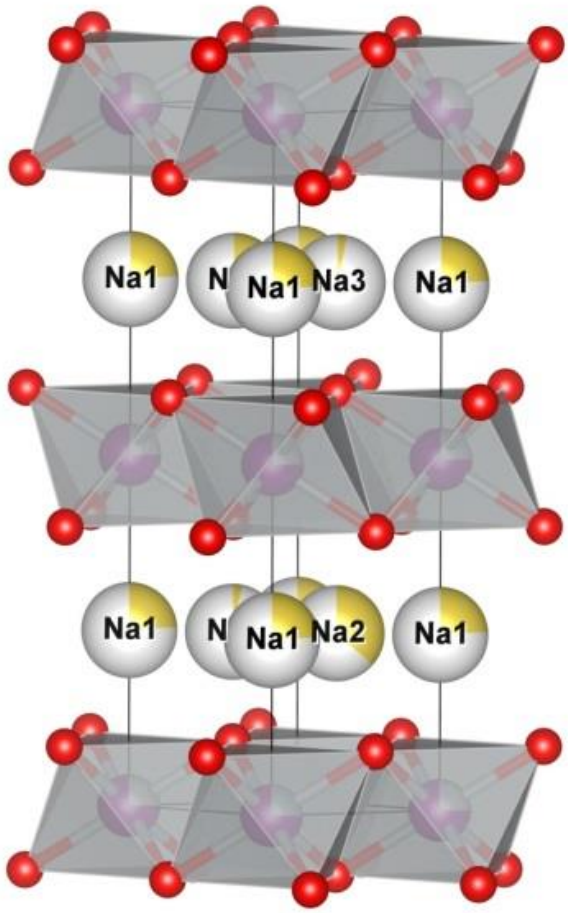

Fig. 4.11 . The structure as refined by Rietveld.

therefore be used to solve the crystal structure with conventional structure solution approaches like direct methods or charge flipping.

The powder x-ray pattern can be indexed with an hexagonal unit cell having a_1=2.8774(1) Å and c_1=11.1822(1) Å. Rietveld refinement starting with the structural model from Paulsen[38] at al 2000, gives only two out of three Na sites with a not negligible occupancy (0.24, 0.36). These sites are those having a trigonal prismatic coordination with the oxygen (**Figure 4.11**). The third Na site, that for being occupied would require a very short Na oxygen distance, has occupancy of only 0.03. Electron diffraction tomography collected on small areas (beam size 150 nm) of micrometric crystal grains revealed a more complex nature of the compound. In the majority of the grains the

reflections can be indexed with the hexagonal unit cell determined with X-ray and a strong streaking along the c axis indicates a disorder on the a b plane with possible shifts parallel to this plane between the layers, as shown in **Figure 4.12**.

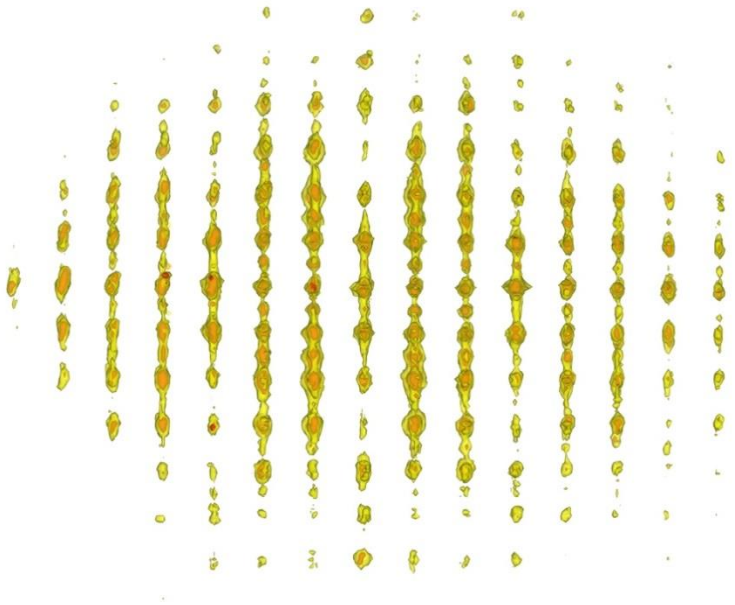

Fig. 4.12 Three dimensional reconstruction of the reciprocal space of the unmodulated structure view along (110). The presence of diffuse scattering along the c direction (vertical) is evident.

Interestingly to solve the crystal structure the symmetry must be reduced from $P6_3/mmc$ to $P6_322$. In the reduced symmetry the solution obtained correspond to the structure refined with X-ray but only the most occupied Na site can be retrieved, Na2. In a minority of crystals (around 20%) weak superstructure reflections can be detected. The reciprocal space of these crystals can be indexed with a new hexagonal cell rotated 30° around c having $a_2=\sqrt[2]{3}\ a_1$ =5.0 Å and the same c axis of 11.2 Å (**Figure 4.13**).

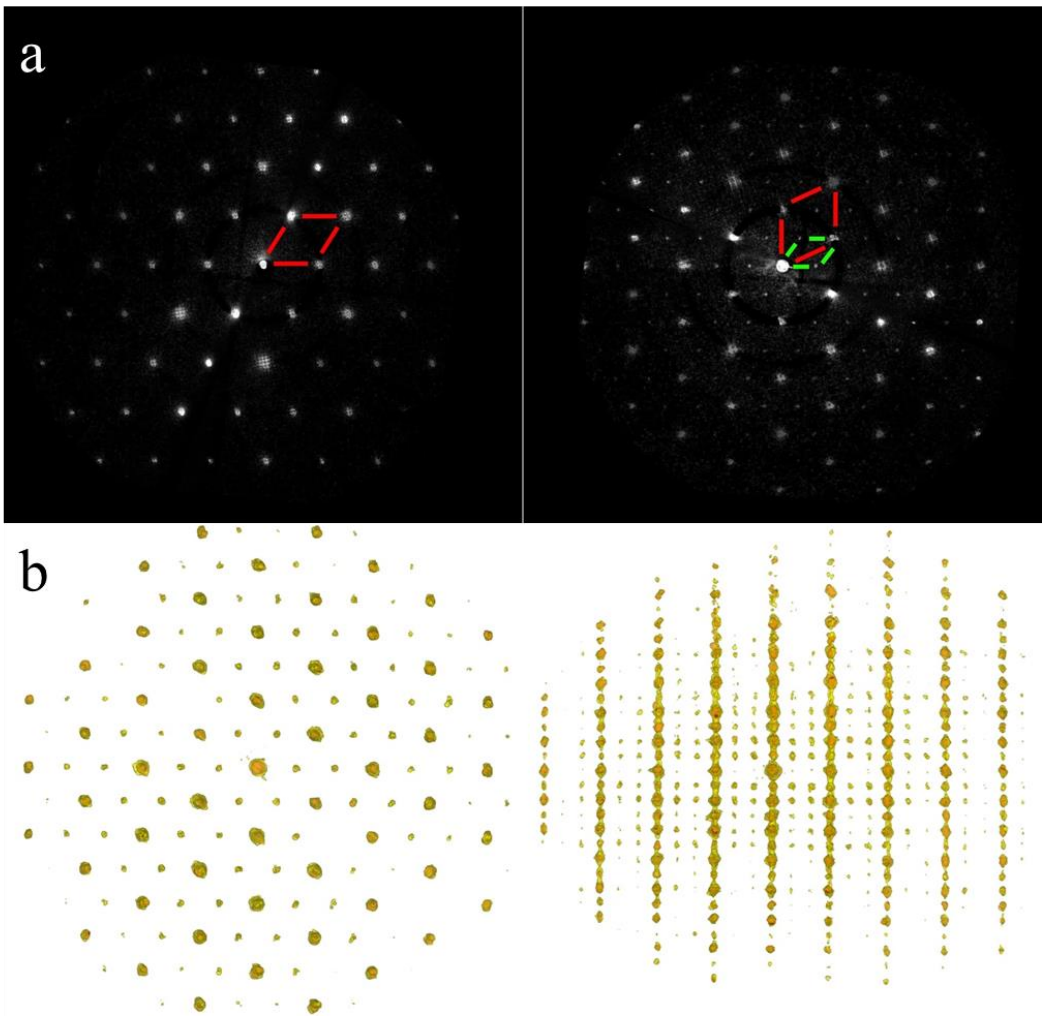

Figure 4.13. (a). hk0 sections of the reconstructed three dimensional reciprocal space of the unmodulated (left) and modulated (right) structure obtained with electron diffraction tomography. The unmodulated and modulated reciprocal cells are reported in red and green respectively; (b). Three dimensional reconstruction of the reciprocal space of the modulated structure view along (001) (left) and (100) (right). The weak superstructure spots are clearly evident.

Structure solution with direct methods on three dimensional set of intensities extracted accordingly with this indexing can be achieved in space group $P6_322$. The solution shows an ordering of Ni and Mn in the octahedral layer with one out of three octahedral sites having longer cation oxygen distances (2.04 vs 1.87-1.88 Å) thus preferentially occupied by Ni (**Figure 4.14**). In the Na layer just one Na position is retrieved corresponding to the Na1 site of the unmodulated structure.

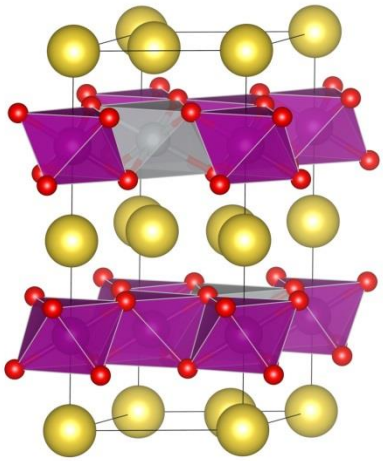

Figure. 4.14. The modulated structure. In gray and in purple the octahedral preferentially occupied by Ni and Mn respectively.

Based on the EDT results, we speculate on the role of the complex structure during the charge/discharge process: When the Na^+ extracted from the P2-NaNMO structure, an energetically stable phase O2-type phase is supposed to be achieved by gliding of MO_2 slabs. However, the disordered structure on TMO slab makes this glide process difficult, which inhibits the P2-O2 phase transition.

4.4. Conclusion

A pure phase $Na_{1.7}Ni_{1.0}Mn_{2.9}O_{7.6}$ layered oxide with a P2-type structure were prepared through a two-step synthesis comprising a first colloidal step followed by a second sodiation step carried out *via* a solid state reaction. By the adopted synthetic protocol and working at Na:Ni:Mn ratios of 1.7:1:3, a cathode material was able to be produced for Sodium-ion batteries that could withstand long charge/discharge cycles at working voltages up to 4.4 V vs. Na^+/Na. The P2-$Na_{1.7}Ni_{1.0}Mn_{2.9}O_{7.6}$ electrodes presented, at the relatively low C-rate of C/10, an initial discharge capacity of 109 mAh g^{-1} (i.e. 92% of its theoretical value) and a capacity retention of 93.6% after 20 cycles. At the higher C-rate of 1C the delivered discharge capacity was 94 mAh g^{-1} with a capacity retention of almost 90% in 50 cycles. We demonstrated, *via in-operando* carried out on the electrode at different charge/discharge voltages up to 4.4 V, that the aforementioned good cycling performances at both low and high C-rates are primary due to the suppression of the detrimental

P2/O2 phase transition. This unique feature has been attributed to the peculiar crystalline patterning revealed by EDT, which is supposed to buffer and sensibly reduce TMO gliding process during repetitive cycling.

4.5 References

1. Nithya, C.; Gopukumar, S., Sodium ion batteries: a newer electrochemical storage. *Wiley Interdisciplinary Reviews: Energy and Environment* **2015,** 4, (3), 253-278.

2. Han, M. H.; Gonzalo, E.; Singh, G.; Rojo, T., A comprehensive review of sodium layered oxides: powerful cathodes for Na-ion batteries. *Energy & Environmental Science* **2015,** 8, (1), 81-102.

3. Komaba, S.; Takei, C.; Nakayama, T.; Ogata, A.; Yabuuchi, N., Electrochemical intercalation activity of layered $NaCrO_2$ vs. $LiCrO_2$. *Electrochemistry Communications* **2010,** 12, (3), 355-358.

4. Ma, X.; Chen, H.; Ceder, G., Electrochemical properties of monoclinic $NaMnO_2$. *Journal of The Electrochemical Society* **2011,** 158, (12), A1307-A1312.

5. Zhao, J.; Zhao, L.; Dimov, N.; Okada, S.; Nishida, T., Electrochemical and thermal properties of α-$NaFeO_2$ cathode for Na-Ion batteries. *Journal of The Electrochemical Society* **2013,** 160, (5), A3077-A3081.

6. Delmas, C.; Braconnier, J.-J.; Fouassier, C.; Hagenmuller, P., Electrochemical intercalation of sodium in Na_xCoO_2 bronzes. *Solid State Ionics* **1981,** 3, 165-169.

7. Delmas, C.; Borthomieu, Y.; Faure, C.; Delahaye, A.; Figlarz, M., Nickel hydroxide and derived phases obtained by chimie douce from $NaNiO_2$. *Solid State Ionics* **1989,** 32, 104-111.

8. Hasa, I.; Buchholz, D.; Passerini, S.; Scrosati, B.; Hassoun, J., High Performance Na0. 5 $[Ni_{0.23}Fe_{0.13}Mn_{0.63}]O_2$ Cathode for Sodium-Ion Batteries. *Advanced Energy Materials* **2014,** 4, (15).

9. Delmas, C.; Fouassier, C.; Hagenmuller, P., Structural classification and properties of the layered oxides. *Physica B+ C* **1980,** 99, (1), 81-85.

10. Komaba, S.; Yabuuchi, N.; Nakayama, T.; Ogata, A.; Ishikawa, T.; Nakai, I., Study on the Reversible Electrode Reaction of $Na_{1-x}Ni_{0.5}Mn_{0.5}O_2$ for a Rechargeable Sodium-Ion Battery. *Inorganic chemistry* **2012,** 51, (11), 6211-6220.

11. Kubota, K.; Yabuuchi, N.; Yoshida, H.; Dahbi, M.; Komaba, S., Layered oxides as positive electrode materials for Na-ion batteries. *MRS Bulletin* **2014,** 39, (05), 416-422.

12. Mendiboure, A.; Delmas, C.; Hagenmuller, P., Electrochemical intercalation and deintercalation of Na_xMnO_2 bronzes. *Journal of Solid State Chemistry* **1985,** 57, (3), 323-331.

13. Saadoune, I.; Maazaz, A.; Ménétrier, M.; Delmas, C., On the $Na_xNi_{0.6}Co_{0.4}O_2$ system: physical and electrochemical studies. *Journal of Solid State Chemistry* **1996,** 122, (1), 111-117.

14. Wang, H.; Yang, B.; Liao, X.-Z.; Xu, J.; Yang, D.; He, Y.-S.; Ma, Z.-F., Electrochemical properties of P2-$Na_{2/3}[Ni_{1/3}Mn_{2/3}]O_2$ cathode material for sodium ion batteries when cycled in different voltage ranges. *Electrochimica Acta* **2013,** 113, 200-204.

15. Zhao, W.; Tanaka, A.; Momosaki, K.; Yamamoto, S.; Zhang, F.; Guo, Q.; Noguchi, H., Enhanced electrochemical performance of Ti substituted P2-$Na_{2/3}Ni_{1/4}Mn_{3/4}O_2$ cathode material for sodium ion batteries. *Electrochimica Acta* **2015,** 170, 171-181.

16. Yoshida, H.; Yabuuchi, N.; Kubota, K.; Ikeuchi, I.; Garsuch, A.; Schulz-Dobrick, M.; Komaba, S., P2-type $Na_{2/3}Ni_{1/3}Mn_{2/3-x}Ti_xO_2$ as a new positive electrode for higher energy Na-ion batteries. *Chemical Communications* **2014,** 50, (28), 3677-3680.

17. Lee, D. H.; Xu, J.; Meng, Y. S., An advanced cathode for Na-ion batteries with high rate and excellent structural stability. *Physical Chemistry Chemical Physics* **2013,** 15, (9), 3304-3312.

18. Wen, Y.; Wang, B.; Zeng, G.; Nogita, K.; Ye, D.; Wang, L., Electrochemical and Structural Study of Layered P2-Type $Na_{2/3}N_{i1/3}Mn_{2/3}O_2$ as Cathode Material for Sodium-Ion Battery. *Chemistry–An Asian Journal* **2015,** 10, (3), 661-666.

19. Wang, P. F.; You, Y.; Yin, Y. X.; Wang, Y. S.; Wan, L. J.; Gu, L.; Guo, Y. G., Suppressing the P2–O2 Phase Transition of $Na_{0.67}Mn_{0\ 67}N_{i0.33}O_2$ by Magnesium Substitution for Improved Sodium-Ion Batteries. *Angewandte Chemie* **2016**.

20. Xu, J.; Lee, D. H.; Clément, R. l. J.; Yu, X.; Leskes, M.; Pell, A. J.; Pintacuda, G.; Yang, X.-Q.; Grey, C. P.; Meng, Y. S., Identifying the Critical Role of Li Substitution in P2–$Na_x[Li_yNi_zMn1_{-y-z}]O_2$ (0< x, y, z< 1) Intercalation Cathode Materials for High-Energy Na-Ion Batteries. *Chemistry of Materials* **2014,** 26, (2), 1260-1269.

21. Wu, X.; Guo, J.; Wang, D.; Zhong, G.; McDonald, M. J.; Yang, Y., P2-type $Na_{0.66}Ni_{0.33-x}Zn_xMn_{0.67}O_2$ as new high-voltage cathode materials for sodium-ion batteries. *Journal of Power Sources* **2015,** 281, 18-26.

22. Kang, W.; Zhang, Z.; Lee, P.-K.; Ng, T.-W.; Li, W.; Tang, Y.; Zhang, W.; Lee, C.-S.; Yu, D. Y. W., Copper substituted P2-type $Na_{0.67}Cu_xMn_{1-x}O_2$: a stable high-power sodium-ion battery cathode. *Journal of Materials Chemistry A* **2015,** 3, (45), 22846-22852.

23. Manikandan, P.; Ramasubramonian, D.; Shaijumon, M., Layered P2-type $Na_{0.5}Ni_{0.25}Mn_{0.75}O_2$ as a high performance cathode material for sodium-ion batteries. *Electrochimica Acta* **2016,** 206, 199-206.

24. Buchholz, D.; Moretti, A.; Kloepsch, R.; Nowak, S.; Siozios, V.; Winter, M.; Passerini, S., Toward Na-ion Batteries Synthesis and Characterization of a Novel High Capacity Na Ion Intercalation Material. *Chemistry of Materials* **2013,** 25, (2), 142-148.

25. Wang, Y.; Xiao, R.; Hu, Y.-S.; Avdeev, M.; Chen, L., P2-$Na_{0.6}[Cr_{0.6}Ti_{0.4}]O_2$ cation-disordered electrode for high-rate symmetric rechargeable sodium-ion batteries. *Nature communications* **2015,** 6.

26. Park, K.; Han, D.; Shon, J.; Doo, S. G.; Lee, S., Characterization of a thin, uniform coating on P2-type $Na_{2/3}Fe_{1/2}Mn_{1/2}O_2$ cathode material for sodium-ion batteries. *RSC Advances* **2015,** 5, (9), 6340-6344.

27. Li, M.; Zhang, L.-L.; Yang, X.-L.; Huang, Y.-H.; Sun, H.-B.; Ni, S.-B.; Tao, H.-C., Synthesis and electrochemical performance of Li_2FeSiO_4/C cathode material using ascorbic acid as an additive. *Journal of Solid State Electrochemistry* **2015,** 19, (2), 415-421.

28. Paulsen, J.; Donaberger, R.; Dahn, J., Layered T2-, O6-, O2-, and P2-Type A2/3$[M'^{2+}_{1/3}M^{4+}_{2/3}]O_2$ Bronzes, A= Li, Na; M'= Ni, Mg; M= Mn, Ti. *Chemistry of materials* **2000,** 12, (8), 2257-2267.

29. Bertoni, G.; Grillo, V.; Brescia, R.; Ke, X.; Bals, S.; Catellani, A.; Li, H.; Manna, L., Direct determination of polarity, faceting, and core location in colloidal core/shell wurtzite semiconductor nanocrystals. *ACS nano* **2012,** 6, (7), 6453-6461.

30. Yuan, D.; Hu, X.; Qian, J.; Pei, F.; Wu, F.; Mao, R.; Ai, X.; Yang, H.; Cao, Y., P2-type $Na_{.67}Mn_{0.65}Fe_{0.2}Ni_{0.15}O_2$ cathode material with high-capacity for sodium-ion battery. *Electrochimica Acta* **2014,** 116, 300-305.

31. Monaco, S.; De Giorgio, F.; Da ColV s-1, L.; Riché, M.; Arbizzani, C.; Mastragostino, M., Electrochemical performance of $LiNi_{0.5}Mn_{1.5}O_4$ composite electrodes featuring carbons and reduced graphene oxide. *Journal of Power Sources* **2015,** 278, 733-740.

32. Shanmugam, R.; Lai, W., Study of Transport Properties and Interfacial Kinetics of $Na_{2/3}[Ni_{1/3}Mn_xTi_{2/3-x}]O_2$ (x=0,1/3) as Electrodes for Na-Ion Batteries. *Journal of The Electrochemical Society* **2015,** 162, (1), A8-A14.

33. Lu, Z.; Dahn, J., In Situ X-Ray Diffraction Study of P 2 $Na_{2/3}[Ni_{1/3}Mn_{2/3}]O_2$. *Journal of The Electrochemical Society* **2001,** 148, (11), A1225-A1229.

34. Talaie, E.; Duffort, V.; Smith, H. L.; Fultz, B.; Nazar, L. F., Structure of the high voltage phase of layered P2-$Na_{2/3-z}[Mn_{1/2}Fe_{1/2}]O_2$ and the positive effect of Ni substitution on its stability. *Energy & Environmental Science* **2015,** 8, (8), 2512-2523.

35. Mortemard de Boisse, B.; Carlier, D.; Guignard, M.; Bourgeois, L.; Delmas, C., P2-$Na_xMn_{1/2}Fe_{1/2}O_2$ Phase Used as Positive Electrode in Na Batteries: Structural Changes Induced by the Electrochemical (De) intercalation Process. *Inorganic chemistry* **2014,** 53, (20), 11197-11205.

36. Kolb, U.; Gorelik, T.; Kübel, C.; Otten, M.; Hubert, D., Towards automated diffraction tomography: Part I—Data acquisition. *Ultramicroscopy* **2007,** 107, (6), 507-513.

37. Mugnaioli, E.; Gorelik, T.; Kolb, U., "Ab initio" structure solution from electron diffraction data obtained by a combination of automated diffraction tomography and precession technique. *Ultramicroscopy* **2009,** 109, (6), 758-765.

38. Paulsen, J.; Donaberger, R.; Dahn, J., Layered T2-, O6-, O2-, and P2-Type $A_{2/3}[M'^{2+}_{1/3}M^{4+}_{2/3}]O_2$ Bronzes, A= Li, Na; M '= Ni, Mg; M= Mn, Ti. *Chemistry of materials* **2000,** 12, (8), 2257-2267.

CHAPTER V

Synthesis and electrochemical study of bi-functional layered material $Na_xNi_{x/2}Ti_{1-x/2}O_2$ ($0.60 \leq x \leq 1.0$) as electrode materials for Na-ion battery

5.1 Introduction

Layered oxides Na_xCoO_2[1, 2], $NaMnO_2$[3-5] and $NaNiO_2$[6-8] have been investigated and they displayed charge/discharge profiles with irregular voltage plateaus, which could result in rapid capacity decay during cycling. The cooperative effect of multiple transition metals in metal oxide layers has proven to be effective in removing multiple plateaus, increasing the average voltage and increasing reversible capacity. Good electrochemical behaviors were thus reported in P2-type oxides such as $Na_xNi_{1/3}Mn_{2/3}O_2$[9, 10], $Na_xFe_{1/2}Mn_{1/2}O_2$[11], $Na_{0.45}Ni_{0.22}Co_{0.11}Mn_{0.66}O_2$[12], $Na_{0.85}(Li_{0.17}Ni_{0.21}Mn_{0.64})O_2$[13]. Among all the layered oxides, Ni-containing[9, 13, 14] layered oxide are interesting system because the overall electrochemical performance is based on the $Ni^{2+/3+/4+}$ Red-Ox couple which has a relatively high operating voltage. On the other hand, Ti-based Na-ion battery anode materials have attracted attention because their efficient Na-storage activity, high stability, low cost and nontoxicity[15-17]. Ti-based layered oxide, such as P2-$Na_{0.66}[Li_{0.22}Ti_{0.78}]O_2$[18], P2-$Na_{2/3}Co_{1/3}Ti_{2/3}O_2$[19] and P2-$Na_{0.6}[Cr_{0.6}Ti_{0.4}]O_2$[20] systems, have been studied and they deliver a safe potential of about 0.7 V (vs. Na^+/Na) based on Ti^{3+}/Ti^{4+} redox potential. It has been demonstrated as a potential anode material for long life NIBs. 'Bi-polar' properties have been investigated in the NASICON structure material $Na_3V_2(PO_4)_3$[21, 22] by using V^{4+}/V^{3+} (3.8 V vs. Na^+/Na) and V^{3+}/V^{2+} (1.75 V vs. Na^+/Na) redox couples, respectively. It has been shown to work as both cathode and anode in NIBs. However, the toxicity of vanadium can potentially become a big issue from environmental and commercial point of view. Considering the similar ionic radius of nickel and titanium, Zhou's group designed and synthesized O3-type layered $Na_{0.8}Ni_{0.4}Ti_{0.6}O_2$[23] material and found the 'golden pair' of Ni-Ti not only greatly stabilized each other in the sodium electrochemical process, but also exhibited the unique double redox couples of Ni^{4+}/Ni^{3+} (3.5V vs Na^+/Na) and Ti^{4+}/Ti^{3+} (0.7 V vs. Na^+/Na). This

bi-polar material can act as both cathode and anode material for NIBs by selectively activating the redox couple of Ni^{4+}/Ni^{3+} and Ti^{4+}/Ti^{3+}.

The successful study of P2-phase $Na_xNi_{1/3}Mn_{2/3}O_2$ that have been discussed in Chapter IV shows the possibility to study the 'Ni-Ti'-containing bi-polar $Na_x(Ni^{2+})_{x/2}(Ti^{4+})_{1-x/2}O_2$ ($0.60 \leq x \leq 1$) layered material. To obtain $Na_x(Ni^{2+})_{x/2}(Ti^{4+})_{1-x/2}O_2$ ($0.60 \leq x \leq 1$) samples, two different synthesis techniques: colloidal-assisted synthesis and all solid-state synthesis are developed as shown in **Scheme 5.1**. For the colloidal-assisted synthesis, different $Ni_xMn_yTi_{1-x-y}O_2$ ($0<y<x<1$) nanoparticles are firstly prepared by colloidal synthesis, then followed by electrochemical (blue route) and chemical sodiation (red route) process. On the other hand, $Na_x(Ni^{2+})_{x/2}(Ti^{4+})_{1-x/2}O_2$ samples are synthesized by one-step solid-state reaction as well. By comparing the different techniques in term of phase purity and electrochemical characteristics, solid-state reaction is the most promising preparation route. The further electrochemical tests of the best solid state sample will be discussed as both cathode and anode for NIBs in order to find out the optimal parameters for a symmetric Na-ion battery. Therefore, this Chapter will discuss the results in two parts: 1). The optimization of the synthesis techniques; 2). The further electrochemical tests of the most promising sample obtained from solid-state reaction.

Scheme 5.1. Outline of the procedure to prepare the materials by colloidal and solid-state reactions. Blue route: colloidal synthesis followed by the electrochemical sodiation process. Red route: colloidal synthesis followed by chemical sodiation process. Green route: all solid state reaction.

5.2. Experimental methods

5.2.1 Sample preparation

Two techniques have been employed to obtain $Na_x(Ni^{2+})_{1/3}(Ti^{4+})_{2/3}O_2$ sample: i) colloidal-assisted solid state reaction (blue and red routes in Scheme 5.1) and ii) all solid-state reaction (green route in **Scheme 5.1**).

5.2.2 Colloidal-assisted solid state synthesis

The work was organized according to our synthesis strategy followed for P2-NaNMO sample preparation (see Chapter IV). After obtaining $Ni_xMn_yTi_{1-x-y}O_2$ ($0<y<x<1$) nanoparticles precursor via colloidal synthesis, solid-state sodiation process, in presence of sodium carbonate, was employed. Alternatively to chemical sodiation, an electrochemical sodiation step, as depicted in Scheme 5.1, was also considered since the sodiation process can be achieved easily by cycling in the cell. Therefore, electrochemical sodiation step is achieved by the discharge process of TiO_2 in a half cell against metallic sodium, while the chemical sodiation step is achieved by a solid-state reaction, as previously described. A considerable effort was devoted to develop a synthesis strategy that deliver phase pure NaNTO particles.

The colloidal synthesis of NaNTO precursor was designed according to the work by De Trizio, et al[24]: 'Nb-Doped Colloidal TiO_2 Nanocrystals with Tunable Infrared Absorption'. In this paper, to produce Nb-doped TiO_2 anatase NCs, a mixture of octadecanol (ODAL) (13 mmol), oleic acid (OAc) (1 mmol), and octadecene (ODE) (4 mL) is degassed under vacuum at 120 °C for 1 h in a three-neck round-bottomed flask. In a second flask, a clear solution containing titanium ethoxide (TEO) (1 mmol), ODE (1 mL) and the desired amount of $NbCl_5$ is prepared under inert atmosphere and then heated at 80 °C for 1h. The latter solution is then rapidly injected, via a syringe, into the first reaction flask, and the whole reaction environment is let to cool to room temperature. The temperature is then raised to 290 °C for 60 min to trigger NCs growth. Since the goal of our work is to obtain a Ni-containing TiO_2 phase, the recipe was modified accordingly. Specifically, $NiCl_2$ has been employed instead of $NbCl_5$, as detailed in **Table 5.1**. The obtained sample via colloidal synthesis are named as NTO, NTMO for short.

5.2.3 Carbon coating of the NTO and NMTO particles

NTO and NMTO samples synthesized via colloidal synthesis were surrounded by organic ligands from the solvents which can be decomposed into carbon in the inert atmosphere during pyrolysis.

Therefore, the particles were dried overnight under vacuum at 40 °C and placed in the middle of a tubular furnace under a slightly reducing atmosphere (95% Ar, 5% H2, 50 sccm) and was heated up to 450 °C (5 °C/min), kept at 450°C for 1h and then slowly heated to 650 °C (3 °C/min) and kept at 650°C for 1h. The furnace was then cooled down to room temperature, while still under Ar/H_2 (95/5%) atmosphere. After the pyrolysis, the organic ligands were decomposed into carbon on the surface of the particles. The carbonated sample are named as NTO/C and NMTO/C for short.

Table 5.1 Chemicals and solvents used for the colloidal synthesis and ICP results.

NTO_ first procedure (colloidal synthesis, followed the paper**)**						
Colloidal synthesis	Solvents		Ti solution	Ni solution	Mn solution	Temperature
TiO_2	ODAL+LAC+ ODE		TEO+ODE	---	---	290°C
NTO	Same		Same	$NiCl_2$	---	290°C
NTO_ New procedure						
Colloidal synthesis	Solvents	Ti solution	Ni solution	Mn solution	Temperature	ICP n(Ti):n(Ni):n(Mn)
NTO	5ml ODE+3ml OLAC	$TiCl_4$	Nickel Acetate+OLAM (0.04M)	---	250°C	1:1.13:0
NMTO	Same	Same	Same	Manganese Acetate+OLAM (0.04M)	300°C	0.96:0.036:0.015

5.2.4 All solid-state reaction

Nickel Oxide, Titanium Oxide and sodium carbonate with different stoichiometric ratios were mixed via wet ball-milling for 3h with ethanol. The powder was dried at 80 °C overnight and then calcined under the same pyrolysis protocol used for NaNMO sample (see Chapter IV), as follow: (i) 120 °C for 1h (RT to 120 °C, 5 °C min^{-1}); (ii) 500 °C for 1h (120 °C to 500 °C, 3 °C min^{-1}); (iii) 900 °C for 3h (500 °C to 900 °C, 5°C min^{-1}); (iv) 700 °C for 6h (900 °C to 700 °C, 5 °C min^{-1}). The furnace was then cooled down to room temperature. The obtained sample was named as NaNTO for short. The series of solid-state samples with different Na:Ni:Mn stoichiometric ratios are listed in **Table 5.2**.

Table 5.2. The Solid State synthesis of the NaNTO samples

Solid state	Na_2CO_3 (mmol)	NiO (mmol)	TiO_2 (mmol)
ss-1	1	1	1
ss-2	0.5	0.5	1
ss-3	0.5	0.25	0.75
ss-4	1	1	3
ss-5	1	3	1
ss-6	0.45	0.45	0.55

5.2.5 Electrochemical Measurements

The electrochemical characterization of NTO, NTMO and NaNTO samples was carried out on composite electrodes with the following formulation: 80 wt.% of active material, 10 wt.% of Super P and 10 wt.% of PVdF (see Chapter II). The electrochemical behavior was tested by galvanostatic charge/discharge and cyclic voltammetry (CV) at 50 µV s^{-1}. The cells were charged using a constant current protocol, at different currents (i.e. different current densities: 20, 30, 50 and 100 A g^{-1}). Different voltage range for charge/discharge process were applied for the cathode and anode The cells were disccharged at the same current density used for the corresponding charging step.

5.3 Results and Discussions

5.3.1 $Na_x(Ni^{2+})_{1/3}(Ti^{4+})_{2/3}O_2$ (NaNTO) materials obtained via colloidal-assisted synthesis

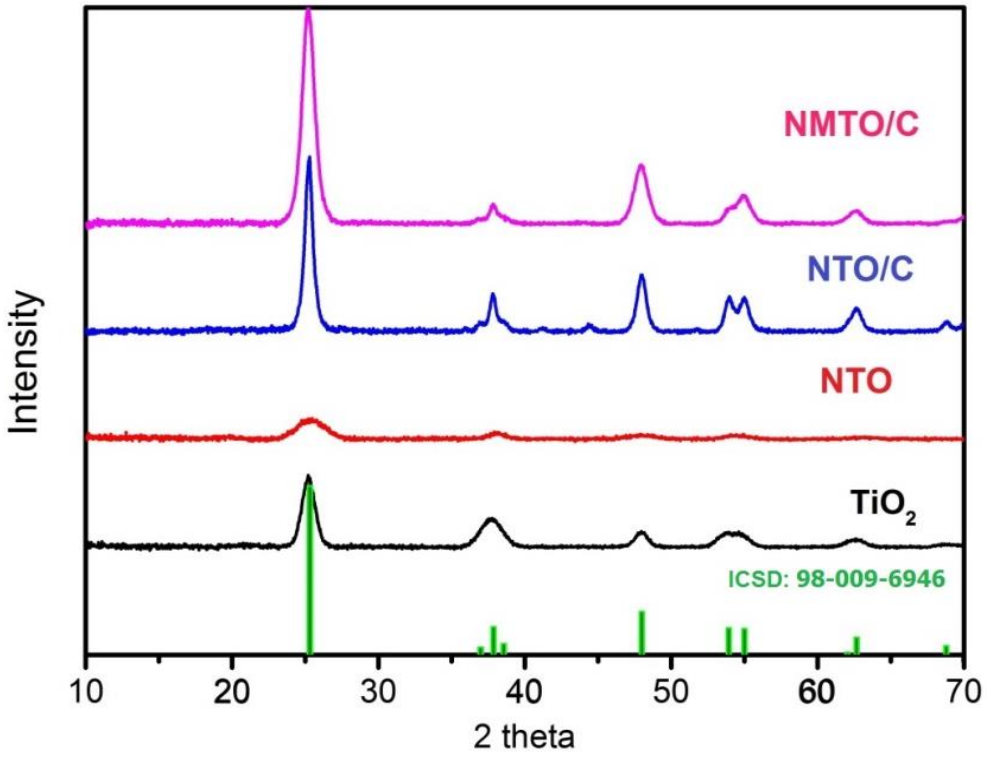

Figure 5.2 . XRD patterns of the TiO_2, NTO and NTMO oxides obtained from colloidal synthesis (new procedure) and the carbon coated samples.

The pure anatase TiO_2 was obtained with the procedure described above in the Experimental methods, however Ni inclusion in TiO_2 NCs by means of $NiCl_2$ solution injections, led to the formation of significant amount of NiO as side product. Moreover, considered the difficult washing process caused by the octadecanol solidification at room temperature, synthesis procedure was modified as listed in Table 5.1 ("new procedure"). In this new procedure, only OLAC and ODE were used. Moreover TEO was replaced with titanium chloride considering lower commercial price of the chemical and higher reactivity at described temperature conditions. **Figure 5.2** shows the XRD patterns of TiO_2, NTO, NMTO and the carbon-coated samples. As shown in Figure 5.2, according to the new procedure, anatase TiO_2 phase was obtained through the colloidal synthesis in the samples of NTO and NMTO as well. The ICP results listed above in Table 5.1 shows the stoichiometric ratio of Ti:Ni:Mn in the sample, which confirms the TiO_2 was successfully doped by Ni and Mn. The XRD patterns of carbon-coated samples can also be readily indexed to the pure anatase TiO_2 with higher intensity of diffraction peaks because of the particles grow during the heating treatment.

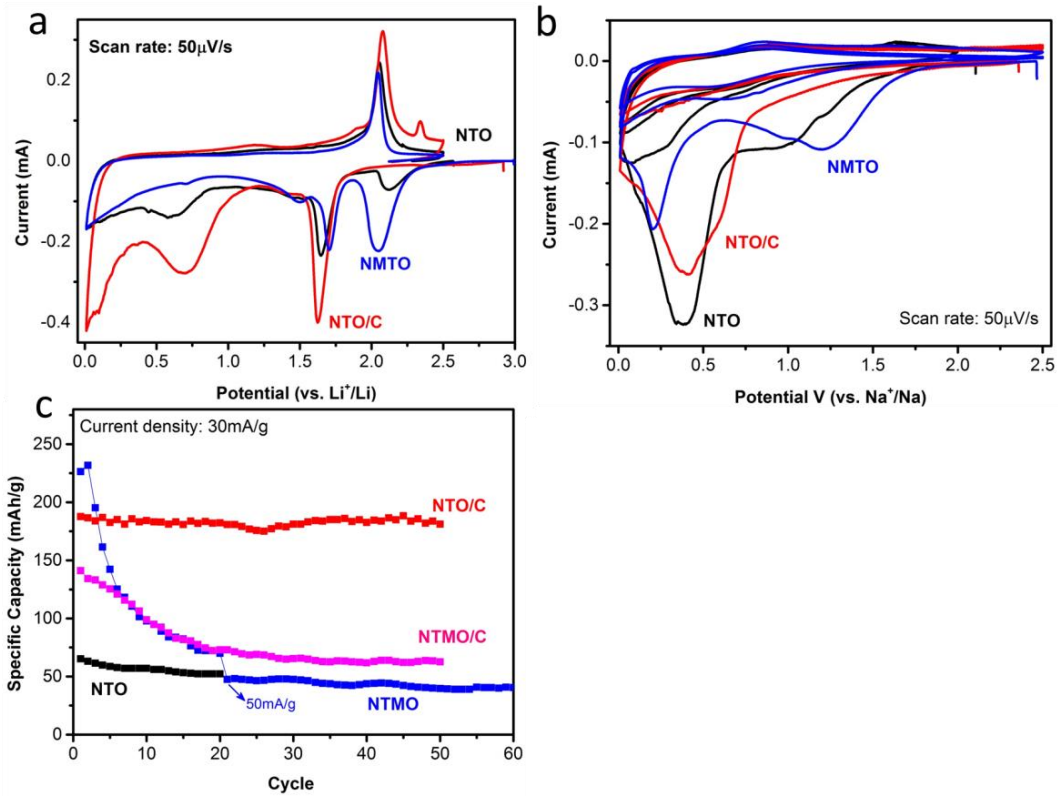

Figure 5.3. Cyclic voltammetry curves of NTO, NTO/C and NMTO for the lithium a) and sodium ion batteries b); c) Cycle performances comparison (discharge capacities) of different oxides as anode material for Li-ion battery.

The following sodiation procedure of the samples were achieved by two techniques: electrochemical sodiation and chemical sodiation process.

Electrochemical sodiation process: NTO, NMTO, NTO/C and NMTO/C samples were used directly as anode materials for both lithium and sodium ion batteries (blue line in Scheme 5.1) considered that the metal oxide is a good choice as anode material for both Li and Na ion batteries, in this case, we could also perform the electrochemical (lithiation) sodiation process. The electrochemical performances are shown below in **Figure 5.3**.

Figure 5.3 shows the cyclic voltammetry curves of NTO, NTO/C and NMTO/C–based anode materials for the Li-ion and Na-ion batteries at a scan rate of 50 μV s-1 in the potential range of 0.01-2.5 V (vs. Na/Na^+). As shown in CV curves (Figure 5.3a), the cathodic peak at 1.69 V and the anodic peak at 2.08 V that shown in all samples, correspond to the reversible phase transition between the tetragonal anatase and orthorhombic, respectively[25]. A cathodic peak appeared around 2.0 V (vs. Li^+/Li) in NMTO sample may correspond to the reduction of Mn^{3+} or Mn^{4+} to Mn^{2+}. The cycle performance of these three samples are shown in Figure 5.3c. The carbon coated sample

NTO/C and NMTO/C deliver higher capacity compared with NTO and NMTO samples may because of the conductive layer helps improve the conductivity of the particles, but the results are not comparable with that reported in the literatures[26, 27]. Mn doping is helpful to improve the performance as shown in Figure 5.3c, but the capacity decays fast which may come from the Jahn-Teller effect of Mn^{3+}. In the case of Na-ion batteries, during the first cathodic scan, the broad peak around 0.9 V is attributed to the decomposition of electrolyte, in another word, it is the irreversible formation of the SEI[28, 29]. The faint peak couple 0.75 V (cathodic)/0.95 V (anodic) in the CV curves becomes pronounced with cycling as shown in Figure 5,3b. This process has been connected to the progressive activation of sodium insertion mechanism[15,29]. However, the Na-ion storage capacity remains low. A parte from a capacity around 200mAh g^{-1} (the best data obtained) delivered during the first cycle, a subsequent fast capacity decay is achieved in just 10 cycles. From the poor electrochemical data so far collected, it can be stated that the electrochemical sodiation (lithiation) process of synthesized NTO and NMTO, via colloidal route, is not a promising approach.

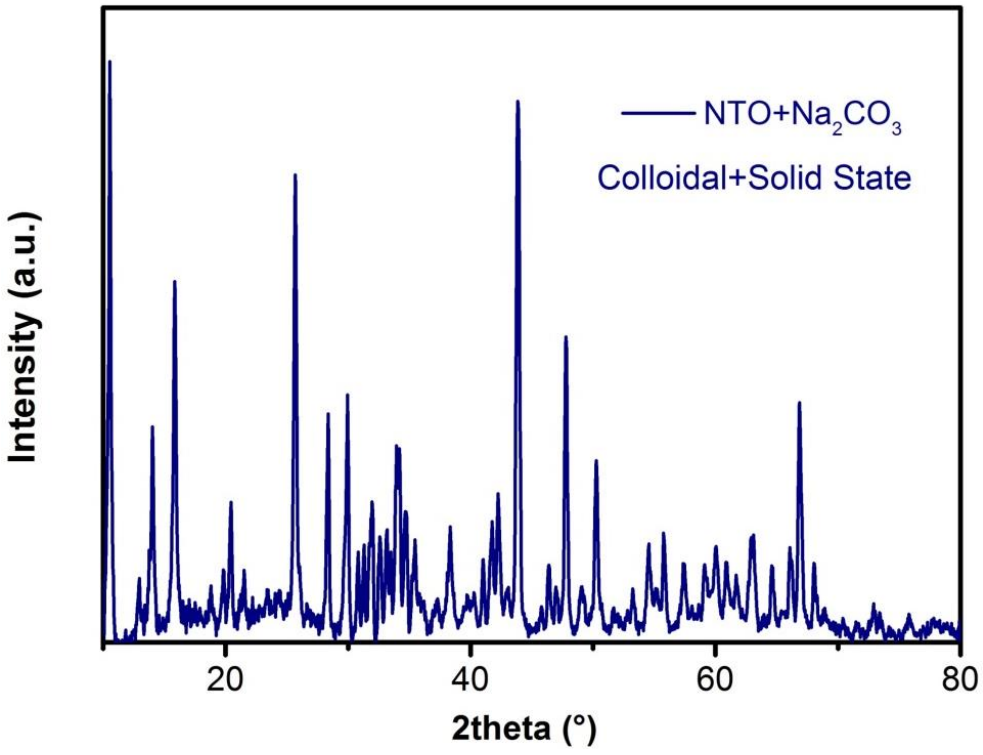

Figure. 5.4. The XRD of the sample obtained from colloidal synthesis after chemical sodiation process.

Chemical sodiation process: The chemical sodiation process of NTO nanoparticles was also taken into consideration, applying solid state reaction. In a typical process Na_2CO_3 was thoroughly mixed to NTO powder (red route in Scheme 5.1). The XRD pattern reported in **Figure 5.4**, referred to

sodiated sample via solid-state process, showed the combination of different phases which contain different $NaTiO_x$ structures and impurities. It seemed that chemical sodiation is not a reliable and reproducible technique to obtain the pure $NaTiO_x$ phase.

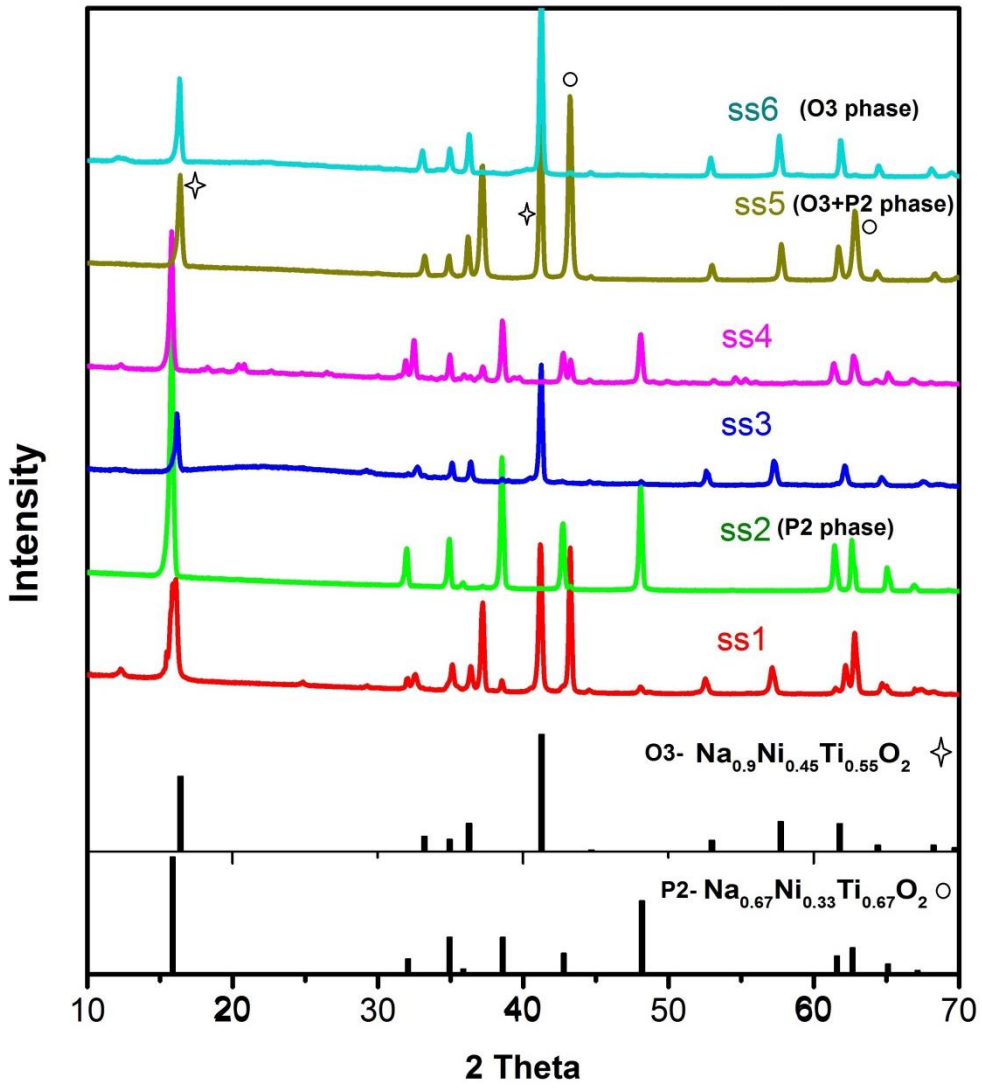

Figure 5.5 The XRD patterns of NaNTO samples obtained from solid state reaction and two typical layered NaNTO phase: P2-$Na_{0.67}Ni_{0.33}Ti_{0.67}O_2$ (references are 98-009-2205) and O3-$Na_{0.9}Ni_{0.45}Ti_{0.55}O_2$ (98-009-2204). P2 and O3 phases in ss5 sample are highlighted with circle and asterisks symbols respectively. Sample ss1-ss5 present the different samples with various stoichiometric ratio of Na, Ni and Ti as shown in the Table 5.2.

Provided the incompatibility between a colloidal step and a solid state sodiation procedure, the whole preparation route was re-designed, and a sole solid-state synthesis has been ultimately

considered. Its description will be provided below, together with experimental outputs analysis.

5.3.2 $Na_x(Ni^{2+})_{1/3(}Ti^{4+})_{2/3}O_2$ (NaNTO) materials obtained via solid-state synthesis

Different precursors ratios were screened in order to achieve the desired phase. Table 5.2 listed the performed solid state reactions for NaNTO samples. We found the synthetic roots ss2, ss5 and ss6 to be more interesting according to their XRD patterns shown in **Figure 5.5**. There are mainly two phases of NaNTO: i) P2-type $N_{a0.67}Ni_{0.33}Ti_{0.67}O_2$ (ss2) and ii) O3-type $N_{a0.9}Ni_{0.45}Ti_{0.55}O_2$ (ss6), which are two typical categories of Na layered oxide according to Delmas classification[30]. In terms of the phase purity, electrodes were prepared only for ss2, ss5 and ss6 samples and the corresponding electrochemical measurements are shown in **Figure 5.6** (1M $NaClO_4$ in PC was used as electrolyte). The ss2 sample was studied as cathode material in the 0.7 – 4.4 V range (red curves) and as anode material in the range of 0.01-2.0 V (blue curves) (Figure 5.6a). The broad redox peak at 3.89 is related to the oxidation of Ni^{2+} to Ni^{4+} while the redox process at 0.78/0.56 V is related to the low potential redox couple $Ti^{4+/3+}$. The overlapping, at potential < 2V, of the first 5 cycles of CV curves shown in Figure 5.6a, suggests that the NaNTO-ss2 sample has better stability when it act as anode material than as cathode in the Na-ion battery. Figure 5.6a' exhibits the initial charge/discharge curves at the current density of 30 mA g^{-1} and insert figures exhibit the cycle stability of the NaNTO-ss2-base electrodes used both as cathode and as anode. The applied voltage range was 1.5-4.4 V (vs. Na^+/Na) for the cathode and 0.01-1.5 V (vs. Na^+/Na) for anode. There is a charge/discharge sloping plateau around 3.6 V and 1.0 V for cathode and a sloping plateau around 0.7 V for the anode. These plateau find correspondence in CV peaks, falling at 3.7 V and 1.0 V in cathode side and 0.56 V in anode side (see Figure 5.6a). The cathode gives higher initial specific capacity (around 130mAh g^{-1}) than the anode (around 75 mAh g^{-1}) since the bigger working potential range which involves two electros process for the cathode and one electro process for the anode, but poorer cycling stability as shown in Figure 5.6a'.

To study the effect of the cycling voltage range on the charge/discharge performance of NaNTO-ss based electrode, and to evaluate how they might affect material stability with cycles, we narrowed the potential range from 0.7-4.4 V to 1.5-4.4 V for the cathode electrode measurements in the NaNTO-ss5 and NaNTO-ss6 sample as shown in Figure 5.6b-6c'. The similar redox peak related to $Ni^{4+/2+}$ and $Ti^{4+/3+}$ are observed in both samples, while the redox peak of the anode part in NaNTO-ss5 sample are much weaker and more irreversible than that of ss2 and ss6, which may result from the lower Ti content. The lower content of Ti in NaNTO-ss5 sample may also be the reason of the

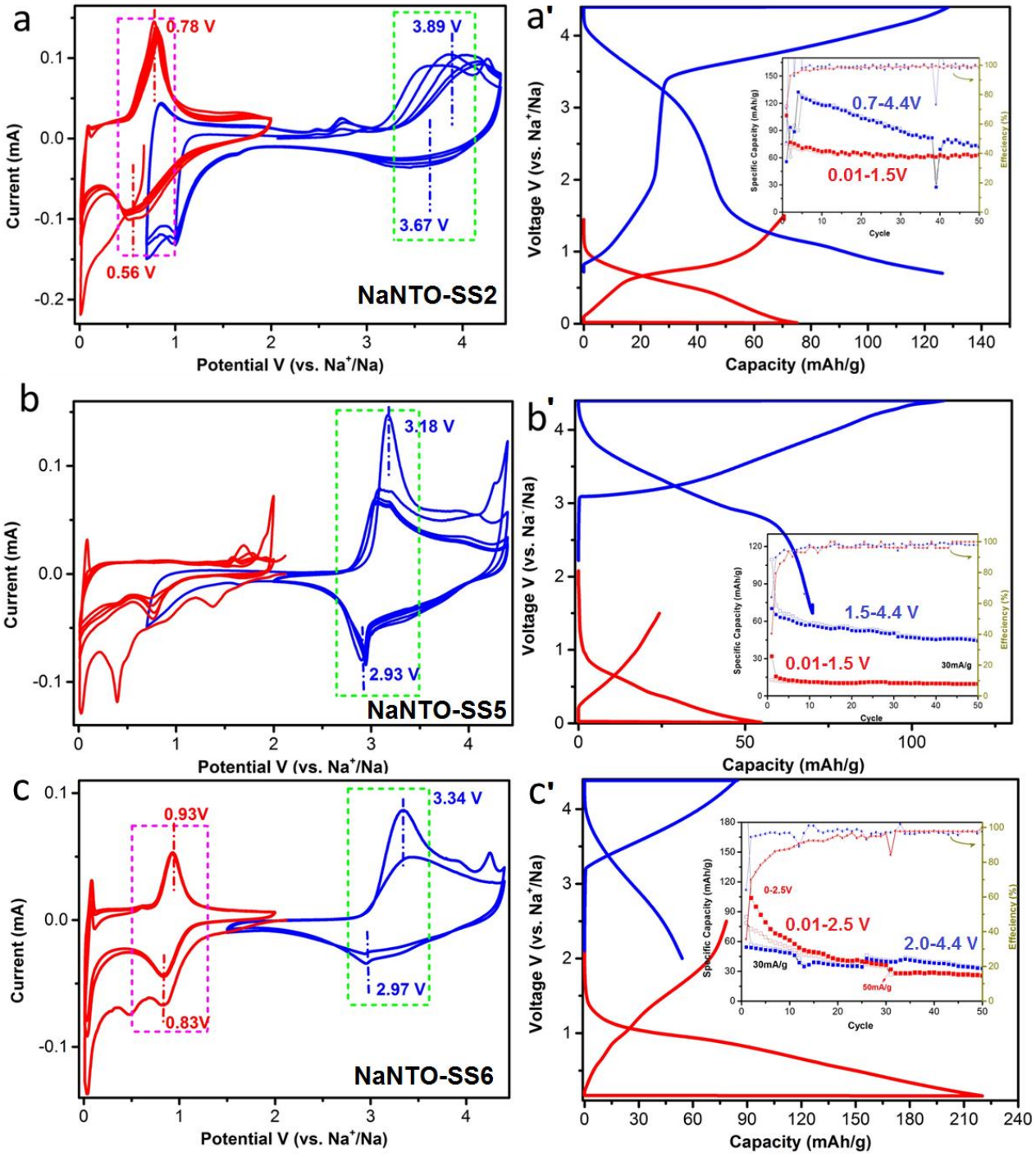

Figure 5.6. The electrochemical performances of the ss2, ss5 and ss6 as anode and cathode materials for the Na ion batteries. a, b and c are the CV curves of ss2, ss5 and ss6 as both cathode and anode materials at 50μV s^{-1}, respectively. a', b' and c' are charge/discharge profiles of ss2, ss5 and ss6 at 30mA/g, respectively. The insert figure shows the cycle performances of the cell on cathode and anode. Blue curves present the cathode and red curves present the anode.

low specific capacity of the sample, in the anode potential range, as showed in Figure 5.6b'. The NaNTO-ss6, which has a O3-type layered structure, shows attractive CV results in both cathode and anode side. However, the O3-structure usually undergoes a series of phase transition connected to slab-gliding of the oxide layer in the crystalline structure[7, 31] during the charge/discharge cycling, which we can tell from the cycle instability in Figure 5.6c'.

So far, two different techniques, colloidal-assisted synthesis and solid-state synthesis, have been tried to obtain $Na_x(Ni^{2+})_{1/3(}Ti^{4+})_{2/3}O_2$ (NaNTO) materials. The P2-type $N_{a0.67}Ni_{0.33}Ti_{0.67}O_2$ (NaNTO-ss2) sample proved to be the optimal result of the solid state reaction in term of phase purity and electrochemical characteristics. This material will be further subjected to electrochemical measurements investigation aimed at to figure out the optimal electrolyte in prospect of the study of full-cell characterization (Chapter VI).

5.3.3 P2-$Na_{0.67}(Ni^{2+})_{0.33}(Ti^{4+})_{0.67}O_2$ (NaNTO-ss2) as electrode material in half cell for Na-ion battery.

Electrode Preparation: The electrochemical characterization of NaNTO-ss2 was carried out on composite electrodes with the following formulation: 80 wt.% of NaNMO, 10 wt.% of conductive carbon SuperP and 10 wt.% of PVdF. The details are described in Chapter II.

Experiments, Results and discussions: The choice of the appropriate liquid electrolytes in the Na-ion battery measurement system is necessary to ensure good electrochemical performance. The most common electrolyte formulations for sodium batteries use either $NaPF_6$ or $NaClO_4$ as salts in carbonate ester solvents, particularly propylene carbonate (PC)[32, 33]. We prepared few different electrolytes in order to find the optimal composition for our Na-ion battery, as listed in **Table 5.3.**

Table 5.3. The different electrolyte used for the Na-ion battery measurements

	Propylene Carbonate (PC)	**PC and 3wt% Ethylene Carbonate (EC)**	**PC and Ethylene Carbonate (PC/EC) (1:1 V/V)**
$NaClO_4$	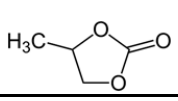	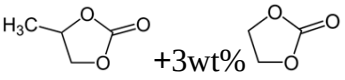	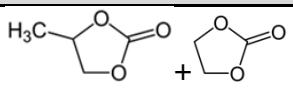

1M $NaClO_4$ in Propylene Carbonate (PC), 1M $NaClO_4$ in PC with 3wt% of Ethylene Carbonate (EC), and 1M $NaClO_4$ in Propylene Carbonate and Ethylene Carbonate (PC/EC 1:1 V/V), were prepared for the measurements considered their significance for the performance as reported in the literatures[14, 34, 35]. The comparison of the electrochemical performance in different electrolytes on both cathode and anode electrodes are shown below. It should be pointed out here that a pre-sodiation process (by directly contact the electrode with Na metal in the presence of the electrolyte (PCEC) to minimize side reactions such as reductive decomposition of SEI), have been done for the anode to see the difference electrochemical behaviors as shown in **Figure 5.7**. From the comparison of the cycle and rate performances, we found out that the electrodes in both cathode and anode side with 1M $NaClO_4$ in PC/EC (1:1 V/V) electrolyte shows the best performance among all the electrolytes that we tried. The electrode exhibited a specific capacity of 121.8 mAh g^{-1}, 95.6 mAh g^{-1} and 82.5 mAh g^{-1} at current density of 30, 50 and 100 A g^{-1} respectively for the anode. At the end of the whole charge/discharge protocol, the electrode with 1M $NaClO_4$ in PC/EC electrolyte delivered, at 30 Ag^{-1} a capacity of 100 mAh g^{-1}.

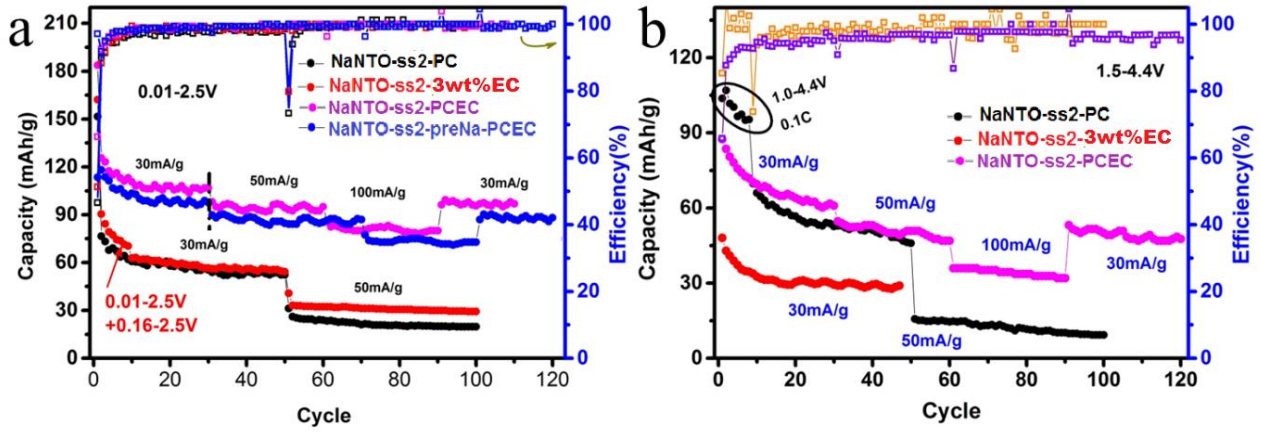

Figure 5.7. The rate and cycle performance of the NaNTO-ss2 sample (obtained via solid state reaction) as cathode a) and anode b) electrodes for the Na-ion half-cell with different electrolytes. (1M $NaClO_4$ in Propylene Carbonate (PC); 1M $NaClO_4$ in PC with 3wt% Ethylene Carbonate (EC) and 1M $NaClO_4$ in Propylene Carbonate and Ethylene Carbonate (PCEC) (1:1 V/V)).

As a result of the pre-sodiation process, the coulombic efficiency of the first cycle increases from 66% to 97%. For the cathode, a specific capacity of 87.5 mAh g^{-1}, 54.8 mAh g^{-1} and 36.0 mAh g^{-1} were delivered at current density of 30, 50 and 100 A g^{-1} respectively.

5.4. Summary

In this chapter, bi-polar layered $Na_xNi_{x/2}Ti_{1-x/2}O_2$ ($0.60 \leq x \leq 1.0$) material was synthesized and acted as bi-functional layered oxide as electrode material for the Na-ion battery. Few works are done to achieve the sample and as electrode material for the Na-ion battery measurements:

a). Two different techniques, colloidal-assisted synthesis and solid-state reaction, have been tried to achieve NaNTO materials. Solid state reaction results a good choice to get the NaNTO materials with pure phase.

a). Different layered $Na_xNi_{x/2}Ti_{1-x/2}O_2$ ($0.60 \leq x \leq 1.0$) sample were synthesized by solid-state reaction, P2-$Na_x(Ni^{2+})_{1/3}(Ti^{4+})_{2/3}O_2$ (NaNTO-ss2) is proved to be the most promising electrode candidate for both cathode and anode material for the Na-ion batteries;

c). By selecting and comparing the different electrolyte solutions, 1M $NaClO_4$ in PC/EC (1:1 V/V) as electrolyte is confirmed to be the best electrolyte for P2-$Na_x(Ni^{2+})_{1/3}(Ti^{4+})_{2/3}O_2$ used as electrode material (both cathode and anode) in Na-ion battery among 1M $NaClO_4$ in PC, 1M $NaClO_4$ in PC with 3wt%EC and 1M $NaClO_4$ in PC/EC (1:1 V/V)). The electrode with 1M $NaClO_4$ in PC/EC electrolyte exhibited a specific capacity of 121.8 mAh g^{-1}, 95.6 mAh g^{-1} and 82.5 mAh g^{-1} for anode and 87.5 mAh g^{-1}, 54.8 mAh g^{-1} and 36.0 mAh g^{-1} for the cathode at current density of 30, 50 and 100 A g^{-1} respectively.

The work we have been discussed in this Chapter is essential for Chapter VI, in which the symmetric full Na-ion battery based on P2-$Na_x(Ni^{2+})_{1/3}(Ti^{4+})_{2/3}O_2$ will be introduced and discussed.

5.5 References

1. Samin, N. K.; Roshidah, R.; Kamarudin, N.; Kamarulzaman, N. In Synthesis and battery studies of sodium cobalt oxides, $NaCoO_2$ cathodes, *Advanced Materials Research*, Trans Tech Publ: **2012**, 185-189.

2. Berthelot, R.; Carlier, D.; Delmas, C., Electrochemical investigation of the P2-Na_xCoO_2 phase diagram. *Nature materials* **2011,** 10, (1), 74.

3. Billaud, J.; Clément, R. J.; Armstrong, A. R.; Canales-Vázquez, J.; Rozier, P.; Grey, C. P.; Bruce, P. G., β-$NaMnO_2$: a high-performance cathode for sodium-ion batteries. *Journal of the American Chemical Society* **2014,** 136, (49), 17243-17248.

4. Ma, X.; Chen, H.; Ceder, G., Electrochemical properties of monoclinic $NaMnO_2$. *Journal of The Electrochemical Society* **2011,** 158, (12), A1307-A1312.

5. Jo, I.-H.; Ryu, H.-S.; Gu, D.-G.; Park, J.-S.; Ahn, I.-S.; Ahn, H.-J.; Nam, T.-H.; Kim, K.-W., The effect of electrolyte on the electrochemical properties of Na/α-$NaMnO_2$ batteries. *Materials Research Bulletin* **2014,** 58, 74-77.

6. Han, M. H.; Gonzalo, E.; Casas-Cabanas, M.; Rojo, T., Structural evolution and electrochemistry of monoclinic $NaNiO_2$ upon the first cycling process. *Journal of Power Sources* **2014,** 258, 266-271.

7. Vassilaras, P.; Ma, X.; Li, X.; Ceder, G., Electrochemical properties of monoclinic $NaNiO_2$. *Journal of The Electrochemical Society* **2013,** 160, (2), A207-A211.

8. Park, K.; Yu, B.-C.; Goodenough, J. B., Electrochemical and Chemical Properties of Na_2NiO_2 as a Cathode Additive for a Rechargeable Sodium Battery. *Chemistry of Materials* **2015,** 27, (19), 6682-6688.

9. Lu, Z.; Dahn, J., In Situ X-Ray Diffraction Study of P 2 $Na_{2/3}[Ni_{1/3}Mn_{2/3}]O_2$. *Journal of The Electrochemical Society* **2001,** 148, (11), A1225-A1229.

10. Lee, D. H.; Xu, J.; Meng, Y. S., An advanced cathode for Na-ion batteries with high rate and excellent structural stability. *Physical Chemistry Chemical Physics* **2013,** 15, (9), 3304-3312.

11. Yabuuchi, N.; Kajiyama, M.; Iwatate, J.; Nishikawa, H.; Hitomi, S.; Okuyama, R.; Usui, R.; Yamada, Y.; Komaba, S., P2-type $Na_x[Fe_{1/2}Mn_{1/2}]O_2$ made from earth-abundant elements for rechargeable Na batteries. *Nature materials* **2012,** 11, (6), 512-517.

12. Buchholz, D.; Moretti, A.; Kloepsch, R.; Nowak, S.; Siozios, V.; Winter, M.; Passerini, S., Toward Na-ion Batteries Synthesis and Characterization of a Novel High Capacity Na Ion Intercalation Material. *Chemistry of Materials* **2013,** 25, (2), 142-148.

13. Kim, D.; Kang, S. H.; Slater, M.; Rood, S.; Vaughey, J. T.; Karan, N.; Balasubramanian, M.; Johnson, C. S., Enabling Sodium Batteries Using Lithium-Substituted Sodium Layered Transition Metal Oxide Cathodes. *Advanced Energy Materials* **2011,** 1, (3), 333-336.

14. Shanmugam, R.; Lai, W., $Na_{2/3}Ni_{1/3}Ti_{2/3}O_2$:"Bi-Functional" electrode materials for Na-ion batteries. *ECS Electrochemistry Letters* **2014,** 3, (4), A23-A25.

15. Su, D.; Dou, S.; Wang, G., Anatase TiO_2: better anode material than amorphous and rutile phases of TiO2 for Na-ion batteries. *Chemistry of Materials* **2015,** 27, (17), 6022-6029.

16. Zhang, Y.; Guo, L.; Yang, S., Three-dimensional spider-web architecture assembled from $Na_2Ti_3O_7$ nanotubes as a high performance anode for a sodium-ion battery. *Chemical Communications* **2014,** 50, (90), 14029-14032.

17. Fielden, R.; Obrovac, M., Low Voltage Sodium Intercalation in $Na_xNi_{x/2}Ti_{1-x/2}O_2$ ($0.5 \leq x \leq 1.0$). *Journal of The Electrochemical Society* **2014,** 161, (6), A1158-A1163.

18. Wang, Y.; Yu, X.; Xu, S.; Bai, J.; Xiao, R.; Hu, Y.-S.; Li, H.; Yang, X.-Q.; Chen, L.; Huang, X., A zero-strain layered metal oxide as the negative electrode for long-life sodium-ion batteries. *Nature communications* **2013,** 4.

19. Yu, H.; Ren, Y.; Xiao, D.; Guo, S.; Zhu, Y.; Qian, Y.; Gu, L.; Zhou, H., An Ultrastable Anode for Long-Life Room-Temperature Sodium-Ion Batteries. *Angewandte Chemie* **2014,** 126, (34), 9109-9115.

20. Wang, Y.; Xiao, R.; Hu, Y.-S.; Avdeev, M.; Chen, L., P2-$Na_{0.6}[Cr_{0.6}Ti_{0.4}]O_2$ cation-disordered electrode for high-rate symmetric rechargeable sodium-ion batteries. *Nature communications* **2015,** 6.

21. Jian, Z.; Zhao, L.; Pan, H.; Hu, Y.-S.; Li, H.; Chen, W.; Chen, L., Carbon coated $Na_3V_2(PO_4)_3$ as novel electrode material for sodium ion batteries. *Electrochemistry Communications* **2012,** 14, (1), 86-89.

22. Plashnitsa, L. S.; Kobayashi, E.; Noguchi, Y.; Okada, S.; Yamaki, J.-i., Performance of NASICON symmetric cell with ionic liquid electrolyte. *Journal of the Electrochemical Society* **2010,** 157, (4), A536-A543.

23. Guo, S.; Yu, H.; Liu, P.; Ren, Y.; Zhang, T.; Chen, M.; Ishida, M.; Zhou, H., High-performance symmetric sodium-ion batteries using a new, bipolar O3-type material, $Na_{0.8}Ni_{0.4}T_{i0.6}O_2$. *Energy & Environmental Science* **2015,** 8, (4), 1237-1244.

24. De Trizio, L.; Buonsanti, R.; Schimpf, A. M.; Llordes, A.; Gamelin, D. R.; Simonutti, R.; Milliron, D. J., Nb-doped colloidal TiO_2 nanocrystals with tunable infrared absorption. *Chemistry of Materials* **2013,** 25, (16), 3383-3390.

25. Wen, Z.; Ci, S.; Mao, S.; Cui, S.; He, Z.; Chen, J., CNT@ TiO_2 nanohybrids for high-performance anode of lithium-ion batteries. *Nanoscale research letters* **2013,** 8, (1), 499.

26. Zhang, Y.; Tang, Y.; Li, W.; Chen, X., Nanostructured TiO_2-Based Anode Materials for High-Performance Rechargeable Lithium-Ion Batteries. *ChemNanoMat* **2016,** 2, (8), 764-775.

27. Mondal, A.; Maiti, S.; Singha, K.; Mahanty, S.; Panda, A. B., TiO_2-rGO nanocomposite hollow spheres: Large scale synthesis and application as an efficient anode material for lithium-ion batteries. *Journal of Materials Chemistry A* **2017**.

28. Xu, Y.; Lotfabad, E. M.; Wang, H.; Farbod, B.; Xu, Z.; Kohandehghan, A.; Mitlin, D., Nanocrystalline anatase TiO_2: a new anode material for rechargeable sodium ion batteries. *Chemical Communications* **2013,** 49, (79), 8973-8975.

29. Wu, L.; Buchholz, D.; Bresser, D.; Chagas, L. G.; Passerini, S., Anatase TiO_2 nanoparticles for high power sodium-ion anodes. *Journal of power sources* **2014,** 251, 379-385.

30. Saadoune, I.; Maazaz, A.; Ménétrier, M.; Delmas, C., On the $Na_xNi_{0.6}Co_{0.4}O_2$ system: physical and electrochemical studies. *Journal of Solid State Chemistry* **1996,** 122, (1), 111-117.

31. Han, M. H.; Gonzalo, E.; Singh, G.; Rojo, T., A comprehensive review of sodium layered oxides: powerful cathodes for Na-ion batteries. *Energy & Environmental Science* **2015,** 8, (1), 81-102.

32. Slater, M. D.; Kim, D.; Lee, E.; Johnson, C. S., Sodium-ion batteries. *Advanced Functional Materials* **2013,** 23, (8), 947-958.

33. Dahbi, M.; Yabuuchi, N.; Kubota, K.; Tokiwa, K.; Komaba, S., Negative electrodes for Na-ion batteries. *Physical Chemistry Chemical Physics* **2014,** 16, (29), 15007-15028.

34. Singh, G.; Aguesse, F.; Otaegui, L.; Goikolea, E.; Gonzalo, E.; Segalini, J.; Rojo, T., Electrochemical performance of NaFe x (Ni 0.5 Ti 0.5) 1− x O 2 (x= 0.2 and x= 0.4) cathode for sodium-ion battery. *Journal of Power Sources* **2015,** 273, 333-339.

35. Yu, H.; Guo, S.; Zhu, Y.; Ishida, M.; Zhou, H., Novel titanium-based O3-type $NaTi_{0.5}Ni_{0.5}O_2$ as a cathode material for sodium ion batteries. *Chemical Communications* **2014,** 50, (4), 457-459.

CHAPTER VI

Investigation of Symmetric Full Battery Based on P2-$Na_{0.67}(Ni^{2+})_{0.33(}Ti^{4+})_{0.67}O_2$

6. 1. Introduction

The vast majority of the sodium ion battery materials that have been studied so far limit their operation to a half-cell configuration, in which the material whose electrochemistry is of interest is tested against metallic sodium. Certainly, this set-up is not representative of a real world sodium-ion battery, for which the substitution of metallic sodium with a safer material, in order to avoid hazard and improve reliability, would be desirable. Added to this, active materials for sodium-ion batteries are being continuatively and extensively studied for more than a decade now and many of them are proven promising cathode and anode compounds ensuring stability and reliability at high currents[1-6] . These findings legitimated the scientific community to investigate full-cell set-ups as well, with the final goal of evaluating the feasibility of a sodium-ion battery prototype cell and putting it into direct comparison with the commercialized lithium-ion counterpart. The recent discovery and optimization of high-voltage cathode materials for NIBs[7-11], indeed contributed in reviving the interest for a full sodium ion battery, contrarily to the downing of sodium ion rechargeable batteries in the 80s. Back then, sodium full-cell performances could not compete with the surpassingly more promising, if not revolutionary, lithium-ion systems[12, 13]. As in any full battery, as currently known, a foremost concern is the precise balancing of cathode and anode materials according to their practical capacities and peculiar behaviors, such as required activation steps and irreversible processes.

Most of the full Na-ion batteries are non-symmetric[14-19] from the recent literatures findings, consisting of layered $NaMO_2$ cathode and carbon/sodium metal anode. This kind of full NIBs system could not satisfy the requirements of long life and safety of large-scale energy storage devices, therefore, the study of new symmetric full cell system is necessary. Currently, there are two types of symmetric full NIBs have been proposed: full vanadium or titanium-based NASICON

structure $Na_3M_2(PO_4)_3$ (M= Ti or V) and Na layered oxides containing two electrochemically active transition metals with redox couples such as Ni^{4+}/Ni^{2+} and Ti^{4+}/Ti^{3+}.

This Chapter will be divided into two sections: 1).A literatures review about full sodium symmetric cell based on NASICON $Na_3M_2(PO_4)_3$ transition metal phosphate and layered oxides materials 2). Discussion of the symmetric NIBs based on layered oxide P2-$Na_x(Ni^{2+})_{1/3}(Ti^{4+})_{2/3}O_2$ as it has been obtained in chapter V in terms of the testing system (two-electrodes and three-electrodes system) and the materials quantity balancing.

6.1.1 Sodium ion full battery based on NASICON-type structure

Na Superionic Conductor (NASICON)-type phosphates $Na_3V_2(PO_4)_3$ (NVP) possesses two red-ox active centers, coinciding with vanadium atoms occupying different crystalline sites. Standard potentials, connected to red-ox couples V^{4+}/V^{3+} and V^{3+}/V^{2+} are, 3.4 and 1.6 V vs Na^+/Na respectively[15].

The cell reactions in the considered symmetric cells can be described as follows[15]:

(Anode) $A_3V^{3+}{}_2(PO_4)_3 + xA^+ + xe^- \leftrightarrow A_{3+x}V^{3+}{}_{2-x}V^{2+}{}_x(PO_4)_3$

(Cathode) $A_3V^{3+}{}_2(PO_4)_3 \leftrightarrow A_{3-x}V^{3+}{}_{2-x}V^{4+}{}_x(PO_4)_3 + xA^+ + xe^-$

(Overall cell reaction) $A_3V^{3+}{}_2(PO_4)_3 \leftrightarrow A_{3+x}V^{3+}{}_{2-x}V^{2+}{}_x(PO_4)_3 + A_{3-x}V^{3+}{}_{2-x}V^{4+}{}_x(PO_4)_3$

The NVP//NVP symmetric cells were firstly fabricated and examined by Plashnitsa, et al[18] in the secondary sodium ion batteries. Based on the Quasi-Open-Circuit Voltage (QOCV) measurements, as shown in **Figure 6.1**a, they optimized the full cell charge cutoff voltage at 1.85 V. To improve the thermal stability of sodium-ion batteries, the room-temperature molten salts $NaBF_4$/1-ethyl-3-methyl imidazolium tetrafluoroborate ($EMIBF_4$) was used as ionic liquid (IL) electrolytes instead of flammable carbonate-type organic electrolyte solvents. The charge and discharge capacities of the NVP symmetric full battery from the first cycle were found to be 102 and 64 mAh g^{-1} respectively as shown in Figure 6.1c. The substitution of the organic electrolytes by the appropriate IL electrolytes in both cases resulted in the decrease of the first discharge capacities. However, the IL-based cells revealed better cyclability and a more stable behavior at elevated temperatures.

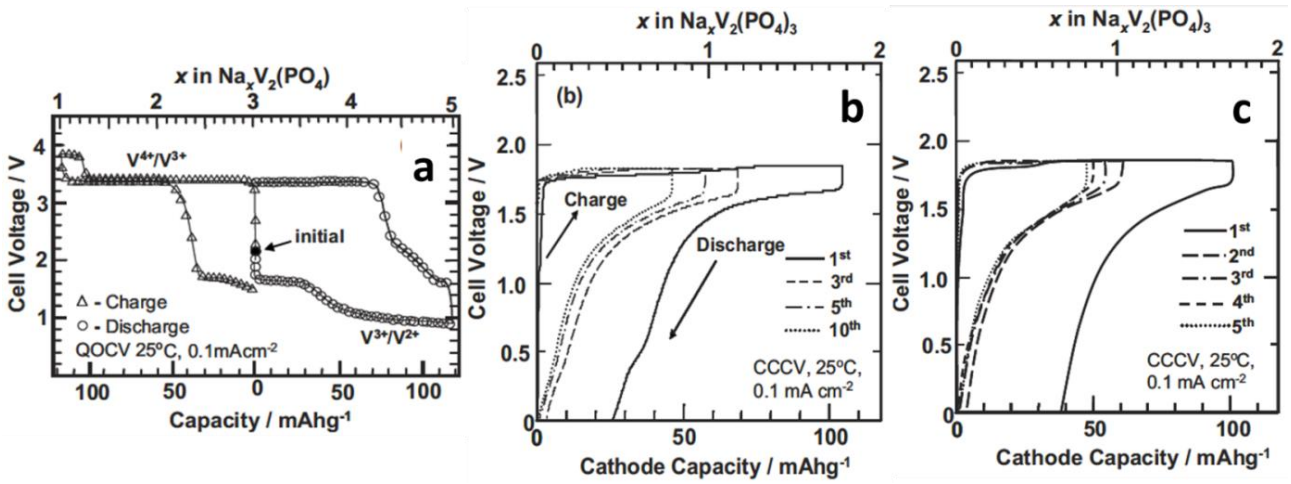

Figure 6.1. [18] a. QOCV curves for the NVP||1M $NaClO_4$/PC||Na cells at room temperature; b. The typical charge/discharge curves obtained at the 1st, 3rd, 5th, and 10th cycles for the NVP||1M $NaClO_4$/PC||NVP symmetrical cells. c. The typical charge/discharge curves obtained at the 1st, 2nd, 3rd, 4th, and 5th cycles for the NVP||0.4 M $NaBF_4$/$EMIBF_4$||NVP symmetrical cells[18].

Yoshinori et al[14] also fabricated the NVP//NASICON//NVP all solid-state symmetric cell. The typical solid-state half-cell was cycled at 2.0-3.6 V and 1.5-2.0 V vs. Na (as shown in **Figure 6.2**a), where the NVP worked as cathode and anode respectively. The voltage of the sodium extractuin from the NVP cathode as flat, at about 3.4V, and was associated with the V^{4+}/V^{3+} redox couple, and the plateau at around 1.6V was associated with the V^{3+}/V^{2+} redox couple and indicated electrochemical insertion of Na^+ ions into the NVP anode. Considered the absolute capacity (mAh of each electrode) balance of the negative/positive electrodes, , as shown in Figure 6.2a, it was suggested that a cathode-to-anode mass ration of 1:3 is appropriate for the construction of symmetric-type cell. Figure 6.2b shows the voltage profiles of the symmetric solid-state cell cycled at 25°C and 1.2μA/cm^2 current density, in the voltage range of 0.01 and 1.9V. The first discharge capacity was about 68mAh g^{-1}, which is around 80% of the first discharge capacity for the liquid NVP//NVP symmetric sodium-ion cell[18] using 1M $NaClO_4$ in PC as the electrolyte and around 58% of the NVP theoretical capacity (117mAh g^{-1}).

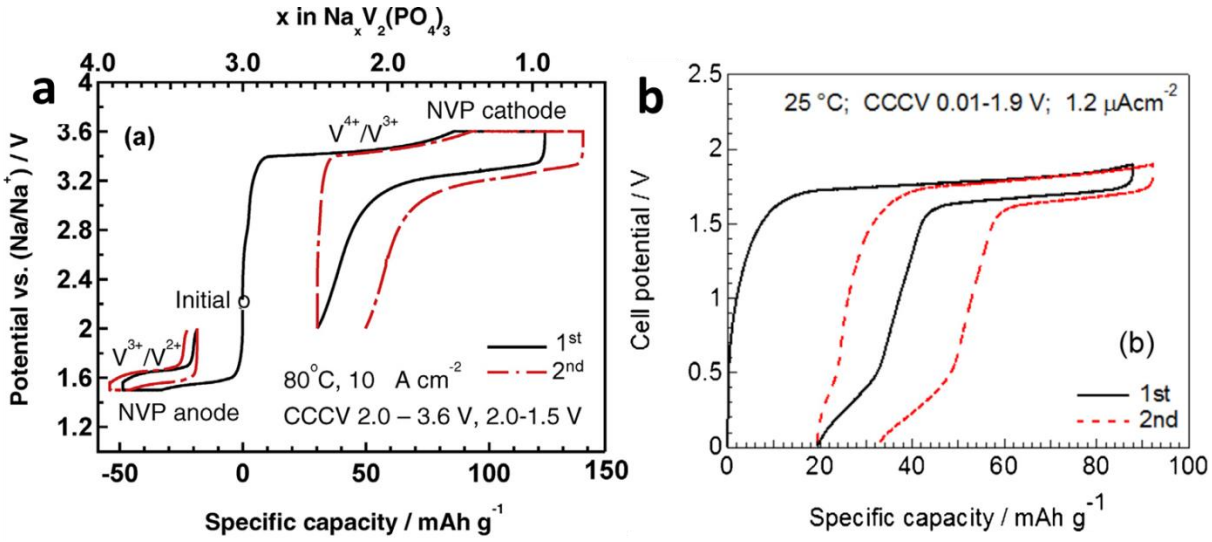

Figure 6.2. a[14]. The charge-discharge profiles of the metallic sodium NVP||NASICON||Na half-cells cycled within 2.0-3-6 and 1.5-2.0 V vs. Na at 10μA and 80°C; b. The charge-discharge profiles of the symmetric NVP||NASICON||NVP solid-state cell tested at 1.2μA cm^{-2} between 0.01 and 1.9V vs. Na at room temperature. The specific capacities are plotted based on the cathode weight[14].

Shuo et al[19] studied the effect of the carbon matrix dimensions on the electrochemical properties of the NVP nanograins for the symmetric sodium-ion batteries. NVP nanograins are dispersed in different carbon matrics from zero-dimensional (0D, Acetylene Carbon), one-dimensional (1D Carbon Nanotubes) to two dimensional (2D Graphite nanospheres) nanostructures. The NVP/AC shows the best electrochemical properties in half cell and the NVP/AC symmetric full battery exhibits excellent performance of 80% capacity retention after 200 cycles at 1C and can tolerate a very high current rate of 10C as shown in **Figure 6.3**.

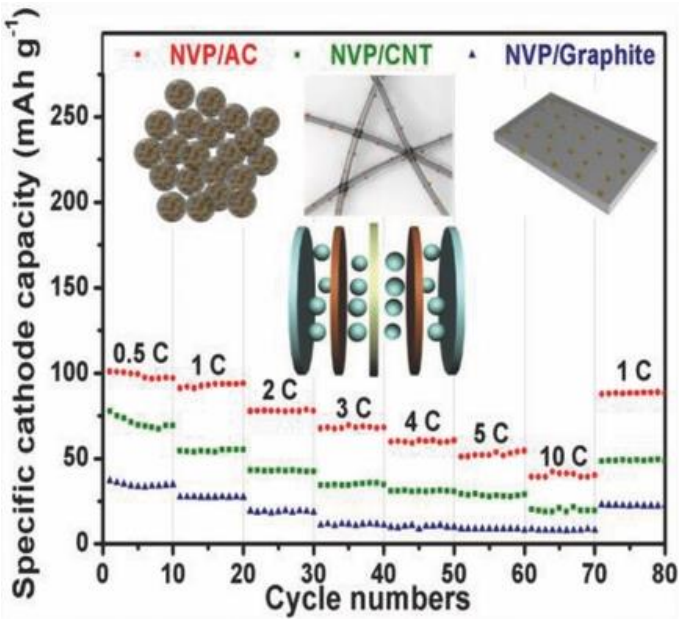

Figure 6.3. The schematic illustrations and the rate performance of $Na_3V_2(PO_4)_3$/AC, $Na_3V_2(PO_4)_3$/CNT and $Na_3V_2(PO_4)_3$ /graphite at various current rates from 0.5 C to 1 C[19].

The ca. 1.8V voltage differences observed between V(IV)/V(III) and V(III)/V(II) redox couples within $Na_3V_2(PO_4)_3$ opened the possibility to the use even different transition metals (such as in the case of $Na_3Ti_2(PO_4)_3$) for the construction of a symmetric sodium-ion full cell. P. Senguttuvan et al[17] have validated the concept of full-Ti-based sodium ion cells through the assembly of symmetric cells involving $Na_3Ti_2(PO_4)_3$ (NTP) operating at an average potential of 1.7V. V^{4+}/V^{3+} and V^{3+}/V^{2+} redox couples were effectively replaced by Ti^{4+}/Ti^{3+} and Ti^{3+}/Ti^{2+} couples, operating at a voltage of 2.1 and 0.4 V vs Na^+/Na respectively. Experimental results agreed well also with theoretical investigation of operational potentials based on ab-initio calculation method originally proposed by Ceder et al[20]. **Figure 6.4**a shows the potential versus composition profile for NTP half-cell in galvanostatic model at C/25 rate between 2.5 and 0V. The voltage window of the symmetric cell was controlled by the positive electrode cutoff voltage as 2.6-1.9 V vs. Na^+/Na, and the potential profile for the three-electrode Swagelok configuration is shown in Figure 6.4b.

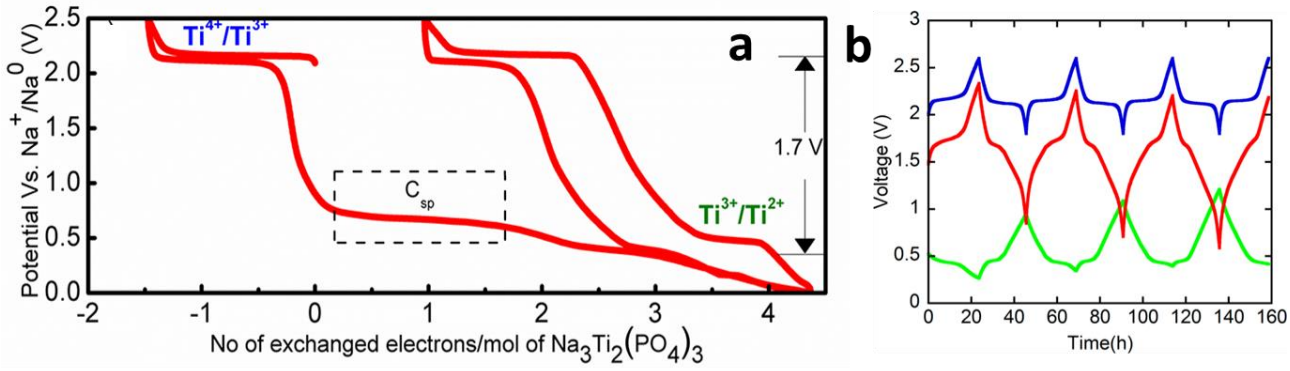

Figure 6.4.[17] (a) Galvanostatic cycling of $Na_3Ti_2(PO_4)_3$ vs Na between 2.5 and 0 V for the first harge/discharge and subsequent charge/ discharge. (b) Potential profile as a function of time for symmetric $Na_3Ti_2(PO_4)_3||NaClO_4$ in $PC||Na_3Ti_2(PO_4)_3$ cells with a three electrode configuration cycled at C/20 at room temperature.

6.1.2 Full battery based on layered oxide

Apart from the NASICON structure-type based symmetric full battery, the bipolar materials with layered structure, containing two electrochemically active transition metals with redox couples such as Ni^{4+}/Ni^{2+} and Ti^{4+}/Ti^{3+}, are also very attractive and promising for the implementation in Na-ion symmetric batteries.

Typical Na layered oxides can be defined as P2- (prismatic) and O3- (octahedral) phases based on the surrounding Na^+ environment and the number of unique oxide layer packing[21]. Shaohua Guo et al[16] designed and synthesized the O3-type $Na_{0.8}Ni_{0.4}Ti_{0.6}O_2$ material, the 'golden pair' of nickel and titanium not only greatly stabilize each other in the electrochemical sodiation/de-sodiation process, but also exhibit the unique double redox couples of Ni^{4+}/Ni^{2+} (3.5V vs. Na+/Na) and Ti^{4+}/Ti^{3+} (0.7V vs. Na+/Na). The proposed symmetric NIB, as shown in **Figure 6.5**, exhibits a reversible discharge capacity of 85 mAh g^{-1} with the average voltage of 2.8V and presents a superior long life exceeding 150 cycles with capacity retention of 75%. Two distinct redox peaks of around 3.65/3.5 V (Ni^{4+}/Ni^{2+}) and 0.95/0.7 V (Ti^{4+}/Ti^{3+}) can be observed in Figure 6.5c, with a potential difference between the two redox couples.

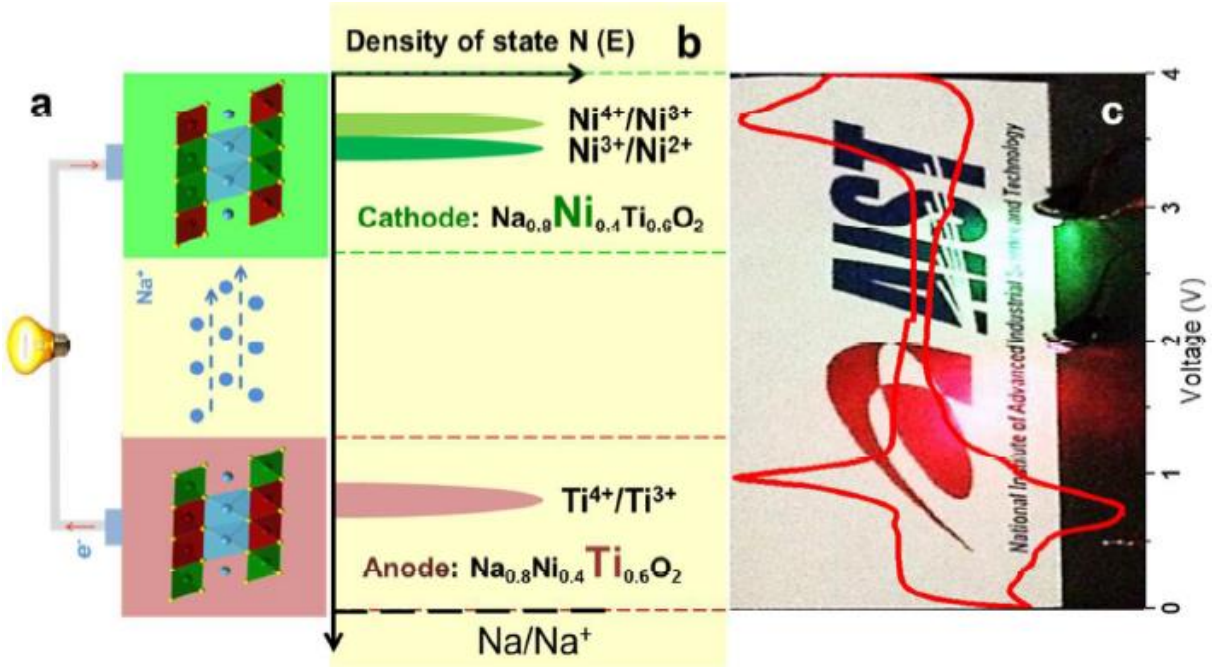

Figure 6.5.[16] Schematic illustration of designing the symmetric NIBs via the two redox couples of nickel and titanium in the layered materials $Na_{0.8}Ni_{0.4}Ti_{0.6}O_2$. **(a)** A diagram of the proposed symmetric cell based on O3-type $Na_{0.8}Ni_{0.4}Ti_{0.6}O_2$. **(b)** schematic of energy *vs.* density of states plot, showing the relative positions of the Fermi energy level of Ni^{4+}/Ni^{2+} (Ni^{4+}/Ni^{3+} and Ni^{3+}/Ni^{2+}) and Ti^{4+}/Ti^{3+} redox couples for O3-type $Na_{0.8}Ni_{0.4}Ti_{0.6}O_2$. **(c)** The CV curve of $Na_{0.8}Ni_{0.4}Ti_{0.6}O_2$/Na half-cell in the whole voltage range of 0-4 V *vs.* Na+/Na, and the background shows the lighted LED bulbs driven up by the designed bipolar $Na_{0.8}Ni_{0.4}Ti_{0.6}O_2$-based symmetric cells.

In case of the P2-type structure, Yuesheng Wang et al. realized that because of the strong Na^+-Na^+ interaction in the alkali metal layer and charge ordering in the transition metal layer, most P2-type layered oxides exhibit Na^+/vacancy-ordered superstructures, which supposed to result in rapid capacity-fading during cycling. They found the transition metal ordering is mainly controlled by the difference in the ionic radii of M1 and M2 in P2 $Na_x[M1,M2]O_2$-layered oxide. Through selecting transition metals as Cr^{3+} and Ti^{4+} which shown similar ionic radii (0.615 and 0.605 Å, respectively[22]) but a substantial difference in redox potential, they[23] designed a P2-$Na_{0.6}[Cr_{0.6}Ti_{0.4}]O_2$-layered oxide, which is highly Cr/Ti and Na^+/vacancy-disordered at any sodium content and over wide range of temperature. The full cell delivers an average operating voltage plateau at around 2.53 V and extraordinary rate and superior cycling performance. Even at a very high rate of 12C, the capacity retention is 75% of that at 1C rate, as shown in **Figure 6.6**. It was demonstrated that this cation-disordered material can function as both positive and negative

electrodes with average operation voltages of 3.5 and 0.8 V, corresponding to the redox couples of Cr^{3+}/Cr^{4+} and Ti^{3+}/Ti^{4+}, respectively. Titanium substitution with manganese in layered oxide chemical formula, leads to the compound P2-$Na_{0.5}Ni_{0.25}Mn_{0.75}O_2$ with dual-electrode characteristic[24]. Contrarily to what has been observed for other manganese containing layered structures. $Na_{0.67}Mn_{0.67}Ni_{0.33}O_2$ and $Na_{0.78}Mn_{0.23}Ni_{0.69}O_2$, in which Mn^{4+} remains substantially inert due to potential values above 2.5V vs. Na^+/Na, Mn changes its oxidation state when P2-$Na_{0.5}Ni_{0.25}Mn_{0.75}O_2$ is cycled between 1.5 V and 2.6 V vs. Na^+/Na. the dual-electrode behavior is imputable to $Ni^{2+/4+}$ redox couple (operating at 3.72/3.51V vs. Na^+/Na). Despite the discrepancies between reversible capacities extracted from half-cell configuration (75 vs 100 mAh g^{-1}), mass ratio between reversible capacities extracted from half-cell fabrication was kept equal to 1. Based on this configuration the cell ensured a long cycle ability extended over 100 cycles with a capacity retention of 90% after 50 cycles and an output voltage of 2.0V.

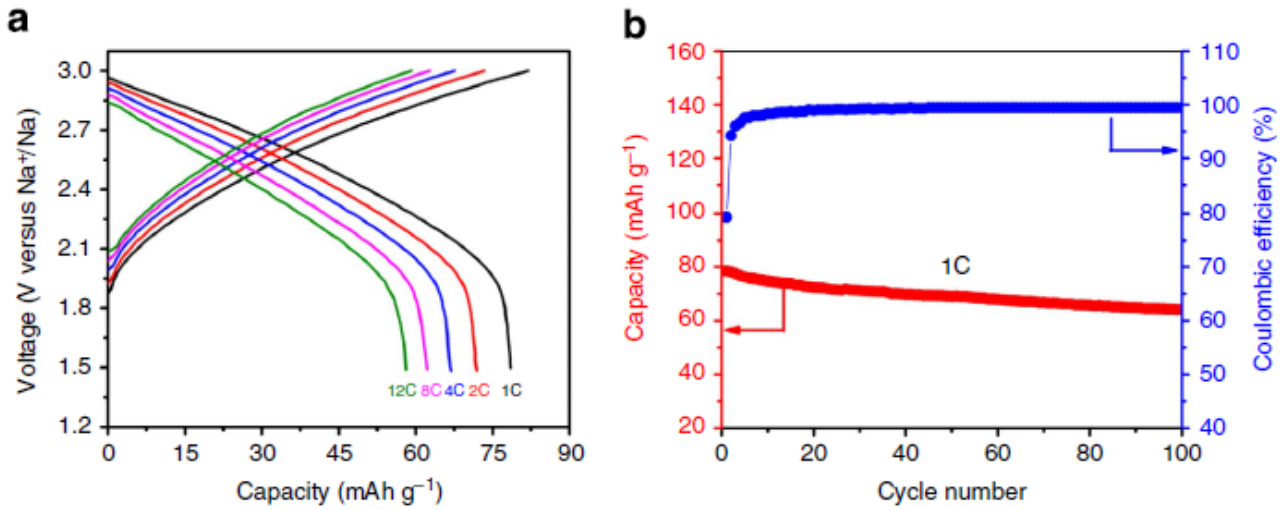

Figure 6.6.[23] Full-cell performance of P2-$Na_{0.6}[Cr_{0.6}Ti_{0.4}]O_2$ as both positive and negative electrodes in the $NaPF_6$-based electrolyte. (a) Dishcharge profiles of $Na_{0.6}[Cr_{0.6}Ti_{0.4}]O_2$/ $Na_{0.6}[Cr_{0.6}Ti_{0.4}]O_2$ sodium-ion full cella t various rates. (b) The capacity and Coulombic efficiency versus cycle number of the full cell at 1C rate. The capacity was calculated based on the mass of the negative electrodes.

Despite the fact that the expected operating potentials of the symmetric system are low and could provide only moderate energy density, the application of the symmetric batteries could definitely involve several advantages, such as improved safety, long preserve lifetime and ability of charging

in either direction. Also from the technical point of view, the assembly of symmetric cell could simplify the fabrication process and significantly reduce the manufacturing costs.

6.2. P2-$Na_x(Ni^{2+})_{1/3}(Ti^{4+})_{2/3}O_2$ (NaNTO-ss2) as electrode material in symmetric full Na-ion battery.

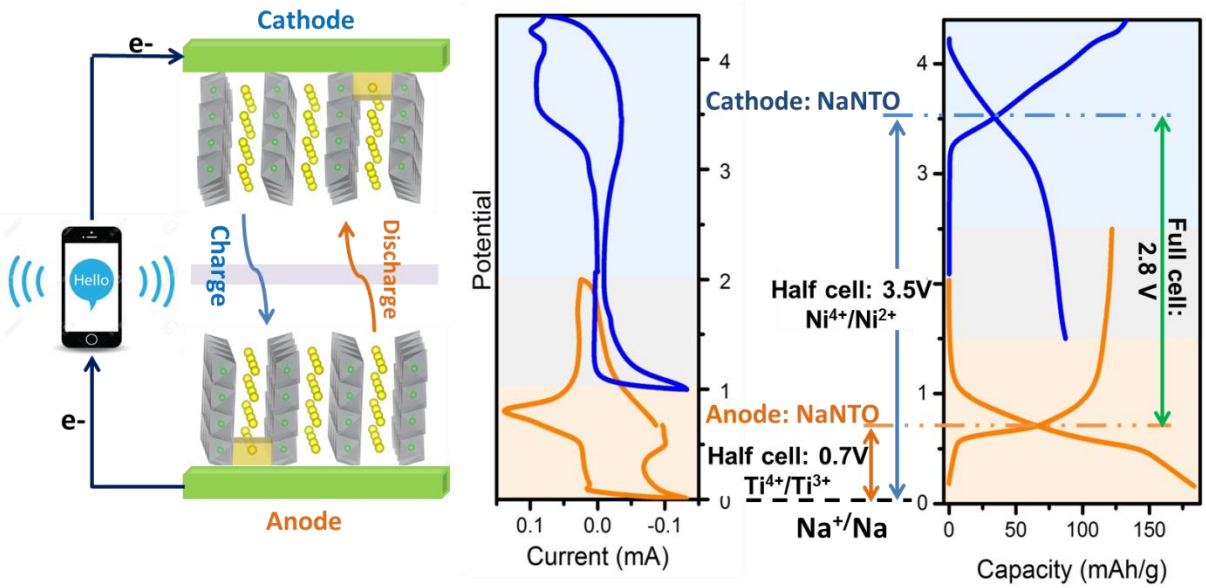

Figure 6.7. Schematic illustration of symmetric sodium-ion cell design. The two redox couples related to nickel ($Ni^{2+/4+}$) and titanium ($Ti^{3+/4+}$) of layered P2-$Na_{0.67}Ni_{0.33}Ti_{0.67}O_2$, are plotted in CV and galvanostatic curve plots.

$Na_xNi_{1/3}Ti_{2/3}O_2$-based material contains two electrochemical active transition metals with high redox couple of Ni^{4+}/Ni^{2+} (3.5V) and low redox couple of Ti^{4+}/Ti^{3+} (0.7V), which make the material suitable for being used both as anode and cathode material. In Chapter V, P2-$Na_{0.67}(Ni^{2+})_{0.33}(Ti^{4+})_{0.67}O_2$ (NaNTO-ss2) was prepared employing an optimized solid-state approach. After an accurate electrolyte solution selection, the material was tested both on cathode and anode sides, in half-cell configuration, as shown in **Figure 6.7**. The broad redox peak at 3.89 V shown in the CV curves for cathode is related to the oxidation of Ni^{2+} to Ni^{4+} while the redox process at 0.78/0.56 V for the anode is related to the low potential redox couple Ti^{4+}/Ti^{3+}. These redox peaks find correspondences in the charge/discharge sloping plateau, around 3.6 V and 1.0 V for cathode

and a sloping plateau around 0.7 V for the anode. This motivated us to assemble the symmetric Na-ion full cell. This chapter will discuss the electrochemical performance of the symmetric Na-ion battery based on this material.

6.2.1 Experimental methods

Coin-type 2032 (two-electrodes system) and Swagelok-type electrochemical cell (three-electrodes system) were carried out for the symmetric Na-ion full cell electrochemical performance study in this Chapter.

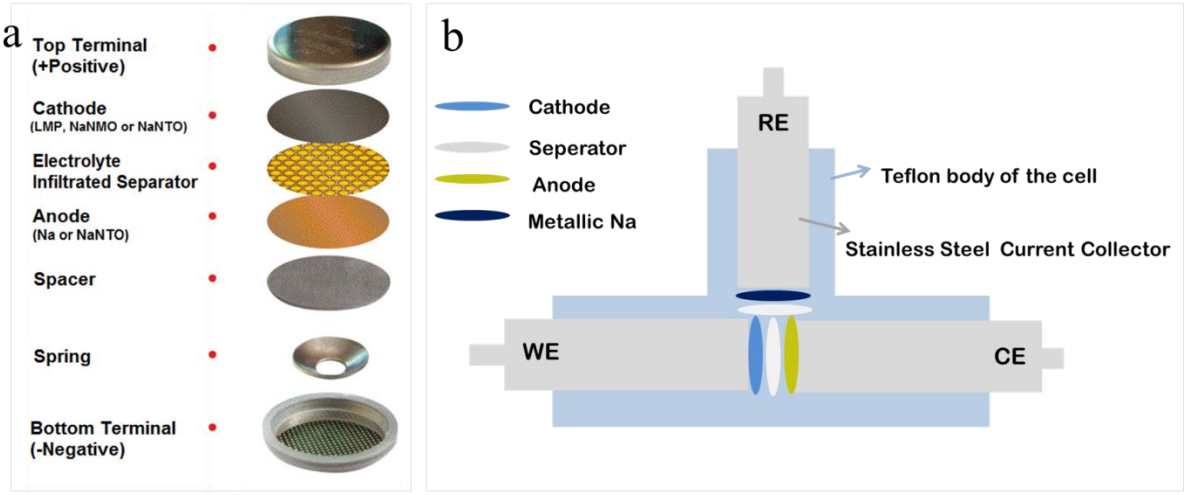

Figure 6.8. Schematic Representation of a. two-electrodes system (c. "coin-type") and b. three-electrodes system (d. "Swagelok-type" electrochemical cell).

Coin-type (2032) Electrochemical Cells: The diameter of the circular electrode for the coin cell is 15mm. In the coin cell, NaNTO sample is employed as both cathode and anode as shown in **Figure 6.8**a. The electrodes have been pre-cycled in coin cell vs. Na before assembling into the full cell. NaNTO electrodes are removed from the half-cell after the first cycle by disassembling the cell. A dried glass fiber membrane (Whatman GF/D) was used as separator wetted with electrolyte solution (200µL).

Swagelok-type Electrochemical Cell: In the Swagelok-type cell, the diameter of the circular electrodes is 12mm. The electrodes have been pre-cycled in coin cell vs. Na before assembling into the full cell. NaNTO electrodes are removed from the half-cell after the first cycle by disassembling the cell, use them as both working and counter electrodes (Figure 6.8b) in the Swagelok cell,

metallic Na disk is employed as reference electrode, A dried glass fiber membrane (Whatman GF/D) was used as separator wetted with electrolyte solution (250µL).

All the cells are assembled and sealed in an argon filled glove box (see Chapter II).

Electrochemical Measurements: The electrochemical behavior was tested by galvanostatic charge/discharge technique. The cells were charged using a constant current protocol, at different currents (i.e. different current densities: 5, 10, 20, 30, 50, 100 and 200 A g^{-1}) up to 4.4V for the full cell. The cells were then discharged at the same current density used for the corresponding charging step.

6.2.2. Results and Discussions

Two-electrode system

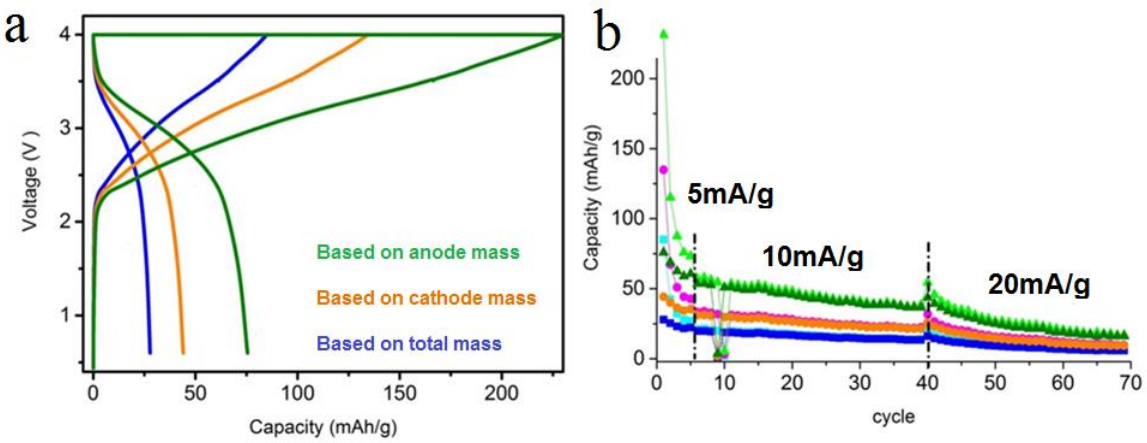

Figure 6.9. Electrochemical performances of symmetric Na-ion full cell based on P2-NaNTO sample tested in a coin cell. a). Initial charge/discharge profiles of the full cell; b). The cycle performance of the full cell under the current density of 5, 10 and 20mA/g. The obtained capacity are based on the mass of anode, cathode and the total.

The full cell is firstly assembled and studied in coin cell (two-electrodes system), in which both working and counter electrode were based on P2-NaNTO, as shown in Figure 6.8a. To reduce the negative effect of the first cycle irreversible capacity, the electrodes have been pre-cycled in half cell vs. Na before assembling into the full cell. The results, in term of capacity, are calculated based on the anode, cathode or the total electrodes mass as shown in **Figure 6.9**a and 9b. The symmetric full cell delivers an average operating potential of ~2.7 V, the initial capacity is around 75 mAh g^{-1}

based on the anode mass. From the charge/discharge profile of Figure 6.9a, a considerable irreversible capacity is still present in the first discharge process of the full cell, which may derived from three possible reasons: 1). The SEI formation (during the pre-cycle) on both electrodes were damaged during the disassembly of the half cell. A new SEI need to be created in the full cell; 2). a not optimized working potential range. The potential window in which the full cell (coin type) was tested could be limited only by the potential difference between the working electrode (E_{WE}) and the counter electrodes (E_{CE}), which can be presented by the equation $E_{cell} = E_{WE} - E_{CE}$, therefore, the optimal working potential range of the full cell could not be guaranteed ; 3). The inadequate use of either the cathode material or the anode material.

The working conditions of both electrodes in the two-electrodes battery testing system are blind since only the results of the whole system could be detected the results of the whole system, which is difficult to modify and optimize the parameters for the full cell. It motivated us to build the three-electrodes testing system, as introduced in Chapter II, to look into the cell and detect results from both working electrode and counter electrode.

Three-electrodes system

Figure 6.10 shows the electrochemical performances of the full cell achieved from a three-electrodes Swagelok cell (Figure 6.8b). The potential will remain constant and equal to its open-circuit value during the electrochemical test. A reliable and un-biased WE-RE voltage difference reading, can be thus achieved. In this case, the RE is metallic Na disk. The current is passed between the WE and CE (or the auxiliary electrode). The WE and CE are P2-NaNTO sample in this case.

In this full cell system, WE and CE potential can be detected separately. By monitoring and modifying the potential ranges of WE and CE, the charge/discharge curves were obtained as shown in Figure 6.10a. The red, blue and green curve present the charge/discharge curves of the full cell, the cathode and the anode, respectively. During charge process, the sodiation and desodiation process is synchronous happening at the WE and CE, respectively. Therefore, it is essential to take full advantage of both the cathode and anode in the full cell. As described before, the oxidation of Ni^{2+} to Ni^{4+} in the cathode happens around 3.8 V (vs. Na^+/Na) while the reduction of Ti^{4+} to Ti^{3+} at around 0.8 V (vs. Na^+/Na) for the anode. Therefore, the initial discharge profile that shown in Figure 6.10a is inadequate at the first few cycles since the anode just reaches 0.7 V (the reduction of Ti^{4+} to Ti^{3+} just starts) when cathode reaches the cut-off voltage 4.4 V. It means the sodiation

process of the full cell is limited by the cathode. The sodiation/desodiation profiles became more balanced after the cutoff potential potentials are increased from 4.4 to 4.5 V, on the cathode side, and from 1.2 to1.5 V on the anode. Differences in overall potential output (red-curve in Figure 6.10a) can be appreciated starting from the 6th cycle, and they actualize in a well-defined potential plateau appearing above 3.5 V. Figure 6.10b exhibited the charge/discharge curves of the cathode, anode and the full cell based on the mass of total, cathode and anode. The irreversible capacity is decreased after the modification of the potential limitations on both WE and CE. However, the capacity dropped fast during cycling as shown in Figure 6.10c, which may be caused by the high cut-off potential (4.5 V vs. Na^+/Na) we modified for the cathode. The plateaux appears at 4.5 V may be caused by the oxidation of the electrolyte.

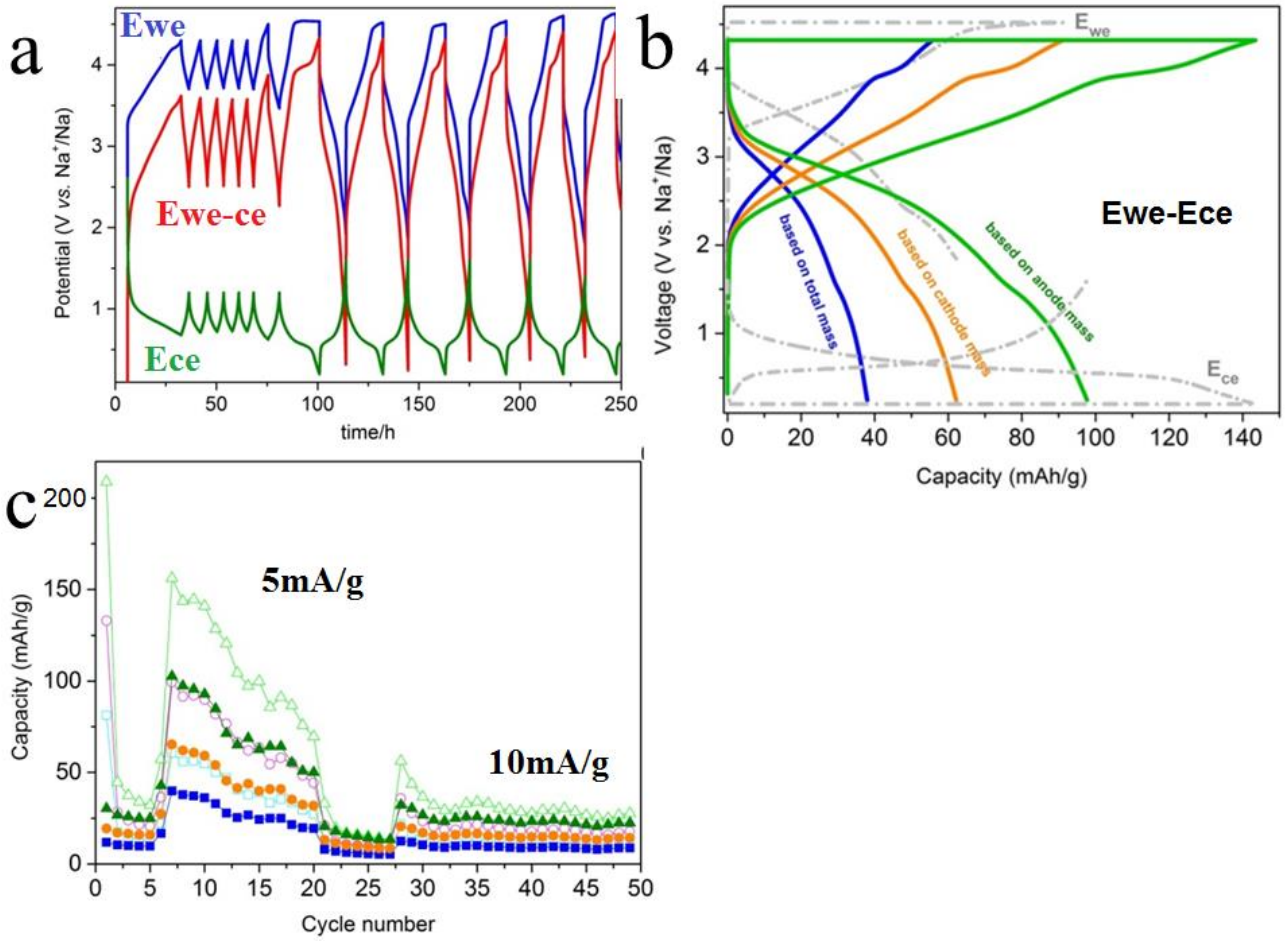

Figure 6.10. The electrochemical performances of symmetric Na-ion full cell based on P2-NaNTO sample tested in Swagelok cell. a). Charge/discharge profiles of the working electrode (WE), counter electrode (CE) and the full cell; b). the initial charge/discharge curves of the cell on WE, CE and full cell; c). the cycle performance under different current density. the capacity obtained based on the mass of anode, cathode and the total.

In order to keep the cathode in the safe potential window (< 4.5 V), we also tried to increase the capacity that can be delivered from the cathode to compensate that from the anode, which means we could increase the mass loading of the cathode instead of increase the cut-off potential. It is necessary then to find out the proper mass ratio between cathode and anode.

Optimize the mass ratio between cathode and anode

The sodiation/desodiation process in the full cell is based on the Na^+ intercalation/deintercalation ability of the cathode and anode. To maximize the energy density of the full cell, an equilibrium mass ratio value should be achieved between two host electrodes. It can be represented by the equation :

$$r = \frac{m_+}{m_-} = \frac{\Delta y \cdot C_-}{\Delta x \cdot C_+}$$

In the equation, r is the mass loading ratio between cathode and anode; Δx and Δy are the mole stoichiometry of the Na^+ that intercalated into the cathode and the anode, respectively; $C-$ and $C+$ are the theoretical capacities of the material as cathode and anode respectively. In another word, it is the ratio of the material capacity at their sodiation state.

According to the study about P2-NaNTO material, collected in Chapter V, where potential range of used for testing cathode and anode were 1.5-4.4V and 0.01-2.5 V respectively, the calculated mass ratio value between cathode and anode is about 1.4. However, for a real full cell, the ratio changes according to the real specific capacities of each side, which depend on the operation potential range of both cathode and anode. Apart from the potential range, the irreversible capacities is also another issue that we need to take into consideration when the full cell is designed. Based on that, different ratios have been discussed considering the irreversible capacity and the tunable potential range.

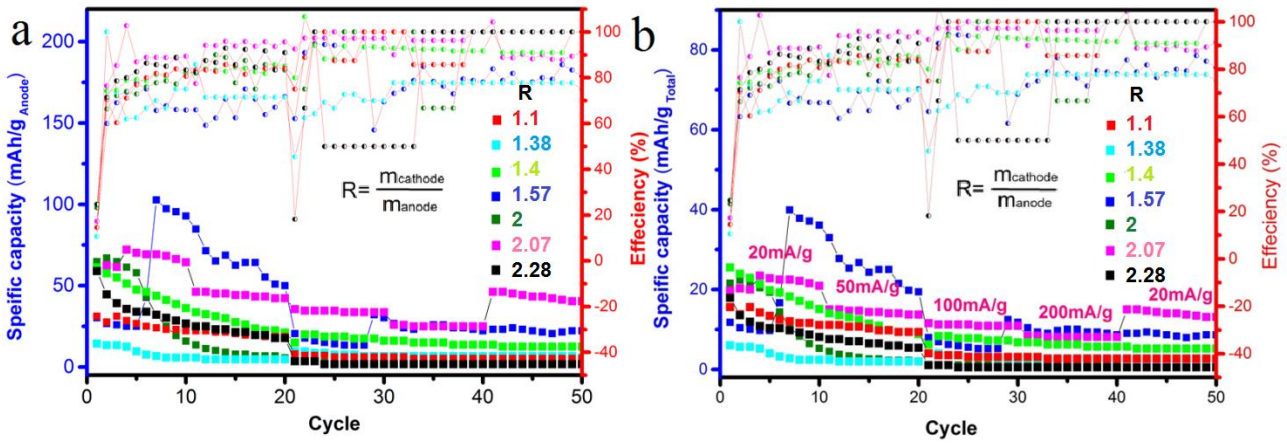

Figure 6.11. The rate performances of the Swagelok-type full cell base on P2-NaNTO with different mass ratio between cathode and anode.

Figure 6.11 presents the electrochemical performance of the full cell with different ratios. We calculated the specific capacity based on the mass of the anode (Figure 6.11a) and the total mass on both cathode and anode (Figure 6.11b) at different current density, 20, 50, 100, 200 and back to 20 mA/g. The best mass ratio between cathode and anode is 2.07 after the comparison as shown in Figure 6.11. The blue, orange and green curves in **Figure 6.12**a presents the charge/discharge profiles of the cathode, anode and the full cell respectively, in the Swagelok cell. The voltage optimization process is done in the first few cycles and the rate performances are shown in Figure 6.12b. We calculated the specific capacities based on the cathode, anode and the total mass of both cathode and anode. To compare our work with the reported symmetric full cell, we collected the data from the literatures and listed in **Table 6.1**. Our P2-NaNTO-based symmetric full cell delivers a high operating voltage at 2.8 V and an energy density around 65 Wh Kg^{-1}.

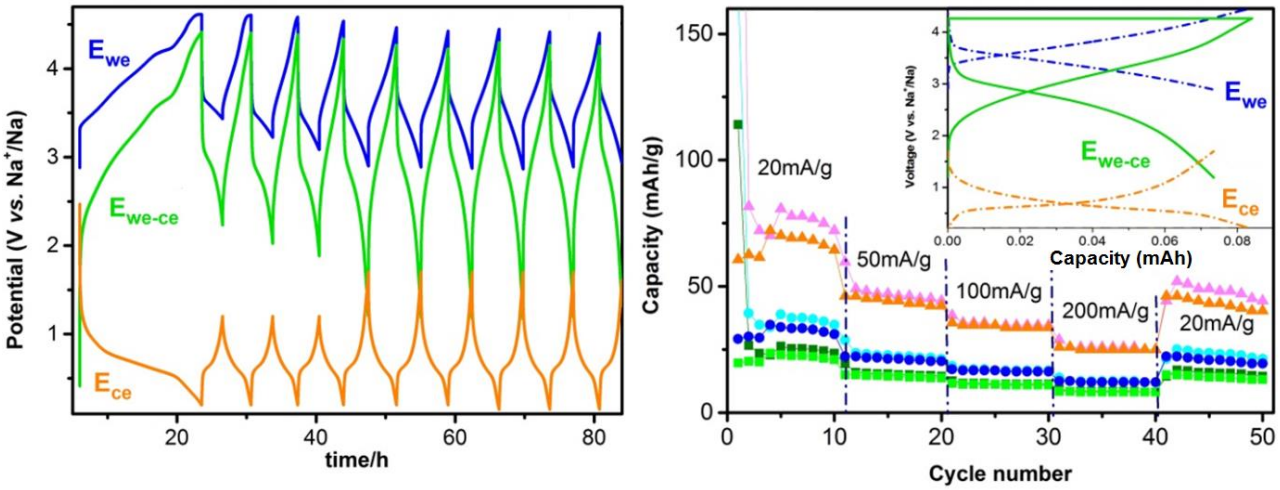

Figure 6.12. The electrochemical performances of symmetric Na-ion full cell based on P2-NaNTO sample tested in Swagelok cell. a). The charge/discharge curves of the cathode, anode and full cell; b). The specific capacities of the full cell calculated based on cathode, anode and the total mass of both cathode and anode. The mass ratio between cathode and anode is 2.07.

Table 6.1. Average operating voltages, capacities, energy density and power densities of reported symmetric full cell (calculated based on total mass of both cathode and anode)

Anode and Cathode	Voltage (V)	Capacity (mAh g^{-1})	Capacity 100th (avg)	Energy density (Wh kg^{-1})	Power density (W kg^{-1})
This work NaNTO-SS2	2.8	23 (20mA/g)	---	64.4	18.3
$Na_{0.6}[Cr_{0.6}Ti_{0.4}]O_2$ [23]	2.5	33-35(1C)	26-27	83-88	83-88
$Na_{0.8}Ni_{0.4}Ti_{0.6}°_2$ [16]	2.8	33(1C)	23	96(0.2C)	92
$Na_{2.55}V_6O_{16}·0.6H_2O$ [25]	1.5	16 (50mA/g)	13	24	8
$Na_{0.66}Ni_{0.17}Co_{0.17}Ti_{0.66}°_2$ [26]	3.1	35(100mA/g)	33	95	107
$NaNi_{0.33}Li_{0.11}Ti_{0.56}°_2$ [27]	3.1	34	20	100(0.2C)	20-26
$Na_3V_2(PO_4)_3$ [19]	1.7	25	19	43 (0.5C,58.8mA/g)	21-25
$Na_3V_2(PO_4)_3$ [28]	1.8	30	24	54(0.25C)	14
$Na_3Ti_2(PO_4)_3$ [29]	1.7	-	-	-	-
$Na_2VTi(PO_4)_3$ [30]	1.2	28(1C)	23(10000th cycle, 10C)	37	34
$Na_{0.5}Ni_{0.25}Mn_{0.75}O_2$ [24]	2.0	13 (at 107uA)	11.4(88%)	26	15

The structure study during intercalation/deintercalation through in-operando XRD

To understand the structure changes upon cycling in 0-2.0 V and 2.0-4.4 V ranges, we investigated the effect of Na^+ intercalation/deintercalation process on the overall structure of the P2-NaNTO sample as both anode and cathode. **Figure 6.13** reports a series of *in-operando* XRD patterns recorded on the anode electrode during the first electrochemical cycle (C-rate of C/20). The reflections related to the P2 phase were maintained during the whole charge/discharge process, with a progressive shift of the peaks during the sodiation process (orange curves of Figure 6.13a). The (002) and (004) peaks shifted to higher 2θ values while the (010) peak moved to lower angles, consistent with an contraction of the *c-axis* and a increase of the *a-axis*, shown in Figure 6.13c. Then (002) and (004) peaks of P2 shifted towards low angles and the (010) peak moved to high angles during the discharge process, corresponding to the reversible sodium insertion process in the 0-2.0 V range.

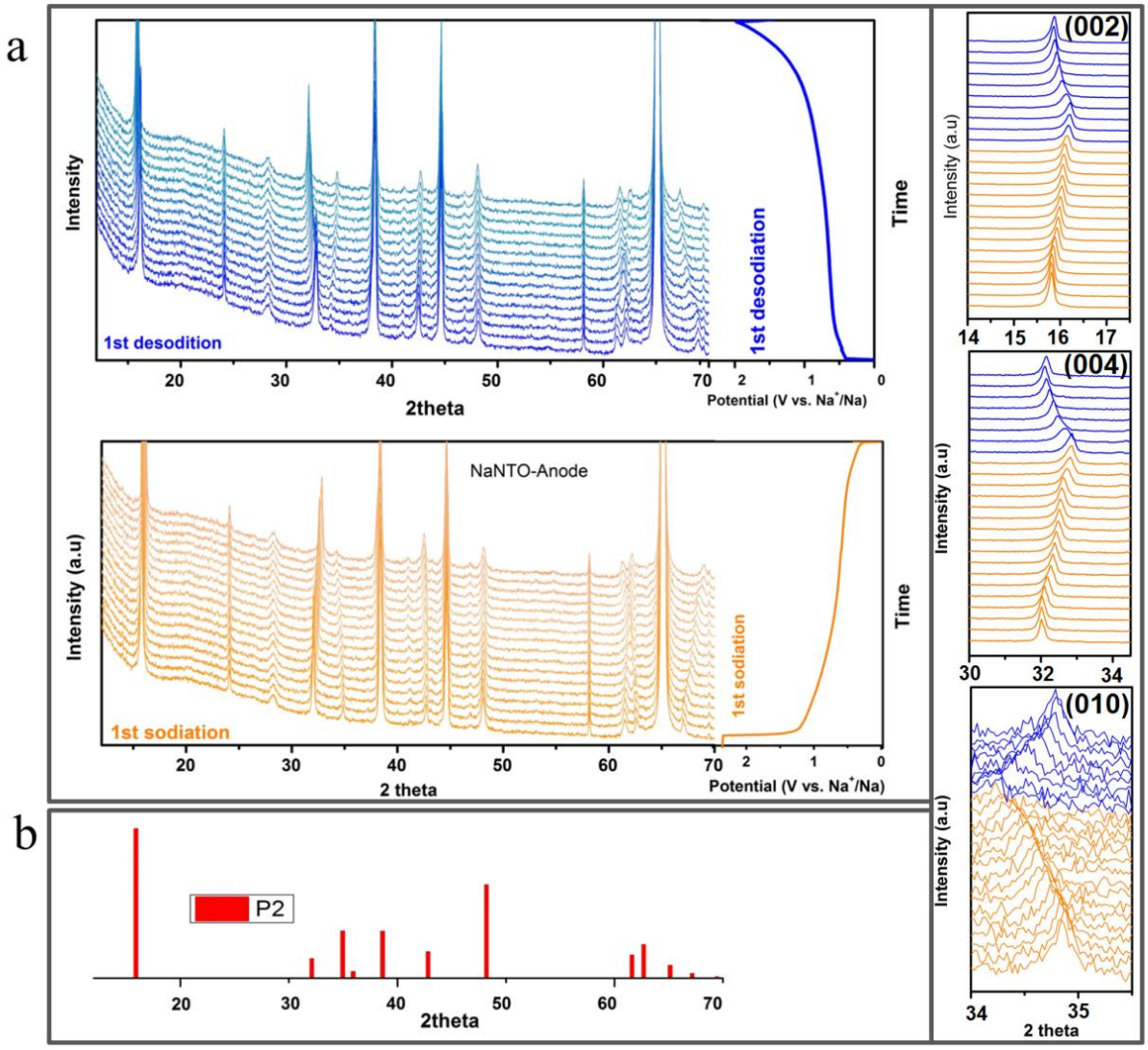

Figure 6.13. *In-operando* XRD characterization upon charge/discharge process of P2-NaNTO-based anode. (a) XRD patterns of the anode at different charge/discharge voltages in the 0-2.0 V range (blue curves are the desodiation process and the orange curves are the sodiation process); (b) XRD patterns corresponding to pure NaNTO with hexagonal layered structure (ICSD code: 90113). (c) the peaks shift indication of *in-operando* XRD patterns at different voltage during charge/discharge.

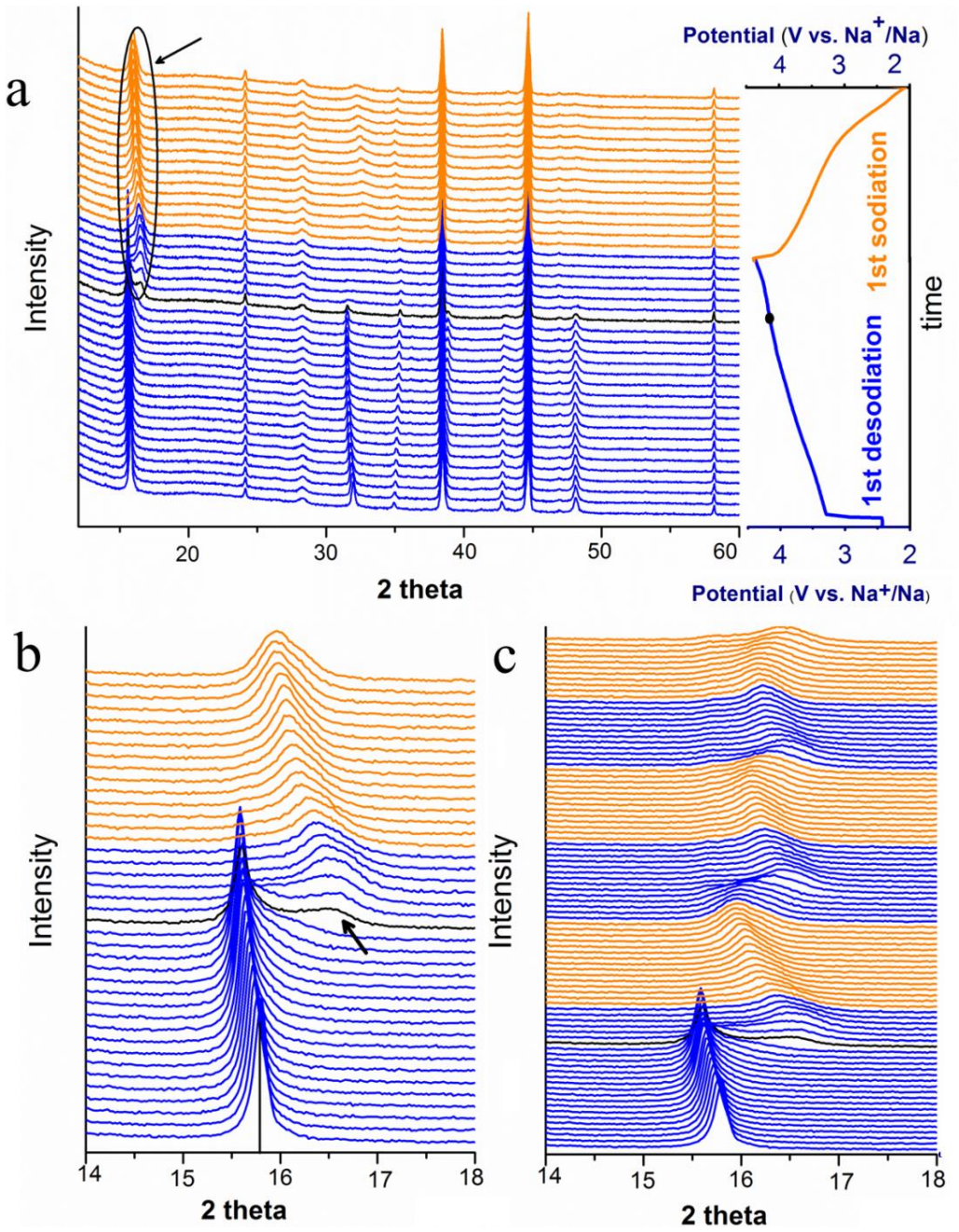

Figure 6.14. *In-operando* XRD characterization upon charge/discharge process of P2-NaNTO-based cathode. (a) XRD patterns of the cathode at different charge/discharge voltages in the 2.0-4.4 V range (blue curves are the desodiation process and the orange curves are the sodiation process); (b) the peak shift indication of *in-operando* XRD patterns at different voltages in the first cycle. (c) peak shift indication of *in-operando* XRD patterns at different voltages in the first 3 cycles.

Figure 6.14 reports the *in-operando* XRD patterns recorded on the cathode electrode during the first electrochemical cycle (C-rate of C/20). Different from the anode side, the reflections related to the P2 phase in the cathode were slowly fading when the cell charged from 2.0 V to 4,1 V, with a progressive shift of the peaks during the first desodiation process as shown in **Figure 6.14a**. A new peak at 16.5° appeared when the cell charged to 4.1 V, at which voltage the diffractions of the P2 phase were almost disappeared as shown in Figure 6.14a and Figure 6.14b. Moreover, the new peak remained in the rest of the desodiation process and the following desodiation process from 4.4 V to 2.0 V instead of the pristine P2 phase. Figure 6.14c presents the peak shift indication of the XRD patterns at different voltages in the first 3cycles. The diffraction peaks related to pristine P2 phase disappeared completely after the first desodiation process, instead, the new peak remained in the following cycles, which shows the irreversible phase change in the first desodiation process.

6. 3. Conclusions and Future work

The recent articles of the symmetric full cells have been firstly summarized and discussed in this chapter. A symmetric full cell based on bi-polar P2-$Na_{0.67}Ni_{0.33}Ti_{0.67}O_2$ material is eventually assembled and optimized. Three-electrodes testing system helped to study the properties on simultaneously cathode and anode, monitoring the occurring reactions. To operate a precise balancing of cathode and anode materials, different mass ratios between cathode and anode were studied and the ratio 2.07 gave the best results in counter balancing irreversible contribute coming from SEI layer formation and un-specified and low-intensity parasitic mechanisms. The symmetric full cell based on P2-$Na_x(Ni^{2+})_{1/3(}Ti^{4+})_{2/3}O_2$ delivers a high operating voltage of 2.8 V and an energy density around 65 Wh Kg^{-1}. Moreover, we found, *via in-operando* carried out on the electrodes at different voltages ranges (0-2.0 V and 2.0-4.4 V), that instable cycling performances of the full cell are primary due to the irreversible phase transition in the cathode during the first desodiation

process. The comprehensive investigation of the phase transition is still necessary in the following study.

6. 4. References

1. Nitta, N.; Wu, F.; Lee, J. T.; Yushin, G., Li-ion battery materials: present and future. *Materials today* **2015,** 18, (5), 252-264.

2. Slater, M. D.; Kim, D.; Lee, E.; Johnson, C. S., Sodium-ion batteries. *Advanced Functional Materials* **2013,** 23, (8), 947-958.

3. Ortiz-Vitoriano, N.; Drewett, N. E.; Gonzalo, E.; Rojo, T., High performance manganese-based layered oxide cathodes: overcoming the challenges of sodium ion batteries. *Energy & Environmental Science* **2017,** 10, (5), 1051-1074.

4. Xiang, X.; Zhang, K.; Chen, J., Recent Advances and Prospects of Cathode Materials for Sodium-Ion Batteries. *Advanced materials* **2015,** 27, (36), 5343-5364.

5. Kim, H.; Kim, H.; Ding, Z.; Lee, M. H.; Lim, K.; Yoon, G.; Kang, K., Recent Progress in Electrode Materials for Sodium-Ion Batteries. *Advanced Energy Materials* **2016**.

6. Dahbi, M.; Yabuuchi, N.; Kubota, K.; Tokiwa, K.; Komaba, S., Negative electrodes for Na-ion batteries. *Physical Chemistry Chemical Physics* **2014,** 16, (29), 15007-15028.

7. Serras, P.; Palomares, V.; Goñi, A.; de Muro, I. G.; Kubiak, P.; Lezama, L.; Rojo, T., High voltage cathode materials for Na-ion batteries of general formula $Na_3V_2O_{2x}(PO_4)_2F_{3-2x}$. *Journal of Materials Chemistry* **2012,** 22, (41), 22301-22308.

8. Palomares, V.; Serras, P.; Villaluenga, I.; Hueso, K. B.; Carretero-González, J.; Rojo, T., Na-ion batteries, recent advances and present challenges to become low cost energy storage systems. *Energy & Environmental Science* **2012,** 5, (3), 5884-5901.

9. Hasa, I.; Buchholz, D.; Passerini, S.; Scrosati, B.; Hassoun, J., High Performance $Na_{0.5}[Ni_{0.23}Fe_{0.13}Mn_{0.63}]O_2$ Cathode for Sodium-Ion Batteries. *Advanced Energy Materials* **2014,** 4, (15).

10. Han, M. H.; Gonzalo, E.; Singh, G.; Rojo, T., A comprehensive review of sodium layered oxides: powerful cathodes for Na-ion batteries. *Energy & Environmental Science* **2015,** 8, (1), 81-102.

11. Park, Y. U.; Seo, D. H.; Kim, H.; Kim, J.; Lee, S.; Kim, B.; Kang, K., A Family of High-Performance Cathode Materials for Na-ion Batteries, $Na_3(VO_{1-x}PO_4)_2F_{1+2x}$ $(0 \leq x \leq 1)$: Combined First-Principles and Experimental Study. *Advanced Functional Materials* **2014,** 24, (29), 4603-4614.

12. Etacheri, V.; Marom, R.; Elazari, R.; Salitra, G.; Aurbach, D., Challenges in the development of advanced Li-ion batteries: a review. *Energy & Environmental Science* **2011,** 4, (9), 3243-3262.

13. Goodenough, J. B.; Park, K.-S., The Li-ion rechargeable battery: a perspective. *Journal of the American Chemical Society* **2013,** 135, (4), 1167-1176.

14. Noguchi, Y.; Kobayashi, E.; Plashnitsa, L. S.; Okada, S.; Yamaki, J.-i., Fabrication and performances of all solid-state symmetric sodium battery based on NASICON-related compounds. *Electrochimica Acta* **2013,** 101, 59-65.

15. Kobayashi, E.; Plashnitsa, L. S.; Doi, T.; Okada, S.; Yamaki, J.-i., Electrochemical properties of Li symmetric solid-state cell with NASICON-type solid electrolyte and electrodes. *Electrochemistry Communications* **2010,** 12, (7), 894-896.

16. Guo, S.; Yu, H.; Liu, P.; Ren, Y.; Zhang, T.; Chen, M.; Ishida, M.; Zhou, H., High-performance symmetric sodium-ion batteries using a new, bipolar O3-type material, $Na_{0.8}Ni_{0.4}Ti_{0.6}O_2$. *Energy & Environmental Science* **2015,** 8, (4), 1237-1244.

17. Senguttuvan, P.; Rousse, G.; Arroyo Y De Dompablo, M.; Vezin, H.; Tarascon, J.-M.; Palacin, M., Low-potential sodium insertion in a NASICON-type structure through the Ti (III)/Ti (II) redox couple. *Journal of the American Chemical Society* **2013,** 135, (10), 3897-3903.

18. Plashnitsa, L. S.; Kobayashi, E.; Noguchi, Y.; Okada, S.; Yamaki, J.-i., Performance of NASICON symmetric cell with ionic liquid electrolyte. *Journal of the Electrochemical Society* **2010,** 157, (4), A536-A543.

19. Li, S.; Dong, Y.; Xu, L.; Xu, X.; He, L.; Mai, L., Effect of carbon matrix dimensions on the electrochemical properties of $Na_3V_2(PO_4)_3$ nanograins for high-performance symmetric sodium-ion batteries. *Advanced Materials* **2014,** 26, (21), 3545-3553.

20. Chevrier, V.; Ceder, G., Challenges for Na-ion negative electrodes. *Journal of The Electrochemical Society* **2011,** 158, (9), A1011-A1014.

21. Ren, W.; Zhu, Z.; An, Q.; Mai, L., Emerging Prototype Sodium-Ion Full Cells with Nanostructured Electrode Materials. *small* **2017**.

22. Shannon, R. D., Revised effective ionic radii and systematic studies of interatomic distances in halides and chalcogenides. *Acta crystallographica section A: crystal physics, diffraction, theoretical and general crystallography* **1976,** 32, (5), 751-767.

23. Wang, Y.; Xiao, R.; Hu, Y.-S.; Avdeev, M.; Chen, L., P2-$Na_{0.6}[Cr_{0.6}Ti_{0.4}]O_2$ cation-disordered electrode for high-rate symmetric rechargeable sodium-ion batteries. *Nature communications* **2015,** 6.

24. Palanisamy, M.; Kim, H. W.; Heo, S.; Lee, E.; Kim, Y., Insights into the Dual-Electrode Characteristics of Layered $Na_{0.5}Ni_{0.25}Mn_{0.75}O_2$ Materials for Sodium-Ion Batteries. *ACS Applied Materials & Interfaces* **2017,** 9, (12), 10618-10625.

25. Hartung, S.; Bucher, N.; Nair, V. S.; Ling, C. Y.; Wang, Y.; Hoster, H. E.; Srinivasan, M., Sodium Vanadium Oxide: A New Material for High-Performance Symmetric Sodium-Ion Batteries. *ChemPhysChem* **2014,** 15, (10), 2121-2128.

26. Guo, S.; Liu, P.; Sun, Y.; Zhu, K.; Yi, J.; Chen, M.; Ishida, M.; Zhou, H., A High-Voltage and Ultralong-Life Sodium Full Cell for Stationary Energy Storage. *Angewandte Chemie International Edition* **2015,** 54, (40), 11701-11705.

27. Zhang, S.; Liu, Y.; Zhang, N.; Zhao, K.; Yang, J.; He, S., O3-type $NaNi_{0\cdot33}\ Li_{0\cdot11}\ Ti_{0\cdot56}\ O_2$-based electrode for symmetric sodium ion cell. *Journal of Power Sources* **2016,** 329, 1-7.

28. Zhang, Y.; Zhao, H.; Du, Y., Symmetric full cells assembled by using self-supporting $Na_3V_2(PO_4)_3$ bipolar electrodes for superior sodium energy storage. *Journal of Materials Chemistry A* **2016,** 4, (19), 7155-7159.

29. Senguttuvan, P.; Rousse, G.; Arroyo Y De Dompablo, M.; Vezin, H.; Tarascon, J.-M.; Palacín, M., Low-potential sodium insertion in a NASICON-type structure through the Ti (III)/Ti (II) redox couple. *Journal of the American Chemical Society* **2013,** 135, (10), 3897-3903.

30. Wang, D.; Bie, X.; Fu, Q.; Dixon, D.; Bramnik, N.; Hu, Y.-S.; Fauth, F.; Wei, Y.; Ehrenberg, H.; Chen, G., Sodium vanadium titanium phosphate electrode for symmetric sodium-ion batteries with high power and long lifespan. *Nature Communications* **2017,** 8, ncomms15888.

CHAPTER VII

Conclusions

The entire project is focused on the synthetic methods preparation of nanocrystals and the investigation of their electrochemical properties in order to improve the energy of the rechargeable batteries. According to the different applications, this PhD work can be categorized into two parts. In the first part the investigation of inorganic nanocrystals as high-voltage cathode for Li-ion batteries, have been conducted, while in the second section, the increasingly important technological alternative to Lithium-ion battery, namely Sodium-ion, has been the object of the research.

A promising way to reduce the diffusion pathway of Li-ion and consequently improve the charge/discharge electrochemical performances of $LiMnPO_4$, is the use of nanoscale materials. The investigation of effective conductive carbon coating of LMP nanocrystals by etching the surface of the particles synthesized via colloidal, hydrothermal and solvothemal methods. A surface treatment with lithium hexafluorophosphate ($LiPF_6$) was studied as the way to remove the surfactant ligand shell of the LMP colloidal particles. The structure and morphology were preserved after carbon coating. The initial charge-discharge Coulombic efficiencies as well as capacity retention at high current rates were improved.

Material nano-structurization have been then extended to Sodium-ion cathode layered oxide P2-type $Na_{1.7}Ni_{1.0}Mn_{2.9}O_{7.6}$. A two-steps synthesis comprising a first colloidal step followed by a second sodiation step carried out *via* a solid-state reaction, was applied. By setting the atomic ratio to the value of Na:Ni:Mn ratios of 1.7:1:3 we were able to produce a cathode material that could withstand long charge/discharge cycles at working voltages up to 4.4 V vs. Na^+/Na. The main still unexplored behaviour of these materials is the poor structure stability upon the Na^+ intercalation/deintercalation at high operating voltage as cathode material. When they are deeply charged, low amount of the Na in the structure induced the gliding of the TMO-layers, with the transition to O2-phase. The material couldn't cycle above 4.2 V (vs. Na^+/Na) since P2-O2 phase transition is mostly irreversible. To operate safely, the operating voltage window is often reduced, limiting the deliverable energy. The colloidal+solid-state reaction was applied to obtain the P2-

phase NaNMO sample. *in-operando* XRD measurements showed P2-O2 phase transition is partially suppressed. This unique feature has been attributed to the peculiar crystalline patterning revealed by EDT, which is supposed to buffer and sensibly reduce stacking faults formation during repetitive cycling.

Inspired by this first promising achievements, the attention has been focused on anonther P2-phase materials, NaNTO. Thanks to Ni- and Ti-base active redox couples, this layered oxide material effectively acts as both cathode as well as anode for NIBs, in particular Ni^{2+}/Ni^{4+} and Ti^{4+}/Ti^{3+} Red-Ox couples can be activated at 3.5 V and 0.7 V vs Na^{+}/Na, respectively. We studied the electrochemical performances of this materials as both cathode and anode material for Na-ion batteries and figured out the solid-state reaction is the most reliable preparation route in terms of the phase purity and electrochemical characteristics. Moreover, P2-$Na_x(Ni^{2+})_{1/3(}Ti^{4+})_{2/3}O_2$ is the most promising bi-polar electrode material compared to other O3-phase compounds. By selecting and comparing the different electrolyte solutions, 1M $NaClO_4$ in PC/EC (1:1 V/V) as electrolyte was confirmed to be the best electrolyte to be used, ensuring a stable and reliable potential window ranging from 1.5-4.4 V for cathode and 0.01-2.5 V for anode. The optimized parameters in this work are the foundation for the symmetric Na-ion full cell. Based on the study, a symmetric full cell with P2-$Na_x(Ni^{2+})_{1/3(}Ti^{4+})_{2/3}O_2$ as both cathode and anode was assembled. Three-electrodes testing system helped to study the properties on simultaneously cathode and anode, monitoring the occurring reactions. To operate a precise balancing of cathode and anode materials, different mass ratios between cathode and anode were studied and the ratio 2.07 gave the best results in counter balancing irreversible contribute coming from SEI layer formation and un-specified and low-intensity parasitic mechanisms. The symmetric full cell based on P2-$Na_x(Ni^{2+})_{1/3(}Ti^{4+})_{2/3}O_2$ delivers a high operating voltage of 2.8 V and an energy density around 65 Wh Kg^{-1}. The instable cycling performances of the full cell might be caused by the irreversible phase transition in the cathode during the first desodiation process from the *In-operando* XRD measurements that carried out on the electrodes at different voltages ranges (0-2.0 V and 2.0-4.4 V). However, the mass balance ratio, the mechanism and the structure change in the full cell system based on the P2-type oxide still requires further investigation.